Kinetic studies of some solid-state reactions of metal sulfides

by

Haipeng Wang

A dissertation submitted for the degree of Doctor of Philosophy at the

University of Adelaide

Adelaide

Australia

August 2005

From the Author

I think I had a brilliant idea for the “Preface” but I forget what it was. Thoughts flashed through my mind and just vanished. Perhaps I am overwhelmed at the thought of finishing my thesis or by the thought that my "student-hood" is becoming history and my life is about to enter a new phase. As I am leaving the University of Adelaide after 2 years and 6 months study as a PhD student, my mind is filled with fond memories of the people that work with and the experiences that gave me the courage to seek an academic career. My heart holds all these experiences as treasures.
I count myself lucky to have been a member of the University Adelaide. The University has given me a unique opportunity to explore the "unknown world" and my journey of exploration continues.

Haipeng Wang

Adelaide

August 2005

THESIS BY PUBLICATIONS

This doctoral thesis is submitted as a portfolio of peer-reviewed publications according to the '*PhD Rules & Specifications for Thesis'* of the University of Adelaide. The journals in which these papers were published or accepted are closely related to the research field of this work. The citation information is listed and the journals are ranked in the order of impact factor in reference to their scientific significance (*Journal Citation Report* 2004, Thomson ISI).

Journal Title	Impact factor	Total Cites	Immediacy Index*	Cited Half-life**
Geochim. Cosmochim. Acta	3.811	26862	0.68	> 10.0
Am. Mineral.	1.785	8845	0.438	>10.0
Thermochim. Acta	1.161	6048	0.234	8.1

*Immediacy Index measures the average number of times that an article, published in a specific year within a specific journal, is cited over the course of the same year; **Cited Half-life measures the number of years, going back from the current year, that account for half the total citations received by the cited journal in the current year.

The thesis is based on the following papers.

1. Wang H., Pring A., Ngothai Y., O'Neill B. (2005) A low-temperature kinetic study of the exsolution of pentlandite from the monosulfide solid solution using a Refined Avrami method, *Geochim. Cosmochim. Acta*, **69**, 415-425.

2. Wang H., Pring A., Xie, Y., Ngothai Y., O'Neill B. (2005) Phase evolution and kinetics of the oxidation of monosulfide solid solution under isothermal conditions, *Thermochim. Act*, **427**, 13-25.

3. Wang H., Pring A., Ngothai Y., O'Neill B. (2005) The kinetics of the $\alpha \rightarrow \beta$ transition in synthetic nickel monosulfide, *Am. Mineral.*, (accepted).

4. Wang H., Pring A., Ngothai Y., O'Neill B. (2005) The mechanism and kinetics of α-NiS oxidation in the temperature range 670 – 700^{o}C, *Am. Mineral.*, (in press).

The following additional publications of relevance in the present work included in the appendixes of this thesis are:

A. Tenailleau C., Etschmann B., Wang H., Pring A., Grguric B.A., Studer A., (2005) Thermal expansion of troilite and pyrrhotite determined by *in situ* cooling (873 to 373 K) neutron powder diffraction measurements, *Mineral. Mag.*, **69**, 205-216.

B. Wang H., Ngothai Y., O'Neill B., Etschmann B., Pring A. (2003) The effects of S fugacity on the exsolution of pentlandite $(Ni,Fe)_9S_8$ from the monosulfide solid solution (Fe,Ni)S, CHEMECA 2003, the 31st Annual Australian Chemical Engineering Conference, Adelaide, Australia.

C. Wang H., Pring A., Ngothai Y., O'Neill B. (2005) X-ray study of the transition kinetics of α- to β-nickel monosulfide, CHEMECA 2005, the 33st Annual Australian Chemical Engineering Conference, Brisbane, Australia.

D. Ngothai Y., Wang H., Pring A., O'Neill B. (2005) A review on the controversial phase relations of pyrrhotite group minerals in low temperature ranges, CHEMECA 2005, the 33st Annual Australian Chemical Engineering Conference, Brisbane, Australia.

E. Wang H., Pring A., Xie, Y., Ngothai Y., O'Neill B. (2005) Phase evolution during the oxidation of monosulfide solid solution under isothermal conditions, CHEMECA 2005, the 33st Annual Australian Chemical Engineering Conference, Brisbane, Australia.

F. Wang H., Pring A., Ngothai Y., O'Neill B. (2005) Model-free kinetics of the pentlandite exsolution from monosulfide solid solution, the 7th World Congress of Chemical Engineering, Glasgow, U.K.

G. Wang H., Pring A., Ngothai Y., O'Neill B. (2005) A mineralogical kinetic note: Negative activation energy or misinterpretation of Avarmi method, the 7th World Congress of Chemical Engineering, Glasgow, U.K.

PANEL OF SUPERVISORS

Principle Supervisor

Dr. Yung Ngothai

Ph.D (RMIT University)

School of Chemical Engineering

The University of Adelaide

Email: yngothai@chemeng.adelaide.edu.au

Phone: + 61 8 8303 5445

Fax: + 61 8 8303 4373

Cooperative Supervisors

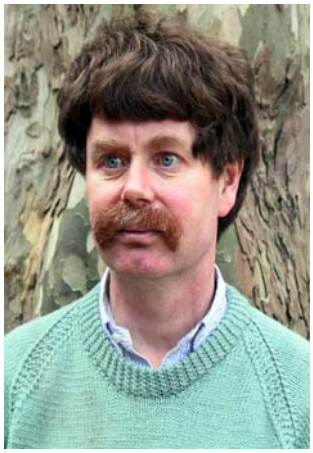

Prof. Allan Pring

Ph.D (University of Cambridge)

Department of Mineralogy, South Australian Museum &

School of Earth and Environmental Sciences

The University of Adelaide

Email: Pring.Allan@saugov.sa.gov.au

Phone: + 61 8 8207 7449

Fax: + 61 8 8207 7222

A/Prof. Brian O'Neill

Ph.D (University of Queensland)

School of Chemical Engineering

The University of Adelaide

Email: boneill@chemeng.adelaide.edu.au

Phone: + 61 8 8303 4647

Fax: + 61 8 8303 4373

Declaration

I declare that this work contains no material which has been accepted for the award of any other degree or diploma in any university or other tertiary institution, and to the best of my knowledge and belief, contains no material previously published or written by another person, except where due reference has been made in the text. The publications included in this thesis have not been previously submitted for the award of any degree at University of Adelaide or other university.

I give consent for this copy of my thesis, when deposited in the library of the University of Adelaide, being available for loan and photocopying.

Haipeng Wang

September 2005

Acknowledgement

I had so much enjoyment in working with my colleagues and supervisors that I almost feel sorry when realize the completion of this project is imminent. During these unforgettable years, many people have enlightened and encouraged me through their wisdom and support, without their input the success of this project would have been impossible. I am indebted to numerous people who have helped me; I apologize if not all of them are specially mentioned.

Thanks to my supervisors, Prof. Allan Pring, Dr. Yung Ngothai, and A/Prof. Brian O'Neill for your faith in me, and your unreserved help. Your enthusiasm in science has encouraged me to pursue my career in research.

I would like to thank Dr. Barbara Etschmann, Dr. Christophe Tenailleau for their assistance in collecting data and giving enlightening advices. Grateful appreciation is due to Dr. Joël Brugger for introducing me to the computational and simulation programs, MatLab, CrystalMaker. To all those who have helped with experimental and/or computational problems, thank you! I like to thank the Australian Education, Science and Training Department for the APA award, which has allowed this work to be carried out.

Finally, thanks to my parents……

爸爸妈妈:

谢谢您们的养育之恩，对我的关怀和教育。回首整整二十二年的求学生涯虽然有艰辛，有困惑，但是更多的是精神上的充实和获得成功时的喜悦。我将博士毕业，却思绪万千，突然想到应借我博士论文即将出版的机会，把我对您们的感谢写入这本书的“前言”。谨将此书献给您们，它标志我学生生涯的结束，也“纪录”了您们多年来对我付出的心血。没有您们的信任和鼓励，也不会有现在的我。

王海鹏

二零零五年九月于澳大利亚阿德莱德大学

Abstract

For many geochemical systems, reaction kinetics determines the system's current status and evolution. It might also be the key to unraveling their thermal history. In metal sulfide systems, kinetic studies have been carried out on four sets of solid-state transitions/transformations in Fe-Ni-S and Ni-S systems. In this work, a new kinetic model, the *Refined Avrami* method, has been developed to account for reactions involving changes in reaction mechanisms. Nonstoichiometric compounds are commonly present in these reactions.

The exsolution of pentlandite from the monosulfide solid solution (*mss*) is an important reaction in the formation of nickel ores. For near equimolar *mss* compositions, the reaction rate is rapid even in the low temperature ranges. For bulk composition $Fe_{0.77}Ni_{0.19}S$, the experimental results show the reaction rates (*mss* → pentlandite) vary from 1.6×10^{-5} to 5.0×10^{-7} s^{-1} at 200 ^{o}C and from 9.4×10^{-5} to 4.1×10^{-7} s^{-1} at 300 ^{o}C. The activation energy, E_a, varies during the course of reaction from 49.6 $kJ.mol^{-1}$ at the beginning of reaction (nucleation mechanism is dominant) to 20.7 $kJ.mol^{-1}$ at the end (crystal growth mechanism is dominant).

Monosulfide solid solution (*mss*) is a common intermediate phase observed during the oxidation of nickel ores, such as violarite and pentlandite. The investigation of *mss* oxidation is of benefit in understanding the thermal behavior of economically important metal sulfides during smelting. The oxidation products of *mss* vary in our samples depending on their compositions. Apart from the common oxidation products hematite and $Ni_{17}S_{18}$, $Fe_2(SO_4)_3$ was observed during the oxidation of $Fe_{7.9}S_8$, and pentlandite for $Fe_{6.15}Ni_{1.54}S_8$. The activation energy was determined using a model-free method. The

oxidation of $Fe_{6.4}Ni_{1.6}S_8$ exhibited a higher E_a than $Fe_{6.15}Ni_{1.54}S_8$ over the course of the reaction. The E_a increases with reaction extent (y) from 67.1 to 103.3 kJ.mol^{-1} for *mss* composition $Fe_{6.15}Ni_{1.54}S_8$ and from 76.1 to 195.0 kJ.mol^{-1} for $Fe_{6.4}Ni_{1.6}S_8$.

The kinetic study of the α-$Ni_{1-x}S \rightarrow \beta$-NiS transition shows that initial compositions of α-$Ni_{1-x}S$ plays an important role in the kinetics of the transition. The activation energy (E_a) for this α- to β-phase transition is 16.0 ($\pm$ 0.5) kJ.mol^{-1} for NiS in the temperature range 70 to 150 ^{o}C, and 13.0 ($\pm$ 0.5) kJ.mol^{-1} in the temperature range 250 to 350 ^{o}C. For $Ni_{0.97}S$, however, E_a deceases from 73.0 ($\pm$ 0.5) to 17.0 ($\pm$ 0.5) kJ.mol^{-1} over the course of the reaction in the temperature range 300 to 320 ^{o}C. The relationship between E_a and extent of transition (y) for the initial bulk $Ni_{0.97}S$ was derived using the *Refined Avrami* method. For Ni deficient compositions, α-$Ni_{1-x}S$, the transformation to β-NiS is accompanied by the exsolution of either a progressively more Ni deficient α-$Ni_{1-x}S$ and Ni_3S_4, and the reactions become more sluggish for more metal deficient compositions.

The study of oxidation kinetics of α-NiS is of metallurgical interest, as α-NiS related phases may occur when nickel ores are flash smelted to produce nickel matte. In an open-air environment, the oxidation mechanisms of α-NiS are constant at 670 and 680^{o}C, dominated by the direct oxidation of α-NiS → NiO. The dominant oxidation mechanism changes to a chain reaction: α-NiS $\xrightarrow{k_1}$ Ni_3S_2 $\xrightarrow{k_2}$ NiO at 700^{o}C. Therefore, different kinetic models need to be applied to these two distinct reaction mechanisms. Activation energy for the oxidation, α-NiS → NiO, in the temperature range 670 to 680^{o}C was calculated to be 868.2 kJ.mol^{-1} using *Avrami/Arrhenius* method. Rate constant k_1 and k_2 are approximated to be 3×10^{-4} s^{-1} and 5×10^{-4} s^{-1} for the first part and second part of the chain reaction respectively at 700^{o}C.

The study of the variation in reaction rate with oxidation time illustrates the optimum oxidation time zone for each temperature, where NiO can be produced at the fastest rate.

CONTENTS

CHAPTER ONE

Chapter 1: Introduction

1.1 Overview

Kinetics has been the subject of a vast number of studies in geochemistry, metallurgy and mineralogy, and it will certainly continue to draw our attention, as in many geochemical systems it is the controlling factor in deciding the fate and evolution of a reaction or transition. The development of kinetic theories is based on the laws of thermodynamics, which identify a point toward which a reaction is proceeding (Burker, 1965; Lasaga, 1997). A thermodynamically predicted reaction does not always happen depending on what extent the reaction is kinetically driven (Broecker and Oversby, 1971). Although significant progress has been made in understanding the thermodynamic properties of equilibrium systems, the nonequilibrium application of kinetics to geology, metallurgy and mineralogy is still at its embryonic stage (Lasaga, 1997). The study of kinetics is inherently more difficult than that of thermodynamics because its time-dependent processes are also path dependent. A variety of kinetic theories have been developed to apply to different reaction systems. For solid-state reactions, the following kinetic models and theories are of interest for chemists: rate laws of chemical reactions, transition state theory, diffusion, nucleation theory, and the theory of crystal growth.

1.2 Rate Laws

Rate laws consist of a series of formula/functions that describe the influence of external parameters (e.g. concentration, temperature) on the reaction rate. The first step in understanding the rate laws is to decompose a complex reaction into a number of elementary reactions. Most solid-state reactions are not a single step process. They

contain a series of elementary reactions (reaction steps), the basic components for a solid-state reaction because they are based on the simplest molecular collisions (Wilkins, 1991; Rosén et al., 2005; Hu, 2004). However, the overall reaction represents the net result of these elementary reactions. The description of an overall reaction in terms of each elementary reaction involved is termed the "reaction mechanism". A general overall reaction can be written as:

$$aA + bB \rightarrow cC + dD \tag{1.1}$$

The reaction rate is defined as:

$$\text{Rate} \equiv -\frac{1}{a}\cdot\frac{dC_A}{dt} = -\frac{1}{b}\cdot\frac{dC_B}{dt} = \frac{1}{c}\cdot\frac{dC_C}{dt} = \frac{1}{d}\cdot\frac{dC_D}{dt} \tag{1.2}$$

Generally, it is a function of the concentrations of reactants and products.

$$\text{Rate} \equiv kC_A^{n_A}C_B^{n_B}C_C^{n_C}C_D^{n_D} \tag{1.3}$$

where C is concentration. n can be any real number and the sum, $n_a + n_b + n_c + n_d$ is termed the "order" of the overall reaction. k is referred to as the rate constant and has units of concentrations to the power $-(n_a + n_b + n_c + n_d - 1)$ per unit time (Frost and Pearson, 1961; Moore and Pearson, 1981; Lasaga, 1997).

Equation (1.3) indicates that the rate law of a complex reaction can depend on both reactants and products. An elementary reaction, on the other hand, only depends on the reactants and is always proportional to the concentration of each reactant (Hinshelwood, 1951; Hu, 2001; Lű, 2003). Since an elementary reaction occurs only via molecular collision, a simple rate law is expected.

The concept of "steady state" is often used to reveal details of reaction mechanism (Meek et al., 1994; Zhu, 2000, Wu, 2004). For example, if a simple reaction,

$$2R \text{ (reactant)} \rightarrow 3P \text{ (product)} \tag{1.4}$$

proceeds through intermediate reactions,

$$R \xleftrightarrow{k_{-1},k_1} P + M \quad \text{fast reversible reaction} \tag{1.5a}$$

$$M + R \xrightarrow{k_2} 2P \quad \text{slow} \tag{1.5b}$$

the concentration of the intermediate reactant, *M*, will reach a steady value after a transient period, where $d[M]/dt = 0$.

$$\frac{d[M]}{dt} = k_1[P] - k_{-1}[R][M] - k_2[M][R] = 0 \tag{1.6}$$

Using this steady-state constraint the reaction rate can be solved as:

$$\frac{d[P]}{dt} = k_1[R] - \frac{k_{-1}[P]k_1[R]}{k_{-1}[P] + k_1[R]} + \frac{2k_2k_1[R]^2}{k_{-1}[P] + k_1[R]} \tag{1.7}$$

Reaction (1.5a, b) is via typical sequential reaction. The slow second step (equation (1.5b)) determines the overall reaction rate; hence, this step is called rate-determining step. It is not always true that the slowest steps are rate determining. In parallel reactions, for instance, the fastest step is the rate-determining step.

In kinetic studies, temperature is one of the most important variables. The rate constant (*k*) is found to be exponentially dependent on temperature. *k* is commonly expressed in *Arrhenius* equation:

$$k = A\exp(-\frac{E_a}{RT}) \tag{1.8}$$

where A is the pre-exponential factor. E_a is the activation energy, and *R* is the gas constant (8.314 $J.K^{-1}.mol^{-1}$), T is the reaction temperature in Kelvin. The value of activation energy has been used to empirically estimate reaction mechanism (Christian, 1965; Etschmann et al., 2004; Sima-Ella et al., 2005; Leo et al., 2005). For instance,

diffusion-controlled reactions in fluid media normally have rather low activation energies (e.g. less than 20 kJ.mol^{-1}). For bulk diffusion in solid-state reactions, E_a is typically in the range of 80-400 kJ.mol^{-1}. Most of the activation energies for a wide variety of mineral-solution alteration processes lie in the range 40-80 kJ.mol^{-1} (Lasaga, 1997). Most solid-state reactions are, at least in part, heterogeneous. Interface areas between phases invariably affect these reactions. An important parameter in heterogeneous kinetics is the reactive surface area available for reaction. The surface area of a mineral (A) can be obtained from the vol% abundance, x, and the mean size of crystals, r_0 using the following equation:

$$A = \frac{3x}{100 r_0}\left[\frac{1 + 2\alpha^2 r_0^2}{3 + 2\alpha^2 r_0^2}\right] \tag{1.9}$$

The parameters α and r_0 follow a gaussian distribution of N (number of crystals/unit volume).

$$N(r) = N_0 \exp[-\alpha^2 (r - r_0)^2] \tag{1.10}$$

N_0 is a pre-exponential constant. The surface area (A) must be corrected to reactive surface area before it can be used in kinetic calculations because the reactive surface area may only be a fraction of the total area (Aagaard and Helgeson, 1982; Helgeson et al., 1984). Lasaga (1986) proposed a parameter, γ, which is an indicator for reactive surface area.

$$\gamma \equiv k_A A \tag{1.11}$$

where k_A is the surface reaction rate constant and A is the total surface area. For a solid-state reaction controlled by surface reactions, the mineral with the lowest value of γ determines the overall reaction rate. Typically only the surface area of one mineral

significantly affects the overall reaction rate. In the initial stage of a reaction, the very low abundance of a product may control the reaction rate because the value of γ is very small; the kinetics is therefore controlled by the nucleation rate of this product mineral. Another important effect of surfaces in a heterogeneous system is to alter the activation energy of a solid-state reaction. This process normally involves adsorption of gas species onto a surface. For example, suppose a heterogeneous reaction has the following mechanism:

$$R + G \leftrightarrow R \bullet G \quad \text{equilibrium constant } K \tag{1.12a}$$

$$R \bullet G \xrightarrow{k_1} P \bullet G \quad \text{slow} \tag{1.12b}$$

$$P \bullet G \xrightarrow{k_2} P + G \tag{1.12c}$$

R, P, G stand for reactant, product, and gas species respectively. $R \bullet G$ and $P \bullet G$ are adsorbed species. The overall production of *P*, therefore, can be solved as:

$$\frac{d[P]}{dt} = k_1[R \bullet G] = k_2[P \bullet G] = Kk_1[R][G] \tag{1.13}$$

The activation energy of the overall reaction is therefore easily derived from the temperature dependence of both *K* and k_1.

$$E_a = \Delta H_{ad} + E_1 \tag{1.14}$$

where ΔH_{ad} is the heat of adsorption of the gas species and E_1 is the activation energy of the slow surface reaction (1.12b). If ΔH_{ad} is negative (strong adsorption), the overall activation energy will be reduced (Lasaga, 1997).

1.3 Transition State Theory

Transition state theory provides a method to explain the temperature and concentration dependence of the rate law (Moore, 1972). A potential surface is employed to portray the

variation in energy of the system as a function of the positions of all atoms involved in an elementary reaction. The reactant and product lie in a region of the potential surface that can be described as deep "valleys" (or minima). Transition state theory (TST) provides the means to characterize the reaction through "reaction coordinates", reaction paths to pass the potential energy barrier between reactant and product. The position at the "mountain pass" of the potential surface is termed "activated complex" (Moore, 1972; Pechukas, 1981; Lasaga, 1997). It is an intermediate state between reactant and product. A typical example of a potential surface in transition state theory is shown in Figure 1.1. Reactant (R) and product (P) lie in the valleys, whereas the activated complex located at the "saddle point" (A) along the reaction path.

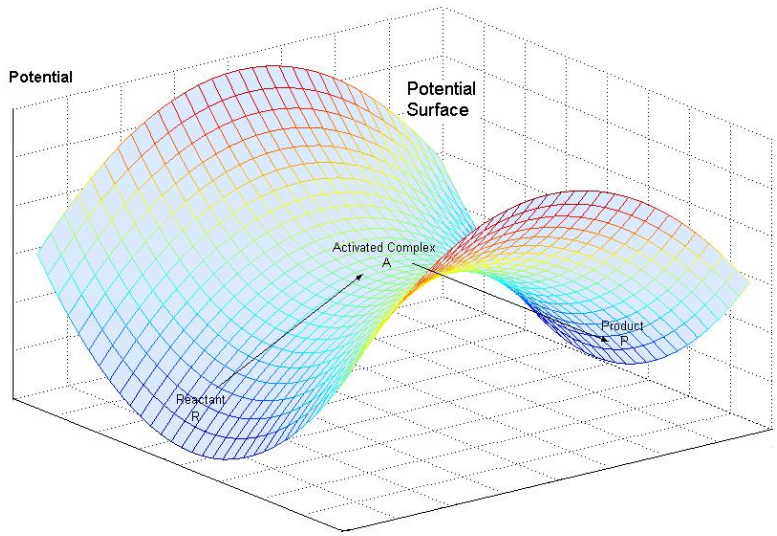

Figure 1.1. The topography of potential surface in the neighborhood of an activated complex. 'R' represents the intermolecular coordinates of reactant; 'P' for product; 'A' (saddle point) for the activated complex. The horizontal plane gives intermolecular coordinates for each species. The vertical axis represents chemical potential (e.g. changes in Gibbs energy with compositions).

For the elementary reaction

$$a + b \rightarrow ab \tag{1.15}$$

an activated complex is formed during the reaction at the transition state between forming products from reactants.

$$a + b \leftrightarrow a\ldots b \text{ (activated complex)} \rightarrow ab \tag{1.16}$$

The rate of reaction is equal to the product of the frequency, ν, of the activated complex crossing the barrier and the concentration of the transition state complex,

Rate = ν [a…b]. The transition state complex (a…b) and the reactants are in pseudo equilibrium at the top of the energy barrier, $K^{\#}$ =[a…b]/[a][b] (Geoffrey, 1966; Cohen, 1991; Lű, 2003). Therefore,

$$\text{Rate} = \nu K^{\#}[a][b] \tag{1.17}$$

According to the rate law, Rate = k [A][B] = Aexp(-E_a/RT)[a][b]. The assumption of equilibrium between the reactants and the activated complex gives,

$$k = \frac{k_B T}{h} K^{\#} \tag{1.18}$$

where k_B is the Boltzmann constant (1.3806503×10^{-23} $m^2.kg.s^{-2}.K^{-1}$) and h is the Planck constant (6.626068×10^{-34} $m^2.kg.s^{-1}$). The rate constant can also be expressed as:

$$k = \frac{k_B T}{h} \exp(\frac{\Delta S_0^{\#}}{R}) \cdot \exp(-\frac{\Delta H_0^{\#}}{RT}) \tag{1.19}$$

where $\Delta S_0^{\#}$, the entropy of activation, is the standard molar change of entropy when the activated complex is formed from reactants. $\Delta H_0^{\#}$, the enthalpy of activation, is the corresponding standard molar change of enthalpy. The quantities E_a (activation energy) and $\Delta G_0^{\#}$ (known as the *Gibbs activation energy*,) are not quite the same, the relationship between them is given by:

$$k = \frac{k_B T}{h} \exp(-\frac{\Delta G_0^{\#}}{RT}) = A \exp(-\frac{E_a}{RT}) \tag{1.20}$$

1.4 Diffusion

Diffusion is an important mechanism for mass transport in solid-state reactions. It relates a given flux of a component to a driving "force". For example, the flux (J_A) of a component *A* is defined as the quantity of *A* passing through a unit area during unit time. According to *Fick's First Law*, J_A is proportional to the concentration gradient of *A*.

$$J_A = -D_A \frac{\partial [A]}{\partial x} \tag{1.21}$$

where *x* is the distance measured normal to the surface that flux passes through. D_A is diffusion coefficient. The negative sign is to make D_A positive quantities (Kidson, 1961; Frank et al., 1962; Su et al., 2005).

The driving force for the flux appears to be the concentration gradient in equation (1.21), however, the chemical potential gradient is preferable for the expression of diffusion flux. For the situation when a flux diffuses across two different phases, there will be a discontinuity in concentration across the phase boundary (e.g. a discontinuity in $\partial [A]/\partial x$). This discontinuity is solved by substitution of $\partial \mu_A / \partial x$ (chemical potential gradient) for $\partial [A]/\partial x$, as for local equilibrium, $\mu_A^I = \mu_A^{II}$ at the boundary between phase I and II (Alberty, 1979). Therefore, the gradient in chemical potential is the true driving force for diffusion. The chemical potential can be expressed as:

$$\mu_A = \mu_A^0 + RT \ln(\gamma_A [A]) \tag{1.22}$$

where μ_A^0 is the chemical potential in a standard state, and γ_A is the activity coefficient. Incorporating equation (1.22) into the flux equation and using the mobility of a species, m_A, defined as the flux velocity attained per unit force ($J_A = -m_A [A] \cdot \partial \mu_A / \partial x$):

$$J_A = -RTm_A(1+\frac{\partial \ln \gamma_A}{\partial \ln[A]})\frac{\partial[A]}{\partial x} \tag{1.23}$$

Thus, the diffusion coefficient D_A is:

$$D_A = RTm_A(1+\frac{\partial \ln \gamma_A}{\partial \ln[A]}) \tag{1.24}$$

There are three types of diffusion that occur in solid-state reactions namely, surface diffusion, grain boundary diffusion, and bulk diffusion (Lasaga, 1997). An illustration of three diffusion mechanisms is shown in Figure 1.2. Surface diffusion occurs over a two-dimensional interface between the crystal grain and nonsolid (air or solution) media. It is very important in the study of crystal growth. Grain boundary diffusion occurs along the boundaries between two solid phases. Bulk diffusion occurs within the lattice sites of the solids.

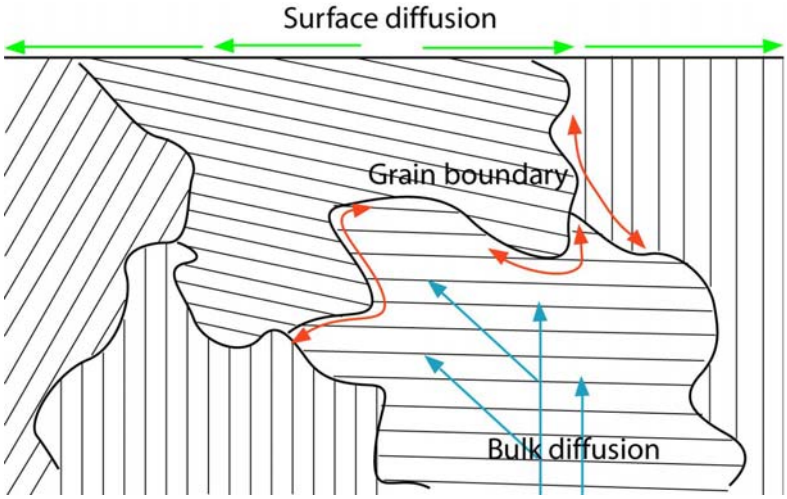

Figure 1.2. Three types of diffusion paths in solid-state reaction, surface diffusion (paths shown in green), grain boundary diffusion (paths shown in red), and bulk diffusion (paths shown in blue).

In general, surface diffusion is the fastest followed by grain boundary diffusion, whereas bulk diffusion is the slowest and is normally three to four orders of magnitude slower than the other diffusion mechanisms. In solid-state reactions, a key factor controlling the

values of diffusion coefficients is the structure of the material. Diffusion in ionic materials is typically faster than in strongly covalent materials, and diffusions in metallic materials are even faster than in ionic materials (Hu, 2001).

The diffusion coefficient in solids is strongly dependent on temperature, and follows the *Arrhenius* law:

$$D_A = D_0 \exp(-\frac{E_a}{RT}) \tag{1.25}$$

Hence, ln(D_A) is a linear function of 1/T if the reaction mechanism remains constant. A significant deviation from linearity of the plot of lnD_A ~ 1/T indicates a change in the diffusion mechanism. Given a known diffusion coefficient (D_A), *Fick's Second Law* is commonly used to solve the concentration function over time and distance. If we treat D_A as a constant, then for one-dimensional diffusion, *Fick's Second Law* becomes:

$$\frac{\partial[A]}{\partial t} = D_A \frac{\partial^2[A]}{\partial x^2} \tag{1.26}$$

Like any partial differential equation, the solution of *Fick's Second Law* for the concentration depends on both the initial and boundary conditions (Aoki et al., 1984; Van-Baal, 1985; Diao and Hess, 2004). Figure 1.3 represents the case where the diffusing species is initially concentrated at $x = 0$ ($t = 0$) and $[A]_{(x,t)}$ diffuses out when $t \to \infty$.

The solution for equation (1.26) is for the one dimensional, constant diffusivity case.

$$[A]_{(x,t)} = \frac{[A]_0}{2\sqrt{\pi D_A t}} \exp(-\frac{x^2}{4D_A t}) \tag{1.27}$$

where $[A]_0$ is the initial concentration of *A*.

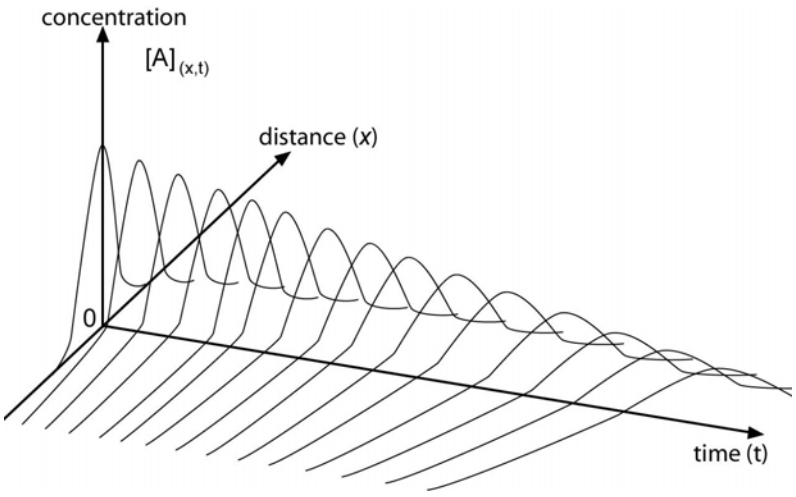

Figure 1.3. Illustration of the simple *Gaussian* solution to the diffusion equation (1.26) for diffusion from a point source. The concentration of species A, $[A]_{(x,t)}$, varies with time (t) and the diffusion distance (x).

1.5 Nucleation

Nucleation is an atomic process by which atoms of a reactant rearrange their positions to form a cluster of a product phase. The cluster has to be sufficiently large to be thermodynamically stable. The atomic fluctuations occurring during a nucleation process are very small, typically on the scale of 10-1000 atoms. This size scale renders difficulties for the observation of a nucleation process (Lasaga, 1997). Although nucleation is a crucial step in many geochemical and mineralogical processes, the development of nucleation theories is still at its infancy. The chemical and physical properties of nuclei surfaces significantly affect the energetics of nucleation process. The surface effect is more important for smaller nuclei. The surface effect can be assessed in terms of 'excess surface free energy', which is defined as:

$$\sigma = \left(\frac{\partial \Delta G}{\partial A} \right)_{V,P,T} \tag{1.28}$$

where σ is excess surface free energy; A is surface area (Adamson, 1990). The value of σ depends on the nature of the two phases (reactant and product). The magnitude of σ reflects the structural mismatch between the nucleus and the host phase. In fact, σ is a function of the cluster size, but it varies very little once the nucleus attains a critical volume, therefore σ is always assumed constant over the range of sizes of interest in nucleation.

The energy needed to form a cluster consists of two parts; one is the free energy change (product minus reactant), the other one is surface free energy term (Castellan, 1983).

$$\Delta G = n\Delta G_r + A \cdot \sigma \tag{1.29}$$

where ΔG is the total energy required for nucleation. ΔG_r is the free energy change from one reactant atom to one product atom. n is the number of atoms in the cluster. A is the surface area of cluster. Clearly, ΔG varies with cluster size, or equivalently, with the value of n. A typical $\Delta G \sim n$ curve for a supersaturated system is illustrated in Figure 1.4.

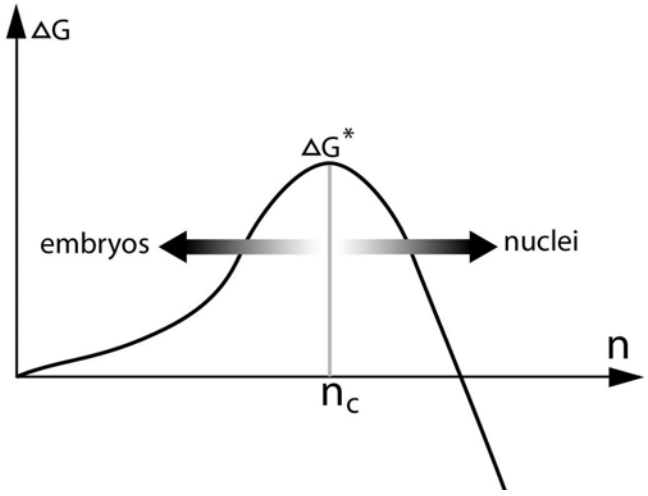

Figure 1.4. Schematic graph showing the free-energy change in the formation of a cluster with n atoms in a nucleation process (after Lasaga, 1997).

In equation (1.29), ΔG_r must have negative values because a nucleation process would not be possible if the product were not thermodynamically favorable. However, the total free energy change ΔG is not always negative. Figure 1.4 suggests that there is a maximum (ΔG^*) at $n = n_c$ (the critical number of n). The position of this maximum allows the definition of two types of clusters. Those with $n < n_c$ are termed 'embryos', whereas those with $n > n_c$ are termed 'nuclei'. Nuclei will continue to grow into a crystal, however embryos are unstable and will decompose to reactant atoms. The critical size of the cluster (n_c) fixes the free energy change in this region, ΔG^* (Moore, 1972). This is analogous to the 'transition state theory'. In a sense, the critical cluster has become the equivalent of an activated complex in the 'transition state theory', and ΔG^* is the energy barrier (activation energy) (Hu, 2001).

The nucleation rate is the net rate of the forward and reverse rates of the following reaction:

$$E_n + E \leftrightarrow E_{n+1} \tag{1.30}$$

It is a reversible reaction, attaching and detaching a single atom (E) to an 'n' cluster (E_n) to form an 'n+1' cluster (E_{n+1}). The energy change for a cluster from E_n to E_{n+1} is termed 'Δg^*'. The nucleation rate is a function of time. However, following a transient period, a steady-state nucleation rate will be attained. An approximation for the nucleation rate is formularized as:

$$I = N_0 \frac{k_B T}{h} \cdot \frac{A_c}{n_c} \left(\frac{\Delta G^*}{3\pi k_B T}\right)^{1/2} \exp\left(-\frac{\Delta g^* + \Delta G^*}{k_B T}\right) \tag{1.31}$$

where I is the nucleation rate. A_c is the surface area for critical cluster size $n = n_c$. k_B is the Boltzmann constant and h is the Planck constant. N_0 is the total number of atoms of

reactant in the medium. Δg^* can be approximated by the activation energy for diffusion or viscosity in a melt (Lasaga, 1997).

The nucleation rate normally increases dramatically at the beginning, given a suitable extent of 'overcooling' (current temperature minus equilibrium temperature). However, as the temperature drops further, the high activation energies associated with diffusion or viscosity in melts (Δg^*) will make the nucleation rate eventually decrease back to zero.

It is known that the surface energy is crucial to the nucleation rate; therefore any process that affects σ value will affect the nucleation rate. The most obvious impact factor is the presence of solid surfaces (more often originating from impurities) during the nucleation. The accumulation of product atoms onto an existing foreign solid surface is termed 'heterogeneous nucleation' (Smith, 1980; Hu, 2001). To simplify the calculation of change in free energy (ΔG_{het}) for a heterogeneous nucleation process, a spherical embryo is generally assumed (see Figure 1.5).

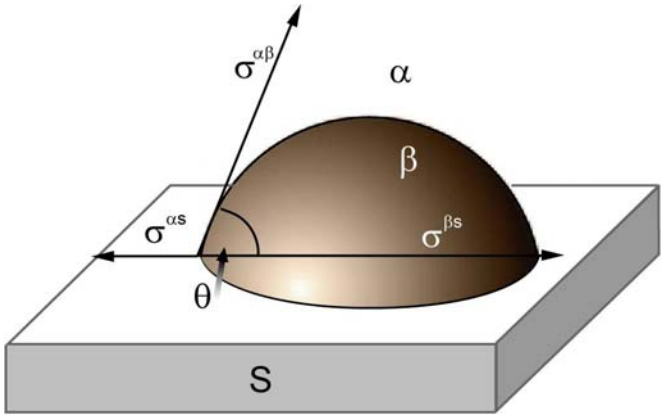

Figure 1.5. Schematic graph showing the formation of an embryo (β-phase) on a flat impurity plate (S-phase). The media is α-phase. σ^{ij} is the surface free energy between phases *i* and *j* (*i* or *j* = α, β, and S).

For the nucleation of the β-phase in the α-phase media with the presence of impurity solid surface (S-phase), the contact area between α and β-phase (or β and S phase) is given by the following equations.

$$A^{\alpha\beta} = 2\pi r^2(1-\cos\theta) \tag{1.32a}$$

$$A^{\beta s} = \pi r^2 \sin^2\theta \tag{1.32b}$$

where $A^{\alpha\beta}$ and $A^{\beta s}$ are the α-β and β-S contact areas. r is the 'radius' of the nucleus. θ is the contact angle, as shown in Figure 1.5. The change in free energy upon formation of the β nucleus in a heterogeneous process is given by (Lasaga, 1997):

$$\Delta G_{het} = \frac{V^{\beta} r^3}{v^{\beta}} \Delta G_r + [A^{\alpha\beta}\sigma^{\alpha\beta} + A^{\beta s}(\sigma^{\beta s} - \sigma^{\alpha s})]^3 (v^{\beta})^2 \tag{1.33}$$

where $V^{\beta} r^3$ is the total volume of the nucleus and $V^{\beta} = \pi(2-3\cos\theta+\cos^3\theta)/3$. σ^{ij} is the surface free energy between phases i and j (i or j = α, β, and S). v^{β} is the molecular volume of β-phase. θ, the contact angle, is determined from the balance of tensional forces at the α-β-S triple contact (Figure 1.5)

$$\sigma^{\alpha s} = \sigma^{\beta s} + \sigma^{\alpha\beta}\cos\theta \tag{1.34}$$

The free-energy change for formation of the critical nucleus can be obtained by setting $\partial \Delta G_{het} / \partial r = 0$, and then solving $\Delta G_{het} = \Delta G^*$, $r = r_c$. Obviously, whether the nucleus grows on the impurity plate depends on the variation of ΔG_{het} with r. If the derivative ($\partial \Delta G_{het} / \partial r$) is negative, then the nucleus will grow (Moore, 1972; Zhu, 2000; Wu, 2004).

1.6 Crystal Growth

The possible atomic processes during crystal growth are normally divided into two groups, surface processes and transport processes. Attachment, detachment, and movement of atoms on a crystal surface are surface processes. Transport and diffusion of atoms from the media to the crystal surface (or diffusion away from surfaces) are transport processes. If the rate of growth (or dissolution) were surface controlled, there would be very small concentration gradient in the reactants within the medium surrounding the growing phase because the transport mechanism acts fast enough to ensure homogeneity. Sometimes, the controlling growth mechanism can be reflected in the crystal's morphology (Frost, 1961; Xie, 2004). Surface-controlled reactions are more sensitive to the surface topography. Consequently, the growth or dissolution process is related to crystallographic directions. Transport-controlled reactions, on the other hand, normally form spherical product crystals (Lasaga, 1997).

As a rule of thumb, the activation energy for a transport-controlled process is much lower than that of a surface-controlled process. The general rate equation (1.8) indicates that temperature has greater impact on reactions possessing a higher value of E_a. Therefore, with an increase in temperature, the rates of surface chemical reactions (higher E_a) increase more rapidly than those for diffusion or transport. As a result, an initial surface controlled crystallization process may eventually switch to a transport controlled process as the temperature increases. As an example Berner (1978) has proposed that in aqueous solutions, minerals with low solubility dissolve by surface control, whereas high-solubility minerals dissolve by transport control.

For solid-state reactions, the *Avrami* equation is widely employed as a kinetic model of crystal growth. A general form of *Avrami* equation is:

$$y = 1 - \exp[-(k \cdot t)^n] \tag{1.35}$$

where y is the reaction extent. *k* is rate constant. *t* is reaction time. *n* is an exponent.

If this model is appropriate then the parameters *k* and *n* may be determined from a plot of lnln[1/(1-*y*)] against ln(*t*). The value of n depends on the reaction/growth mechanism. Large changes in *n* indicate changes in the reaction mechanism (Christian, 1965; Yund and McCallister, 1970; Putnis, 1992; Etschmann et al., 2005; Wang et al., 2005a, b, c, d). Early attempts by Christian (1965) to assign particular reaction or growth mechanism to particular values of *n* were later shown to be invalid (Yund and Hall, 1970;Etschmann et al., 2005; Wang et al., 2005a). The reaction rate indicated by the *Avrami* equation follows the general form:

$$\text{Rate} = \frac{dy}{dt} = k^n t^{n-1}(1 - y) \tag{1.36}$$

Although *Avrami* equation was designed to study the kinetics of crystal growth, it is more often used describe the overall reaction process. Because for solid-state reactions, it is very difficult to distinguish different stages of a reaction (e.g. nucleation, diffusion, and crystallization). The *Avrami* equation has been successful in predicting the kinetics of many solid-state reactions. However, its inherent defect, the assumption of constant activation energy (E_a), means the classic *Avrami* equation failed to explain many other kinetic behaviors of solid-state reactions, especially in nonstoichiometric systems. In this work, we developed a new kinetic model by integrating a time function of E_a into the rate equations. We named this model *Refined Avrami* method. Its applications are compared with that of the classic *Avrami* method in the following reactions: pentlandite exsolution from monosulfide solid solution (*mss*), oxidation of *mss*, α- to β- phase transition of nickel monosulfide, oxidation of NiS.

1.7 References

Aagard, P. and Helgeson, H.C. (1982), Thermodynamic and kinetic constrains on reaction rates among minerals and aqueous solutions, I. Theoretical considerations. American Journal of Science, 282, 237-285.

Adamson, A.W. (1990), Physical chemistry of surfaces, 4th ed. Wiley, New York.

Alberty, R.A. (1979), Physical chemistry, Wiley, New York.

Aoki ,K., Tokuda, K., Matsuda, H., Oyama, N. **(**1984), Theory of charge transport within polymer films with uneven thickness coated on electrodes , Journal of Electroanalytical Chemistry, 176, 139-150.

Berner, R.A. (1978), Rate control of mineral dissolution under earth surface conditions. American Journal of Science, 278, 1235-1252.

Broecker, W.S. and Oversby, V.M. (1971), Chemical equilibria in the earth, McGraw-Hill Press, New York.

Burker, J. (1965), The kinetics of phase transformations in metals, Pergamon Press, Oxford.

Castellan, G. W (1983), Physical chemistry, Addison-Wesley, Massachusetts.

Christian, J.W. (1965), The theory of transformations in metals and alloys, Pergamon Press, Oxford.

Cohen, N. (1991), Are Reaction Rate Coefficients Additive? Revised Transition State Theory Calculations for OH+ Alkane Reactions, International Journal of Chemical Kinetics, 23, 397-417.

Diao, J. and Hess, D.W. (2004), Use of angle-resolved XPS to determine depth profiles based on Fick's second law of diffusion: description of method and simulation study Journal of Electron Spectroscopy and Related Phenomena,135,87-104.

Etschmann, B., Pring, A., Putnis, A., Grguric, B.A., and Studer, A. (2004), A kinetic study of the exsolution of pentlandite $(Ni,Fe)_9S_8$ from the monosulfide solid solution (Fe,Ni)S. American Mineralogist, 89, 39-50.

Frost, A and Pearson, R. (1961), Kinetics and mechanism: a study of homogeneous chemical reactions, Wiley Press, New York.

Helgeson, H.C., Murphy, W.M., and Aagaard, P. (1984), Thermodynamic and kinetic constraints on reaction rates among minerals and aqueous solutions. II. Rate constants, effective surface area, and the hydrolysis of feldspar, Geochimica et Cosmochimica Acta, 48, 2405-2432.

Hinshelwood, C.N. (1951), The structure of physical chemistry, Clarendon Press, Oxford.

Hu, Y. (2001), Physical Chemistry, Higher Education Press, Beijing (in Chinese).

Hu, Y. and Sinnott, S.B. (2004), Constant temperature molecular dynamics simulations of energetic particle–solid collisions: comparison of temperature control methods, Journal of Computational Physics, 200, 2004, 251-266.

Kidson G.V. (1961), Some aspects of the growth of diffusion layers in binary systems, Journal of Nuclear Materials, 3, 21-29.

Lasaga, A.C. (1997), Kinetic theory in the earth sciences, Princeton University Press, New Jersey.

Liau, L. C. and Hsieh, Y.P. **(**2005), Kinetic analysis of poly(vinyl butyral)/glass ceramic thermal degradation using non-linear heating functions, Polymer Degradation and Stability, 89, 545-552.

Liu, S.M., Zhang, J., Chen, H.T., and Zhang, G.S. (2005), Factors influencing nutrient dynamics in the eutrophic Jiaozhou Bay, North China, Progress In Oceanography, 66, 66-85.

Lű, R.D. (2003), Principles of Physical Chemistry, ECUST Press, Shanghai (in Chinese).

Wilkins, R.G. (1991), Kinetics and mechanisms of reactions of transition metal complexes, Weinheim Press, New York.

Meek, T.D., Rodriguez, E.J. and Angeles T.S. (1994), Use of steady state kinetic methods to elucidate the kinetic and chemical mechanisms of retroviral proteases, Methods in Enzymology, 241, 127-156.

Meeks, F.R. and Kosenkranius, H. (1962), Determination of the solubility product of CuS in a gel employing the liesegang phenomenon, Journal of Colloid Science, 17, 1-9.

Moore J.W., Pearson R.G. (1981), Kinetics and mechanism, Wiley Press, New York.

Moore, W. (1972), Physical chemistry, Longman, London.

Pechukas**,** P. (1981), Transition State Theory**,** Annual Review of Physical Chemistry, 32, 159-177.

Putnis, A. (1992), Introduction to mineral science, Cambridge University Press, Cambridge.

Rosén J., Schneider, J.M. and Larsson, K. (2005), *Ab initio* molecular dynamics study of ion-surface interactions, Solid State Communications, 134, 2005, 333-336.

Sima-Ella, E., Yuan, G. and Mays, T. (2005), A simple kinetic analysis to determine the intrinsic reactivity of coal chars, Fuel, 84, 1920-1925.

Smith, I.W.M. (1980), Reaction dynamics, Plenum Press, New York.

Sykes, A.G. (1966), Kinetics of inorganic reactions, Pergamon, New York.

Van-Baal C.M. (1985), Kinetics of crystalline configurations: III. An alloy that is inhomogeneous in one crystal direction, Physica A: Statistical and Theoretical Physics, 129, 601-625.

Wang, H., Pring, A., Ngothai, Y., O'Neill, B. (2005a), A low-temperature kinetic study of the exsolution of pentlandite from the monosulfide solid solution using a reined Avrami method, Geochimica et Cosmochimica, 69, 415-425.

Wang, H., Pring, A., Xie, Y., Ngothai, Y., O'Neill, B. (2005b), Phase evolution and kinetics of the oxidation of monosulfide solid solution under isothermal conditions, Thermochim. Acta, 427, 13-25.

Wang, H., Pring, A., Ngothai, Y., O'Neill, B. (2005c), The kinetics of the $\alpha \rightarrow \beta$ transition in synthetic nickel monosulfide, American Mineralogist (accepted).

Wang, H., Pring A., Ngothai, Y., O'Neill, B. (2005d), The mechanism and kinetics of α-NiS oxidation in the temperature range 670-700 ^{o}C, American Mineralogist (in press).

Wu, Q.X. (2004), Principles of Kinetics, He Hai University Press, Nanjing (in Chinese).

Xie, C.F. (2004), Kinetics, 2nd ed., Higher Education Press, Beijing (in Chinese).

Yund, R.A. and Hall, H.T. (1970), Kinetics and mechanisms of pyrite exsolution from pyrrhotite, Journal of Petrology, 11, 381-404.

Yund, R.A. and McCallister, R.H. (1970), Kinetics and mechanisms of exsolution, Chemical Geology, 6, 5-30.

Zhu, S.M. (2000), Introduction to kinetics, ECUST Press, Shanghai (in Chinese).

CHAPTER TWO

Chapter 2: Mineralogy of the Fe-Ni-S and Ni-S systems

2.1 Introduction

Reactions involving nonstoichiometric compounds are often mysterious and complex. The varying composition of these compounds imposes further difficulties in understanding reaction mechanisms and phase relations. In this work, the reaction kinetics of two nonstoichiometric systems was investigated. They are the pyrrhotite group (including monosulfide solid solution) and nickel sulfide minerals.

2.2 Pyrrhotite Group Minerals

2.2.1 Overview

The pyrrhotite group is defined as all the iron monosulfides of the general formula $Fe_{1-x}S$ ($0 < x < 0.125$) that possesses a NiAs type substructure. They exhibit a hexagonal close packed structure with [FeS_6] and [SFe_6] units (Carpenter and Desborough, 1964; Arnold, 1966). This includes troilite (FeS) and the monoclinic and hexagonal pyrrhotites. The pyrrhotites are extremely complex from both a physical and chemical standpoint. They crystallize in the hexagonal or monoclinic systems; troilite (FeS) is hexagonal, whereas pyrrhotite ($Fe_{1-x}S$) may be monoclinic or hexagonal. These minerals usually appear in massive form, and are commonly found in basic igneous or ultrabasic rocks, in hydrothermal mineral deposits, and in contact-metasomatic sediments. Interest in the pyrrhotite group arises from their occurrence in metallurgical processes, their properties, and their common occurrence in many types of ore deposits. They are also of importance in terms of geomagnetism monoclinic pyrrhotite being one of the main magnetic minerals in the earth's crust. Structurally, they are all derivatives of the NiAs structure (Vaughan,

1978; Nesbitt et al., 2002). Pyrrhotite minerals are abundant in nature, and possesses a dark, brownish rusty colour on their surface. They often occur with pyrite (FeS_2), chalcopyrite ($CuFeS_2$), pentlandite ($(Fe,Ni)_9S_8$), and magnetite (Fe_3O_4).

A better understanding of the chemical and physical behaviour of pyrrhotite is of commercial interest for mineral processing industry, as pyrrhotite is one of the major iron ores used as feedstock in flash smelting processes for metal extraction (Wang et al., 2005b).

2.2.2 Polytypes

The most widely used classification for pyrrhotite polytypes is to categorize these NiAs-type derivatives into three groups: troilite, hexagonal pyrrhotite, and monoclinic pyrrhotite.

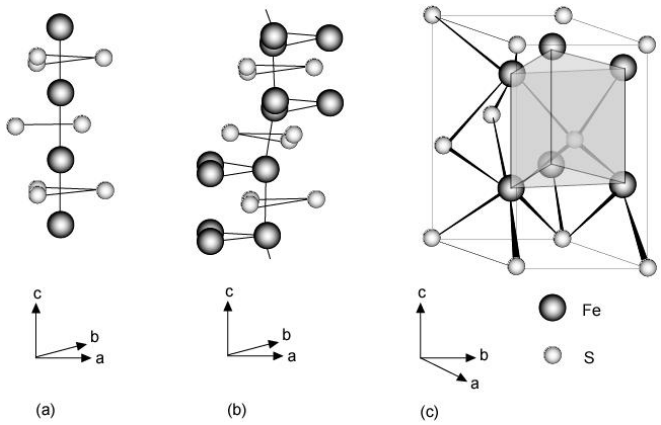

Figure 2.1. (a) Partial configuration of S and Fe atoms along c axis in the NiAs substructure. (b) Partial atom configuration in troilite along c axis. Triangular Fe clusters are surrounded by distorted sulfur octahedra. (c) Fe clusters in the troilite cell, which is derived from the NiAs cell by doubling the *c* axis, with *a* axis deviating by 30^o in ab-plane (Kruse and Mossbauer, 1990; Skinner et al., 2004).

Troilite is a stoichiometric or near stoichiometric iron sulfide ($Fe_{1-x}S$, x = 0~0.05), exhibiting 2C superstructure of NiAs-type ($a = \sqrt{3}A$, c = 2C where A and C are the axes

of the NiAs subcell common to troilite and pyrrhotites), and $P\bar{6}2c$ symmetry below 140^{o}C (Bertaut, 1952; Evans, 1970; Ward, 1970; Kissin and Scott, 1982).

It shows distortions from the ideal NiAs structure type positions (Figure 2.1a and b); triangular groupings of iron atoms are displaced in the *ab*-plane forming contracted and dilated triangular units. The sulfur network is much less distorted with only a slight displacement of one-third of the sulfur atoms along the *c* axis, away from the centre of the Fe cluster (Thomas, 2003). The Fe cluster formed by three Fe atoms on *ab*-plane is shown in Figure 2.1b. Neighboring Fe triangular clusters are positioned in two ways: stacked directly above one another along c axis (Figure 2.1a), and displaced above one another (Figure 2.1b). Thus, a line connecting Fe atoms along *c* axis is alternately parallel to and then inclined to the *c* axis. The position of an iron cluster in the troilite cell is shown in Figure 2.1c. For troilite with the stoichiometric composition (FeS), the Fe-Fe distances in the same iron triangular cluster, directly above one another, and obliquely above one another are 2.925, 2.988, and 2.947 Å respectively (Kruse and Mossbauer, 1990). It has been suggested that the formation of the Fe-Fe cluster results from Fe-Fe bonds formed by 3d electron overlapping when the Fe-Fe separations are below the critical value, 3.0 Å (Kruse and Mossbauer, 1990).

In nature, troilite is not as abundant as other pyrrhotite polytypes. It forms under strong reducing conditions (Evans, 1970). One such occurrence is in swamps, where anaerobic bacteria can reduce sulfate to sulfide. Studies of swamp sediments show only low concentrations of troilite, but an abundance of fine crystalline pyrite (Thomas et al., 2003). However, troilite is found in most iron meteorites where it occurs as large clumps up to 5 cm in diameter. The magnetic moments on ab-planes are antiferromagnetically

ordered at room temperature, and undergo a spin-flip transition (α-transition) at 140^{o}C, where the orientation of magnetic moments flips from perpendicular to the *c* axis to parallel to the *c* axis (Li et al., 1996). Magnetic moment disordering occurs at the Curie temperature (315 ^{o}C), when antiferromagnetic FeS transforms to a paramagnetic structure (β-transition).

The β-transition is accompanied by a phase transformation to the NiAs subcell (1C). The β-transition is a first-order transition (characterised by an abrupt change in the cell lattice). Although the conclusion that FeS undergoes magnetic structure variations during the α- transition is widely accepted, there is dispute about whether or not a structural phase transition accompanies this magnetic transition (Hägg and Sucksdorff, 1933; Arnold, 1969; Ward, 1970; Moffatt, 1984). However, the majority of the research reports since the 1980s indicate FeS adopts the MnP-type structure between 140~315 ^{o}C (between the α and β transitions) (Kruse, 1990; King and Prewitt, 1982). The transition from the troilite (2C) to the MnP-type structure (α- transition) is believed to be a second-order transition (Li et al., 1996). The MnP-type structure can be interpreted as a phase with the subgroup symmetry of troilite. The similarity in the X-ray diffraction patterns of troilite and the MnP-type structure and the nature of continuous change in cell parameters (characteristic of a second order transition) during the α- transition may explain why the MnP-type structure has been overlooked in earlier studies. Recently, high temperature X-ray diffraction was used to distinguish these two similar phases (Li et al., 1996). It has been shown that the α- transition temperature is dependent on the starting stoichiometry of the troilite ($Fe_{1-x}S$, x = 0~0.05). The larger the value of x, the lower the temperature of transition (Li et al., 1996).

Metal-like iron states have been observed in troilite due to higher occupancy of Fe lattice sites compared to the more metal-deficient pyrrhotites, and increased Fe-Fe 3d orbital interactions occur within the constrains of the mineral structure.

Monoclinic pyrrhotite can be perceived as a derivative of FeS following subtraction of one-eighth of the iron atoms. The resultant structure contains alternating layers of full Fe sites and layers of Fe sites with vacancies, thereby lowering the symmetry from hexagonal to monoclinic (Kondoro, 1999). The 4C monoclinic structure may be regarded as the result of a slight distortion of the hexagonal structure (Flahaut, 1972), in which the c axis tilts with respect to the basal ab-plane (Corlett, 1968). The phase Fe_7S_8 adopts a monoclinic structure in which vacancies are confined to every other site in alternate rows of sites within the vacancy layer.

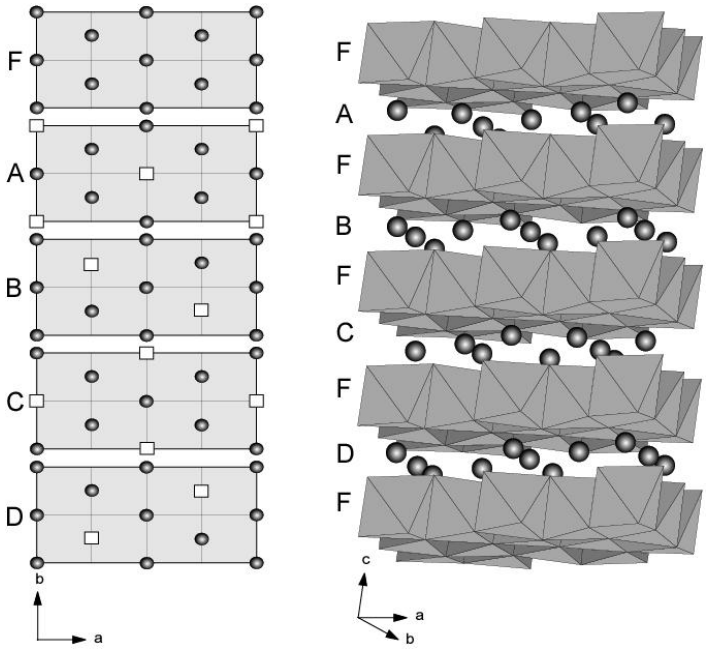

Figure 2.2. 4C monoclinic superstructure of pyrrhotite. (a) four different vacancy arrangements in cation layer, A, B, C, and D. (b) Stacking sequence of vacancy layers and vacancy free layers (Levinson and Treves, 1968; Kondoro, 1999).

The vacancy layers are stacked in an ABCD sequence, quadrupling the unit cell along the stacking direction and leading to a superstructure of 4C. The various vacancy arrangements, A~D, are shown in Figure. 2.2a.

The 4C superstructure of pyrrhotite can be expressed as (…FAFBFCFDF…), where F represents a layer free of cation vacancies (Figure 2.2b). Monoclinic pyrrhotite is not stable at high temperatures.

Monoclinic pyrrhotite shows strong ferrimagnetic behavior. In fact, magnetic structures of all pyrrhotite group minerals are closely related to the ordering of iron atoms and vacancies in the vacancy-bearing layers. The magnetic behaviour of monoclinic pyrrhotite is attributed to the ferromagnetic alignment of cations within layers and the antiferromagnetic coupling between adjacent layers. The presence of vacancies in alternate layers results in an uncompensated moment, leading to ferrimagnetism (Powell et al., 2004).

Although monoclinic pyrrhotite is generally denoted as Fe_7S_8, it has a measurable composition range at room temperature (Carpenter and Desborough, 1964). There is a second modification of the Fe_7S_8 phase that can be described in terms of a trigonal supercell (2A, 3C) (Fleet, 1968; Tokonami et al., 1972; Li and Franzen, 1996). This phase is considered to be a metastable form at room temperature, as it normally exists in quenched samples but has not been found in nature. The stability field of 3C is shown in the MC (when M = 3) zone of the phase diagram (see Figure 2.3). The 4C structure has been found only in natural pyrrhotite that has undergone cation and vacancy ordering processes over geological time (Li et al., 1996). In other words, rapid cooling of Fe_7S_8 from high temperature results in the formation of a well-ordered 3C structure, whereas a

4C structure is formed when the cooling rate is slow (Ericsson et al., 1997). The 4C and 3C structures of Fe_7S_8 differ not only in the arrangement of vacancies, but also in the type of Fe-clustering.

Similar to monoclinic pyrrhotites, vacancy-bearing layers in hexagonal pyrrhotites determine the structural and magnetic properties of the various phases noted (from monoclinic 4C to hexagonal NC structures; see Figure 2.3 for the definition of NC). Bertaut (1953) observed a repulsion effect among vacancies in pyrrhotite. This observation was further developed by Powell (1983) into the *Vacancy Avoidance* theory, which has been used to study the superstructures of pyrrhotite. At high temperatures, the vacancy distribution is random and the unit cell of pyrrhotite is the NiAs subcell, the 1C structure (Morimoto, 1978). When the temperature decreases, the vacancies start to order and superstructures of the NiAs subcell form (Nakazawa and Morimoto, 1975). Below 300^{o}C, the diffusion of vacancies is effectively inhibited, and high-temperature structures are locked in metastable states (Ono et al., 1962; Marusak and Tongson, 1979; Igaki et al., 1981, 1982). Many natural hexagonal pyrrhotites are formed during a sudden geological cooling process. The superstructures of the NiAs subcell, except for 4C and 2C, contain nonintegral X-ray reflections attributed to the intergrowth of differently ordered domains (Pierce and Buseck, 1974). Formation of superstructures does not appear to affect the short-range atom configurations, although detailed structural refinements of many superstructures are yet to be undertaken. Many of the hexagonal superstructures have very close stoichiometries but they appear to behave as separate phases (or polytypes) and were normally treated as such when delineating phase diagrams. Nakazawa and Morimoto (1970, 1971) sorted the numerous superstructures

into five categories according to their multiplicities of the NiAs sublattice (Nakazawa and Morimoto, 1970, 1971). These categories of the superstructures are: (1) 2C for troilite, (2) 4C for monoclinic pyrrhotite, (3) NC (a = 2A; c = NC, N varies continuously between 5.0 and 11.0 (Nakazawa and Morimoto, 1970, 1971; Morimoto et al., 1975), (4) MC (a = 2A; c = MC, M varies between 3.0 and 4.0), (5) NA (a = NA; c = 3C, N varies continuously between 40 and 90). Note A, C are the *a* and *c* parameters of NiAs subcell. The most well studied superstructures in nature, 5C (Fe_9S_{10}), 6C ($Fe_{11}S_{12}$), and 11C ($Fe_{10}S_{11}$), belong to the NC category (Morimoto et al., 1975). Although 5C, 6C, and 11C are crystallographically distinguishable, they are treated as one phase, NC, in the studies of phase relations. This is because they act as a single phase during phase transitions, and their compositions fall into a very narrow band (47.37 to 47.83 at.% of Fe) (Nakazawa and Morimoto, 1970, 1971; Morimoto et al., 1975). These superstructures are best described in terms of stacking of fully occupied and ordered defective iron layers normal to the c-axis. Each structure is characterized by a regular succession of such layers, corresponding to an integral supercell multiplicity N, where c = NC. The multiplicity N is related to the general chemical formula $Fe_{m-1}S_m$ (m >8) by N = 0.5m (when m has a even value), or N = m (when m has an odd value). This formulism serves for the convenience of describing the superstructures in pyrrhotite. In fact, pyrrhotites with nonintegral multiplicity superstructure are more common, as the m (as in $Fe_{m-1}S_m$) is not necessary integer and changes continuously with both composition and temperature. Stacking disorders between filled and vacancy bearing layers gives rise to non-integral m values, and thus to an apparently incommensurate c-axis repeat (Grønvold and Stølen, 1992). These pyrrhotites are often referred to just as hexagonal pyrrhotite, and have

compositions in the region between troilite and monoclinic pyrrhotite. These superstructures can either expressed as Fe_9S_{10}, $Fe_{10}S_{11}$, $Fe_{11}S_{12}$ or a mixture of the stoichiometric phases with troilite or with monoclinic pyrrhotite (Morimoto et al., 1975; Kondoro, 1999).

2.2.3 Binary Phase Diagram

The phase relations in the FeS-FeS_2 system have been the subject of numerous investigations (Arnold, 1969; Yund and Hall, 1970; Tokonami et al., 1972; Kissin and Scott, 1982). There is general agreement between a large number of studies on the phase relations at higher temperatures (> 350^{o}C), but considerable contradictory evidence in the lower temperature ranges (<350^{o}C). It is a daunting task to determine a solvus between the various pyrrhotite polymorphs due to the similarity of their powder diffraction patterns, as they form a series of chemically and closely related superstructure phases (Pierce and Buseck, 1974). At low temperatures, these pyrrhotite supercell phases may form metastable phase assemblages, which seriously affect the accuracy of determination of an equilibrium solvus. Some difficulties also occurred in the determination of the phase solvus at high temperatures, as some high-temperature phases cannot be quenched for room temperature measurement. The preservation of high-temperature crystal structures with pyrrhotite phases becomes problematic when the temperature (T) exceeds 308^{o}C (Corlett, 1968; Nakazawa and Morimoto, 1970). For sulfur rich samples, the pyrrhotite compositions will invariably transect the equilibrium solvus, and produce large deviation from equilibrium compositions. For some pyrrhotite compositions ranges, no matter how fast the pyrrhotite samples are quenched from high temperature (T > 308^{o}C) to room temperature, an oversaturation induced phase exsolution (e.g. pyrite) might more

or less affect the preservation of the high temperature phase structure and composition. This problem has been successfully overcome by using high-temperature single crystal (or power) X-ray diffraction methods (Yund and Hall, 1970; Nakazawa and Morimoto, 1971; Kissin and Scott, 1982).

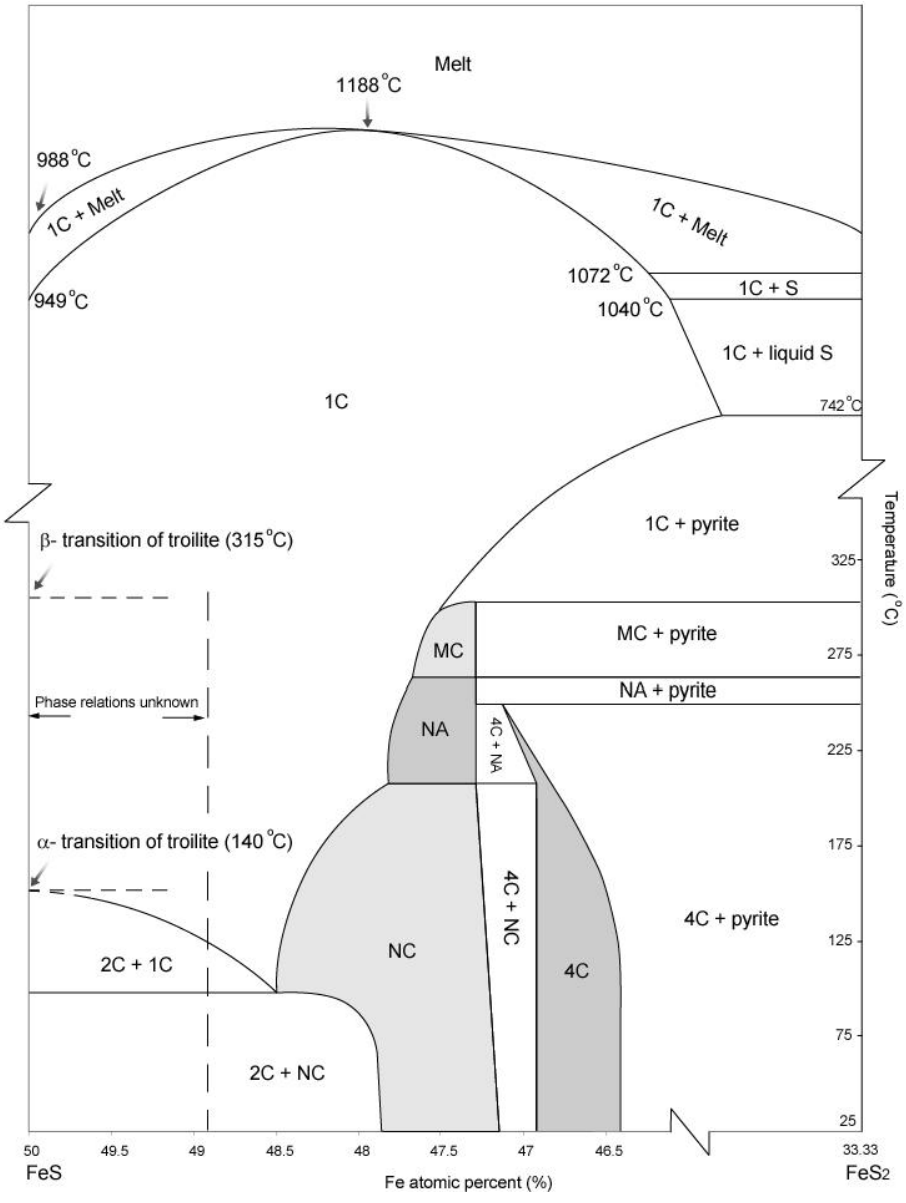

Figure 2.3. FeS-FeS_2 phase diagram (Arnold, 1962, 1969; Tokonami et al., 1972; Kissin and Scott, 1982; Grønvold and Stølen, 1992)

Kissin and Scott (1982) systematically investigated the low temperature phase diagram near the most metal deficient compositions using a hydrothermal recrystallizaion method. This method largely overcomes the problem of the long annealing requirement to achieve reaction equilibrium by dry synthesis experiment (Scott and Barnes, 1971; Scott, 1975; Barnes, 1971). It gives more reliable results for phase relations. Their data and earlier reports on the pyrrhotite phase relations were summarized to give a relatively accurate and complete phase relations for low temperatures (Kissin and Scott, 1982). Combining the high temperature phase diagram, Figure 2.3 gives the complete FeS-FeS_2 phase relations covering temperature range of 25 ~ 1200^{o}C.

The solvus between 1C pyrrhotite and pyrite continues below 750 ^{o}C along the slope proposed by Toulmin and Barton (1964) and Arnold (1962) to 315 ^{o}C, where the 1C phase starts to transform into MC superstructure (Arnold, 1962). M = 3.0 ~ 3.3. This temperature coincides with the β-transition temperature. The solvus then proceeds along a similar slope down to 262^{o}C, with the exsolution of NA superstructure. In the narrow temperature range from 262 to 254^{o}C, NA pyrrhotite coexists with pyrite if the initial bulk composition contains less than 47.5 atomic percent iron (%). The stability field of monoclinic pyrrhotite near 254^{o}C is very narrow and many earlier researchers considered it restricted to Fe_7S_8 (46.67 at.% Fe) (Corlett, 1968), but it has been found that the monoclinic pyrrhotite is able to exist over a wider composition range at lower temperatures (e.g. 46.4 ~ 46.9 at.% Fe at 115 ^{o}C) (Kissin and Scott, 1982). Below 209^{o}C, NA pyrrhotite will be transformed into NC structure, and its stable composition field becomes wider with increasing temperature until around 90~100^{o}C, a eutectic temperature, where three phases coexist (1C + 2C + NC). Below the eutectic temperature,

2C superstructure (troilite) coexist with NC pyrrhotite, of composition 47.8 at.% Fe at room temperature (Arnold, 1969). Viewed under a crossed polars microscope, the images of the 2C and NC phases go to extinction simultaneously, indicating that the *c* axes of these two phases are parallel in the intergrowth (Carpenter and Desborough, 1964). The temperature at which pyrite melts incongruently (742^{o}C) is from Kullerud and Yoder (1959).

Arnold (1962) proposed an idea of "*Pyrrhotite Geothermometer*", which utilizes the temperature dependence of the composition of pyrrhotite coexisting with pyrite in a sulfide ore. The fundamental assumption of this pyrrhotite geothermometer was that a unique composition of hexagonal pyrrhotite coexists with pyrite along the pyrrhotite-pyrite solvus (Figure 2.3) (Arnold, 1962; Kissin and Scott, 1982). However, the geothermometer is only valid for low temperatures ($T < 314^{o}$C), as pyrrhotite-pyrite ores at higher temperatures are unquenchable (Kissin and Scott, 1982). The pyrrhotite solvus exhibits a strong tendency to re-equilibrate with decreasing temperature.

Li and Franzen (1996) stated that composition of troilite could vary in a narrow range (FeS to $Fe_{0.95}S$). The phase transitions for stoichiometric troilite (FeS) have been well studied (troilite → MnP-type ,140 ^{o}C → 1C pyrrhotite, 315^{o}C) . However, the phase transitions studies for nonstoichimetric troilite (say $Fe_{0.95}S$) have only been conducted for α-transition (troilite → MnP-type) (Craig, 1966; Scott and Kissin, 1973; Sugaki et al., 1977). The orthorhombic MnP-type structure is a distorted variant of the NiAs-type structure with pronounced metal-metal zigzag chains (see Figure 2.4). In these earlier studies for α-transition solvus, the MnP-type phase was treated as 1C pyrrhotite, which has been proven imprecise. Figure 2.3 does not include the β-transition curves for the

range of 49.0 ~ 50.0 at. % Fe, as there is little data related to the β-transition solvus extending to the troilite composition $Fe_{0.95}S$ ~FeS.

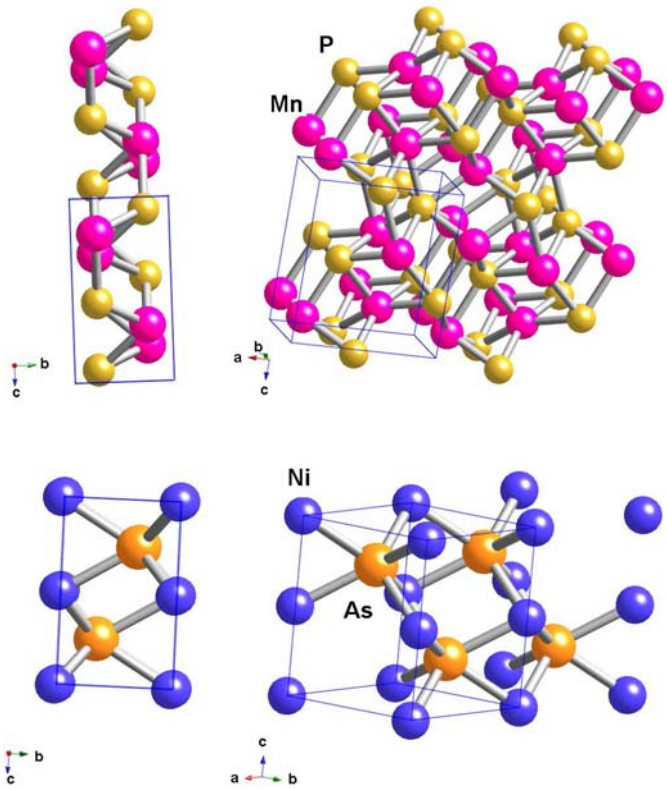

Figure 2.4. A comparison of the MnP-type structure (space group: Pnma; Fjellvag and Kjekshus, 1984) with the NiAs-type structure (space group: P 6_3/mmc; Yund, 1962). The MnP-type structure shows distinct metal-metal zigzag chain along *c* axis compared to NiAs.

The trigonal pyrrhotites (3C, see Section 2.2) here, is denoted MC instead of 3C, as in nature, the trigonal pyrrhotites normally exhibits a multiplicity (M) slightly larger than 3 (3< M< 4). Thus, it is more accurate to use MC in the phase diagram.

The phase diagram also produces guidance for the estimation of coexisting phases in an assemblage. At low temperatures, with the increase in iron content in bulk pyrrhotite compositions, the possible assemblage shifts from (4C + NC) to (2C + NC) (Hayas and Mariko, 1961; Mukaiyama and Izawa, 1966; Morimoto and Nakazawa, 1968; Vorma, 1970; Izawa and Mukaiyama, 1972; Morimoto et al., 1975) (Figure 2.3).

2.2.4 Ternary Phase Diagram

When a reasonable amount of Fe atoms in the pyrrhotite structures are replaced by other cations, it would be more appropriate to call these phases monosulfide solid solution (*mss*).

There are numerous possible substitutional cations, e.g. Ni, Co, Cu, Pt, and Pd etc. (Li et al., 1996). In nature, however, the major cation substitutions for pyrrhotites are Ni and Co. *mss* can be considered as binary or ternary solid solution between $Fe_{1-x}S$ (pyrrhotite), α-NiS_{1-x}, and $Co_{1-x}S$ (jaipurite). In this work, we focus on Fe-Ni-S system.

At high temperatures, $Fe_{1-x}S$ and $Ni_{1-x}S$ form a continuous solid solution but below 610^{o}C cation ordering and atomic diffusion cause the exsolution of pentlandite. The possible *mss* composition range still spans the complete solution between the two end members ($Fe_{1-x}S$ and $Ni_{1-x}S$). The studies by Misra and Fleet (1973) and Craig (1973) show that *mss* is continuous solution down to 300^{o}C, below this temperature two immiscible *mss* phases appear; one is more Fe-rich, the other is more Ni-rich (Craig, 1973; Misra and Fleet, 1973). With continuous decrease in temperature, the more Fe-rich *mss* phase becomes progressively enriched in Fe, and the more Ni-rich *mss* phase decomposes to an intergrowth of pentlandite and pyrrhotite. Numerous experimental results show that at low temperatures (< 300^{o}C) up to 17% at.% Ni can remain in the *mss*. This is in contradiction to the 0.2 to 0.7 at.% Ni in naturally formed *mss*/pyrrhotite (Craig, 1973; Misra and Fleet; 1973; Farrell and Fleet, 2002; Etschmann et al., 2004). Clearly, cation ordering and atom diffusion in *mss* may proceed even at low temperatures. The readjustment of the *mss* compositions over a geological time results in the substantially Ni free *mss*/pyrrhotite compositions.

The *mss* stability field in Fe-Ni-S ternary system depends largely on temperature, expanding from a more Fe enriched domain at higher temperatures ($T \geq 1100^oC$) to a bivariant field covering all Fe: Ni ratios at low temperatures (e.g. $T = 650^oC$) (Figure 2.5a and b). The *mss* stability field at 1100^oC extends from 36.5 to 43.3 wt% sulfur along Fe-S joint, protruding into the ternary system up to a composition with maximum Ni content of 14 wt% (Figure 2.5a) (Kullerud et al., 1969). The relatively Fe rich composition of *mss* above 1100^oC results in a nickel enriched liquid coexisting with the *mss* at the same temperature. This solid solution becomes complete between $Fe_{1-x}S$ and $Ni_{1-x}S$ below 992^oC and remains so over a large temperature region (Kullerud, 1963; Clark, 1966). Figure 2.5a, b, and c show the progressive extension of *mss* stability field towards the Ni-S joint with decreasing temperature from 1100 to 900^oC. Kullerud (1963) showed that above 1083^oC a liquid immiscibility field spans the sulfur-rich portion of the ternary system with a homogeneous liquid field located in the center (Figure 2.5a) (Kullerud, 1963). On cooling the liquid immiscibility field shrinks and finally disappears at 991^oC, as well $(Ni,Fe)S_2$ becomes stable with liquid below this temperature (Figure 2.5c) (Kullerud et al., 1969; Clark and Kullerud, 1963). Cooling below 900^oC results in a gradual narrowing of the *mss* + sulfur liquid divariant field, and continuous expansion of *mss* field, but the central homogeneous liquid shrinks drastically (Kullerud, 1963). On cooling to 610^oC, pentlandite starts to exsolve from the system. Figure 2.5e shows the stability field of pentlandite, *mss*, and *mss* + pentlandite bivariant field at 550^oC. Studies by Naldrett et al. (1967) of the *mss* stability field have shown that its ability to tolerate variation in the metal to sulfur ratio decreases rapidly with decreasing temperature (Naldrett et al., 1967). The *mss* field starts to break off from the Ni-S joint and retreats

toward the Fe-S joint with further cooling below 300^{o}C. Figure 2.5f shows the stable equilibrium composition of *mss* at 130^{o}C is $Fe_{1-x}S$ (Kullerud and Yund, 1969).

2.3 Nickel Monosulfides

The two well-studied forms of nickel monosulfides are β-NiS (millerite) and α-NiS. β-NiS, a trigonal/rhombohedral structure crystal, is naturally formed as a low temperature hydrothermal or alteration product of other nickel minerals. β-NiS is also called millerite after W. H. Miller, the crystallographer who introduced the system of crystallogrphic indices. Compared with α-NiS, β-NiS is always referred to as the low-temperature form of NiS (< 652 K). It has a high metallic conductivity and is speculated to possess a diamagnetic structure (Krishnakumar et al., 2002). Millerite is the only form of NiS found in nature and it is of metallurgical interest, as it is often associated with other important nickel-iron or copper-iron ores (Power, 1981; Hubli et al., 1995; Legrand et al., 1998). Millerite generally occurs in fine hairlike or capillary crystals, which give it the synonyms: “hair pyrite” and “capillary pyrite”. β-NiS has a near equimolar composition NiS, whereas α-NiS has a variable stoichiometry range, $\alpha\text{-}Ni_{1-x}S$ (Grønvold and Stølen, 1999). The maximum *x* value (in $\alpha\text{-}Ni_{1-x}S$) varies with temperature, and has not been precisely determined (Grønvold and Stølen, 1999; Stølen et al., 1994; Rau, 1975; Kullerud and Yund, 1962).

The high temperature phase, $\alpha\text{-NiS}/\alpha\text{-}Ni_{1-x}S$, has the NiAs-type hexagonal structure, is quenchable and remains a metastable phase under ambient conditions.

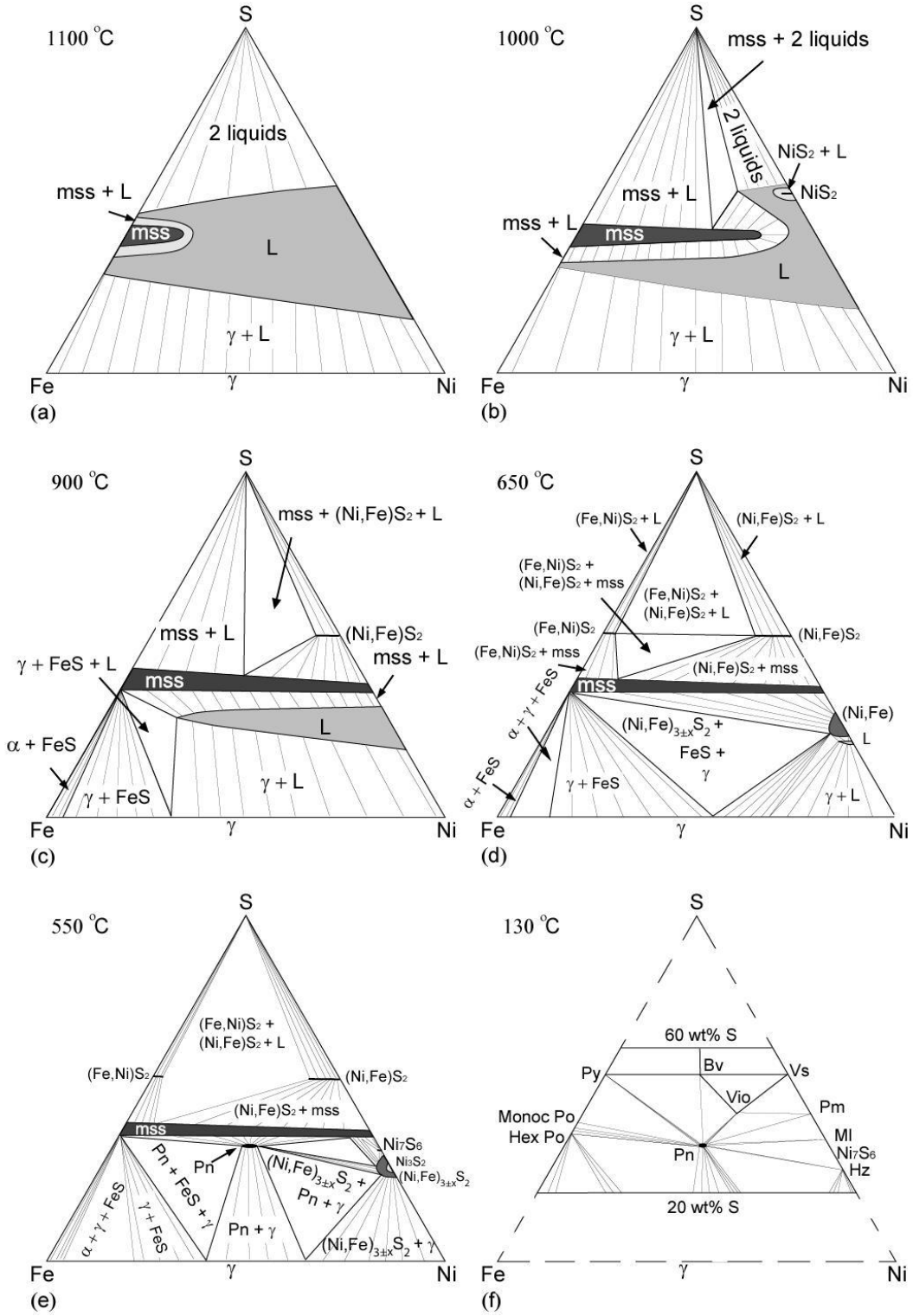

Figure 2.5. Phase relations in the Fe-Ni-S system at (a) 1100°C, (b) 1000°C, (c) 900°C, (d) 650°C, (e) 550° C, and (f) 130°C (after Kullerud and Yund, 1969). Note: for the purpose of clear illustration, some parts of the diagrams are enlarged.

There have been numerous studies on this metastable α-NiS/α-$Ni_{1-x}S$ at low temperatures due to the distinct metal→ semiconductor transition (MS transition) of α-NiS at 265 K, below which a small band gap occurs and the gap progressively increases with decreasing temperature (Sparks and Komoto, 1963; Nakamura et al., 1994; Okamura et al., 1999). α-NiS/α-$Ni_{1-x}S$ also plays an important role in studies of the crystal chemistry and phase relations in metal sulfides systems because of its relationship with other economically important Ni bearing sulfide minerals, and especially because α-NiS and pyrrhotite are structurally related so that α-NiS can be considered as a compositional Ni end-member of nickeliferous pyrrhotite, $(Ni,Fe)_{1-x}S$ (Legrand et al., 1998; Nesbitt and Reinke, 1999). The NiAs structure of α-NiS exhibits a paramagnetic-antiferromagnetic transition at –8 ^{o}C (Néel temperature). The sublattice magnetization goes from zero to full saturation on cooling through –8 ^{o}C. Previous powder diffraction results and the measurements of magnetic and electrical properties through the transition indicate that the metal→ semiconductor transition of α-NiS is first-order (Sparks and Komoto, 1963, 1967, 1968). In the antiferromagnetic state, the moments of Ni in a hexagonal layer are coupled ferromagnetically within (001) planes and antiferromagnetically between adjacent (001) planes. This makes the magnetic unit cell of α-NiS identical to the crystal unit cell (Trahan and Goodrich, 1970). The metal→ semiconductor transition temperature (T_{MS}) is a strong function of composition, dropping from –8 ^{o}C for α-NiS to –198 ^{o}C for α-$Ni_{0.97}S$ (Sparks and Komoto, 1968). This transition temperature (T_{MS}) also is affected by pressure, decreasing rapidly with increasing pressure (Anzai and Ozawa, 1968; McWhan et al., 1972). Nakamura and Fujimori (1993) reported the opposite effects by introducing

small amount of Ni and Co impurities to "adjust" the T_{MS}. Ni increases T_{MS} whereas Co decreases T_{MS}. There is some disagreement about the structures of α-phase below and above the metal→ semiconductor transition temperature. Many researchers believe there is no crystal structure modification of the α-phase during the metal→ semiconductor transition. However, Trahan and Goodrich (1970) discussed a possible subtle change in the lattice symmetry during the MS transition of α-NiS/α-$Ni_{1-x}S$, from $P6_3/mmc$ above T_{MS} to $P6_3mc$ below T_{MS}.

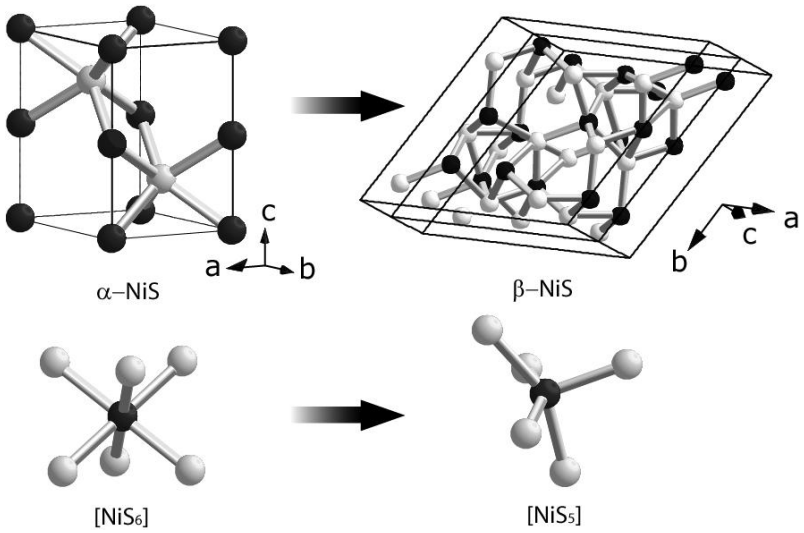

Figure 2.6. Unit cells of α- and β-NiS plotted using the structural information of Vaidya (1976) and Grice and Ferguson (1974) respectively. The schematic graph shows the octahedrally coordinated unit $[NiS_6]$ in α-NiS becomes $[NiS_5]$ in β-NiS.

Upon heating, the low-temperature stable phase (millerite) transforms to the high-temperature form, α-NiS, at 379 ^oC (Kullerud and Yund, 1962). This transition temperature ($T_{\beta-\alpha}$) was measured at ambient pressure. Sowa et al. (2004) reported the phenomenon of a strong pressure dependence of $T_{\beta-\alpha}$. The temperature for the transition from millerite to NiAs-type NiS decreases dramatically with increasing pressure. Owing to the higher compressibility of β-NiS (millerite) compared with that of the α-phase, the

NiAs-type structure is believed to be unstable at high pressures. The coordination of Ni changes from 5 (in β-NiS structure) to 6 (in α-NiS structure) during the β- to α-phase transition (shown in Figure 2.6). This β- to α-phase is a reconstructive transition, involving breaking and rearranging Ni-S bonds. As the compositional range of the α-phase is wider than that of the β-phase, the equilibrium compositions of α- and β- phases depend on whether the transition is from α- to β-phase or from β- to α-phase. For the transition from β-NiS to α-NiS, all the β-phase transforms into the α-phase with no variations in composition. For the transition from a nickel deficient α- $Ni_{1-x}S$ to β-NiS, the exsolution of more nickel rich β-NiS from the nickel deficient α- $Ni_{1-x}S$ host render the α-phase host even more deficient in Ni. The present study attempts to reconcile the ambiguities regarding the stoichiometry effect on the transition kinetics of the α- to β-phase transition at ambient pressure.

2.4 References

Anzai, S., Ozawa, K. (1968) Effect of Pressure on the Magnetic and Electrical Transition Point of the NiAs-Type NiS. Journal of the Physical Society of Japan, 24, 271-274.

Arnold, R.G. (1962), Equilibrium relations between pyrrhotite and pyrite from 325 to 743^{o}C. Economic Geolology, 57, 72-90.

Arnold, R.G. (1966), Mixtures of hexagonal and monoclinic pyrrhotite and the measurement of the metal content of pyrrhotite by X-ray diffraction. American Mineralogist, 51, 1221-1227.

Arnold, R.G. (1969), Pyrrhotite phase relations below 304 ± 6^{o}C at <1 atm. Total pressure. Economic Geology, 64, 405-419.

Barnes, H.L. (1971), Investigation in hydrothermal sulfide system in Ulmer, G.C., ed., Research techniques for high pressure and high temperature. New York, Springer-Verlag, p317-355.

Bertaut, E.F. (1952), La structure de la pyrrhotite Fe_7S_8: Acad Sci [Paris], Comptes Rendus, v234, p1295-1297.

Bertaut, E.F. (1953), Contribution a l'étude des structures lacunaires: la pyrrhotite. Acta Crystallographica, 6, 557-561 (in French).

Carpenter, R.H. and Desborough, G.A. (1964) Range in solid solution and structure of naturally occurring troilite and pyrrhotite. American Mineralogist, 49, 1350-65.

Clark, L.A., Kullerud, G., (1963), The sulfur-rich portion of the Fe-Ni-S system. Economical Geology, 58, 853-885.

Clark, A.H., (1966), Stability field of monoclinic pyrrhotite: Appl. Earth Sci., Transactions of the Institute of Mining and Metallurgy B, 75, B232-B235.

Corlett, M. (1968), Low-iron polymorphs in the pyrrhotite group. Zeitschrift fur Kristallographie, 126, 124-134.

Craig, A.H. (1966), Stability field of monoclinic pyrrhotite. Transactions of the Institute of Mining and Metallurgy B, 75, 232-235.

Craig, J.R. (1973), Pyrite-pentlandite assemblages and other low temperature relations in the Fe-Ni-S system. American Journal of Science, 273-A, 496-510.

Ericsson, T., Amcoff, Ö., and Nordblad, P. (1997), Superstructure formation and magnetism of synthetic selenian pyrrhotite of $Fe_7(S_{1-y}Se_y)_8$, $y \leq 1$ composition. European Journal of Mineralogy, 9, 1131-1146.

Etschmann, B., Pring, A., Putnis, A., Grguric, B.A., Studer, A., (2004), A kinetic study of the exsolution of pentlandite $(Ni,Fe)_9S_8$ from the monosulfide solid solution (Fe,Ni)S. American Mineralogist, 89, 39-50.

Evans, H.T. (1970), Lunar troilite: Crystallography. Science, 167, 621-623.

Farrell, S.P., Fleet, M.E. (2002), Phase seperation in $(Fe,Co)_{1-x}S$ monosulfide solid-solution below 450^{o}C, with consequences for coexisting pyrrhotite and pentlandite in magmatic sulfide deposits. Canadian Mineralogist, 40, 33-46.

Fjellvag, H., Kjekshus, A. (1984), Magnetic and structural properties of transition metal substituted MnP. Acta Crystallographica A, 38, 563-573.

Flahaut, J. (1972), Transition metal chalcogenides. In L.E.J. Roberts, Ed., MTP International Review of Science, Solid State Chemistry, Inorganic Chemistry Series One. Butterworths University Park Press, London.

Fleet, M.S. (1968), On the lattice parameters and superstructures of pyrrhotites. American Mineralogist, 53, 1846-1855.

Genkin, A. (1971), Some replacement phenomena in copper-nickel sulphide ores, Mineralium Deposita, 6, 348-355.

Grice, J.D., and Ferguson, R.B. (1974), Crystal structure refinement of millerite (β-NiS). Canadian Mineralogist, 12, 248-252.

Grønvold F., Stølen S. (1992), Thermodynamics of iron sulfides II. Heat capacity and thermodynamic properties of FeS and $Fe_{0.875}S$ at temperatures from 298.15 to 1000 K, of $Fe_{0.98}S$ from 298.15 to 800 K, and of $Fe_{0.89}S$ from 298.15 to about 650 K. Thermodynamics of ormation. Journal of Chemical Thermodynamics, 24, 913-936.

Grønvold, F. and Stølen, S. (1999), Heat capacity and thermodynamic properties of millerite from 289.15 to 660 K and NiAs-type nickel(II) sulfide from 260 to 1000 K. Thermodynamics of the NiAs-type to millerite transition. Thermochimica Acta, 266, 213-229.

Hayas, K. and Mariko, T. (1961), On the thermal-metamorphism of the orebody of the Yanahara mine. Geological Society of Japan, 67, 1-13.

Hägg, G. and Sucksdorff, I. (1933), Die Kristallstruktur von Troilite und Magnetkies. Zeitschrift fur Physikalische Chemie B, 22, 444-452.

Hubli, R.C., Mukherjee, T.K., Venkatachalam S., Bautista, R.G., and Gupta, C.K. (1995), Kinetics of millerite dissolution in cupric chloride solutions. Hydrometallurgy, 38, 149-159.

Igaki, K., Sata, M., and Shinohara, T. (1981), Mössbauer study on the iron vacancy distribution in iron sulfide $Fe_{1-x}S$ ($0.083 \leq x \leq 0.125$). Transactions of Japanese Institute of Metals, 22, 627-632.

Igaki, K., Sata M., and Shinohara, T. (1982), Mössbauer study on the iron vacancy in iron sulfide $Fe_{1-x}S$. Transactions of Japanese Institute of Metals, 23, 221-228.

Izawa, E. and Mukaiyama, H. (1972), Thermally metamorphosed sulfide mineral deposits in Japan. The 24th International Geological Congress, Montreal, sec.4, 455-462.

Kissin, S.A., and Scott, S.D., (1982), Phase relations involving pyrrhotite below 350^{o}C. Economic Geology, 77, 1739-1754.

King, H.E. and Prewitt, C.T. (1982), High-pressure and high-temperature polymorphism of iron sulphide (FeS). Acta Crystallographica B, 38, 1877-87.

Kondoro, J.W.A., (1999), Mossbauer study of vacancies in natural pyrrhotite. Journal of Alloys and Compounds, 289, 36-41.

Krishnakumar, S.R., Shanthi, N., and Sarma, D.D. (2002), Electronic structure of millerite NiS. Physical Review B, 66, 115105-115110.

Kruse, O. (1990), Mossbauer and X-ray of the effects of vacancy concentration in synthetic hexagonal pyrrhotites. American Mineralogist, 75, 755-763.

Kübler, L. (1982), A continuous phase grading in a “monocrystalline” pyrrhotite, Physics and Chemistry of Minerals, 8, 8-13.

Kullerud, G. and Yoder, H.S. (1959), Pyrite stability relations in the Fe-S system. Economic Geology, 54, 533-572.

Kullerud, G., (1963), The Fe-Ni-S system: Carnegie Inst. Wash. Year Book 62, 175-189.

Kullerud, G., Yund, R.A. (1969), Moh G.H., Phase relations in the Cu-Fe-S, Cu-Ni-S, and Fe-Ni-S system. Economic Geology Monograph, 4, 323-343.

Legrand, D.L., Nesbitt H.W., Bancroft, G.M. (1998) X-ray photoelectron spectroscopic study of a pristine millerite (NiS) surface and the effect of air and water oxidation. American Mineralogist, 83, 1256-1265.

Levinson, L.M. and Treves, D. (1968) Journal of Physics and Chemistry of Solids, 29, 2227-2238.

Li, F., Franzen, H. F. (1996), Phase transitions in near stoichiometric iron sulfide. Journal of Alloys and Compounds, 238 73-80.

Li, F. and Franzen, H. F. (1996), Ordering, Incommensuration, and Phase Transitions in Pyrrhotite. PII: A High-Temperature X-ray Powder Diffraction and Thermomagnetic Study. Journal of solid-state chemistry, 126, 108-120.

Li F., Franzen H. F. and Krame M., (1996), Ordering, Incommensuration, and phase Transitions in Pyrrhotite. Part I: A TEM Study of Fe_7S_8. Journal of solid-state chemistry, 124, 246-271.

Marusak, L.A., and Tongson, L.L. (1979), Soft X-ray emission and Auger electron spectroscopic study of FeS, Fe0.9S, Fe0.875S, and Fe0.5S. Journal of Applied Physics, 50, 4350-4355.

McWhan, D.B., Marezio, M., Remeika, J.P., and Dernier, P.D. (1972), Pressure-Temperature Phase Diagram and Crystal Structure of NiS. Physical Review B, 5, 2552-2555.

Misra, K.C., Fleet, M.E. (1973) The chemical compositions of synthetic and natural pentlandite assemblages. Economic Geology, 68, 518-539.

Morimoto, N. (1978), Direct observation of the superstructures of nonstoichiometric compounds by high resolution electron microscopy. Memoirs of the Institute of Science and Industrial Research, Osaka University, 36, 45-59.

Morimoto, N., Gyobu, A., Tsukuma, K., and Koto, K. (1975), Crystallography and stability of pyrrhotites. Economic Geology, 70, 824-833.

Morimoto, N. and Nakazawa, H. (1968), Pyrrhotites: synthetics having two new superstructures. Science, 161, 577-579.

Mukaiyama, H. and Izawa, E. (1966), Phase relations of pyrrhotite, Mining Institute of Kyushu Journal, 34, 194-213.

Moffatt, W.G (1984), The Handbook of Binary Phase Diagrams vol.3, General Electric, New York, p37-24.

Nakamura, M., Sekiyama, A., Namatame, H., Kino, H., and Fujimori, A. (1994), Opening of a correlation-induced band gap in NiS. Physical Review Letters, 73, 2891-2894.

Nakazawa, H. and Morimoto, N. (1975), Direct observation of metal vacancies by high-resolution electron microscopy. Part I: 4C type pyrrhotite (Fe7S8). American Mineralogist, 359-366.

Nakazawa, H. and Morimoto, N. (1970), Pyrrhotite phase relations below 320^{o}C. Japanese Academic Proceeding, 46, 678-683.

Nakazawa, H. and Morimoto, N. (1971), Phase relations and superstructures of pyrrhotite, $Fe_{1-x}S$. Materials Research Bulletin, 6, 345-358.

Naldrett, A.J., and Kullerud, G. (1967), A study of the Strathcona mine and its bearing on the origin of the nickel-copper ores of the Sudbury district, Ontario. Journal of Petrology, 8, 453-534.

Nesbitt, H.W., Reinke, M. (1999), Properties of As and S at NiAs, NiS, and $Fe_{1-x}S$ surfaces, and reactivity of niccolite in air and water. American Mineralogist, 84, 639-649.

Nesbitt, H.W., Schaufuss, A.G., Bancroft, G.M., and Szargan, R. (2002), Crystal orbital contributions to the pyrrhotite valence band with XPS evidence for weak Fe-Fe π bond formation. Physics and Chemistry of Minerals, 29, 72-77.

Okamura, H., Naitoh, J., Nanba, T., Matoba, M., Nishioka, M., Anzai, S., Shimoyama, I., Fukui, K., Miura, H., Nakagawa, H., Nakagawa, K., and Kinoshita, T. (1999), Optical study of the metal-nonmetal transition in $Ni_{1-\delta}S$. Solid State Communications, 112, 91-95.

Ono K., Ito A., and Hirahara, E. (1962), Mössbauer study of hyperfine field quadrupole interaction, and isomer shift of Fe57 in FeS1.00, FeS1.05 and FeS1.07, Journal of Physics Society of Japan, 17, 1615-1620.

Pierce, L. and Buseck, P.R. (1974), Electron imaging of pyrrhotite superstructures, Science, 186, 1209-1212.

Power, G.P. (1981), The electrochemistry of the nickel sulfides. I. NiS. Australian Journal of Chemistry, 34, 2287-2296.

Powell, A. V., Vaqueiro, P., Knight, K.S., Chapon, L. C., and Sánchez, R. D. (2004), Structure and magnetism in synthetic pyrrhotite Fe_7S_8: A powder neutron-diffraction study. Physical Review B, 70, 014415-1-10.

Putnis, A. and McConnell, J.D.C. (1980), Principles of Mineral Behaviour. Blackwells, Oxford.

Scott S.D. (1975), Hydrothermal synthesis of refractory sulfide minerals. Fortschr Mineralogie, 52, 185-195.

Scott, S.D. and Barnes H.L. (1971), Sphalerite geothermometry and geobarometry. Economic Geology, 66, 653-669.

Scott, S.D. and Kissin, S.A. (1973), Sphalerite composition in the Zn-Fe-S system below 300^{o}C. Economic Geology, 68, 475-479.

Sparks, J.T., and Komoto, T. (1963), Neutron Diffraction Study of NiS. Journal of Applied Physics, 34, 1191-1192.

Sparks, J.T., Komoto, T. (1967) Metal-to-semiconductor transition at the magnetic ordering temperature of NiS. Physical Letters A, 25, 398-399.

Sparks, J.T., Komoto, T. (1968) Metal-semiconductor transition in hexagonal NiS. Review of Modern Physics, 40, 752-754.

Skinner, W.M., Nesbitt, H. W., and Pratt, A. R. (2004), XPS identification of bulk hole defects and itinerant Fe 3d electrons in natural troilite (FeS) Ceochimica et Cosmochimica Acta, 68, 2259-2263.

Sowa, H., Ahsbahs, H., and Schmitz, W. (2004), X-ray diffraction studies of millerite NiS under non-ambient conditions. Physics and Chemistry of Minerals, 31, 321-327.

Stølen, S., Fjellvåg, H., Grønvold F., Seim, H., and Westrum, E.F. (1994), Phase stability and structure properties of $Ni_{7\pm\delta}S_6$ and Ni_9S_8. Heat capacity and thermodynamic

properties of Ni_7S_6 at temperature from 5 to 970 K and of Ni_9S_8 from 5 to 673 K. Journal of Chemical Thermodynamics, 26, 987-1000.

Sugaki, A., Shima, H., Kitakaze, A., and Fukuoka, M. (1977), Studies on pyrrhotite group minerals (3). On solvuses of solid solutions among troilite, hexagonal and monoclinic pyrrhotite below 300^{o}C. Tohoku University Science Report serie.3, 13, 147-163.

Taylor, L.A., (1970), Low-temperature phase relations in the Fe-S system, Carnegie Institute of Washington Year Book, 68, 259-270.

Thomas, J. E., Skinner W. M., and Smart R. St. C. (2003), A comparison of the dissolution behavior of troilite with other iron (II) sulfides; implications of structure, Geochimica et Cosmochimica Acta, 67, 831-843.

Tokonami, M., Nishihiguchi K., and Morimoto N. (1972), Crystal structure of monoclinic pyrrhotite (Fe_7S_8). American Mineralogist, 57, 1066-1080.

Trahan, J., and Goodrich, R.G., and Watkins, S. F. (1970), X-ray diffraction measurements on metallic and semiconducting hexagonal NiS. Physical Review B, 2, 2895-2863.

Vaidya, N. (1976), X-ray diffraction study of Ni S And Cr S at high pressures. Indian Journal for Pure and Applied Physics, 14, 600-601.

Vaughan, D.J., Craig J.R., Mineral Chemistry of Metal Sulphides, Cambridge University Press, Cambridge, 1978.

Vorma, A. (1970), Pyrrhotite-troilite intergrowth from luikonlahti copper deposit, eastern Flinland: Geological Society of Finland Bulletin, 42, 3-12.

Wang, H., Pring, A., Ngothai, Y., and O'Neill, B. (2005), Phase evolution and kinetics of the oxidation of monosulfide solid solution under isothermal conditions. Thermochim. Acta. 427, 1350-1362.

Ward, J.C. (1970), The structure and properties of some iron sulfides. Review of Pure and Applied Chemistry, 20, 175-206.

Yund, R.A. (1962), Phase relations in the system Ni-As, Economic Geology, 56, 1273-1296.

Yund, R.A. and Hall, H.T. (1970), Kinetics and mechanism of pyrite exsolution from pyrrhotite, Journal of Petrology, 11, 381-404.

CHAPTER THREE

Chapter 3: Experimental Methods

3.1 Introduction

The experimental methods used in this work involve sample synthesis, anneal-quench processes, phase characterization, *Rietveld* refinement of the XRD profiles, collection of kinetic data and cell parameters for each phase, and compositional analysis. Kinetic studies have been performed on solid-state reactions in the Fe-Ni-S and the Ni-S systems. The use of synthetic rather than natural samples allows a choice of bulk compositions and minimizes the uncertainty associated with the effects of trace impurities.

3.2 Sample preparation

The standard 'silica-glass-tube' technique was used to synthesize iron-nickel monosulfides $(Fe,Ni)_{1-x}S$ and nickel monosulfides $Ni_{1-x}S$ (Vaugan and Craig, 1978; Kullerud, 1971). The nonstoichiometry of these synthetic phases is associated with the complex nature of their related reactions. Therefore, it is important to ensure the homogeneity of the synthetic samples in order to accurately decipher the kinetic behavior of these solid-state reactions. The 'silica-glass-tube' technique is a dry synthesis process. Pure iron (99.9+%, Aldrich), nickel (99+%, Aldrich) wires, and S (99.99+%, Aldrich) were used. Iron powder is not used in the current study due to its large surface area subjected to larger extent of oxidation by air in ambient. These dry reagents in elemental form were sealed under vacuum in silica glass and placed in muffle furnaces (see Figure 3.1). Figure 3.2 illustrates the vacuum-line system and welding torch used to seal the glass tubes. Silica wool was used to prevent mass loss during evacuation. The charges were heated slowly to 300^{o}C and then taken up to 500 and 800^{o}C, soaking for 12 hours at

each stage. These soaking steps minimized tube failures caused by high S vapour pressure above 450^{o}C (Etschmann et al., 2004).

Figure 3.1. The muffle furnaces used in this work, BC9090 (Kiln, Co. Ltd.). The safe operating temperature range is below 1200^{o}C. The heating schedule is programmable.

The tubes were then quenched in cold water. Charges were removed from their tubes and ground with acetone. Figure 3.3 illustrates the sealed tubes used for quenching tubes and a tube containing a powder charge following grinding under acetone (unsealed). Next, the silica tubes were sealed under vacuum to ensure homogeneity of the charges. The charges were then heated. In this stage, the heating sequence varied depending on the composition of the charges. For example, $(Fe,Ni)_{1-x}S$ (*mss*) may be heated up to 1100^{o}C to form a homogeneous melt, whereas NiS can only be heated to 700^{o}C, as above this

temperature the NiS will unmix, forming $Ni_{1-x}S$ + Ni_3S_2. Different annealing/heating schemes were adopted depending on the reaction studied (details are available in Chapters 4-7).

Figure 3.2. The vacuum system used in the preparation of synthetic samples. The inlet is the welding torch that used to melt and seal glass tubes under vacuum.

3.3 X-ray diffraction and *Rietveld* refinement

Phase analysis (phase fraction and cell parameters) of the anneal-quench samples was undertaken using X-ray diffraction and *Rietveld* refinement. For three sets of experiments the XRD patterns were collected using a 100 mm diameter *Guinier Hägg* camera with Cr $K_{\alpha 1}$ radiation (λ = 2.2897Å), while for another set, room temperature XRD patterns were determined using a Huber HTC 9634 X-ray diffractometer with Co $K_{\alpha 1}$ radiation (λ =

1.78897 Å) (see Figure 3.4). Weight fractions of various phases were calculated by the *Rietveld* refinement (Rietveld, 1967, 1969; Kisi, 1994; Hunter, 1997).

Rietveld refinement can be used to refine both neutron diffraction and X-ray diffraction profiles. The refinement produces 1) the structures of single or mixed phases, 2) the phase transformations and cation disorder, 3) the refined incommensurate and magnetic structure, and 4) the site occupancy, especially in minerals and inorganic materials (Wallwork, 2002). The *Rietveld* refinement uses least-square minimizations to simultaneously refine structure, atomic coordinates, lattice parameters, peak-shapes, thermal displacement parameters, etc. Quantitative phase analysis was performed on each sample using the formalism described by Hill and Howard (1994). The weight fraction of a phase can be described as:

$$w_{\mathrm{p}} = \frac{(SZMV)_p}{\sum (SZMV)_i} \tag{3.1}$$

where w_{p} is the weight fraction of phase P, S is the scale factor, Z is the number of formula units per unit cell, M is the molecular weight of the formula unit, and V is the volume of unit cell. *i* represents each phase.

A *Pseudo-Voigt* function was adopted to model the peak shapes and *Shifted Cheby* I function to model the background. The scale factor (S), cell parameters (*a*, *b*, *c*, α, β, γ), and an overall thermal displacement parameter (B) were fitted during the Rietveld refinement. The refinement of these parameters integrates each intensity into a properly shaped reflection that contributes to the overall diffraction pattern. The result is a calculated X-ray diffraction profile, which best-fits the experimental intensities of the X-ray diffraction peaks. GOF (goodness of fit) was used to assess the success or otherwise of the refinement procedure.

$$\text{GOF} = R_{\text{wp}}/R_{\text{exp}} \tag{3.2a}$$

$$R_{wp} = \left\{ \frac{\sum_i w_i [y_i(obs) - y_i(calc)]^2}{\sum_i w_i [y_i(obs)]^2} \right\}^{1/2} \tag{3.2b}$$

$$R_{\text{exp}} = \left[\frac{N - P}{\sum_i^N w_i y_i(obs)^2} \right]^{1/2} \tag{3.2c}$$

where N is the number of observations, P is the number of parameters, $y_i(obs)$ and $y_i(calc)$ are observed and calculated diffraction intensities respectively. w_i is the weighted phase fraction.

A commercial software package, RIETICA, was used to perform all *Rietveld* refinement. An example of refinement parameter settings is presented in Figure 3.5. The calculated pattern (red curves) best-fits the observed pattern (marked with black '+'). The green cure down the bottom is the deviation between observed and calculated diffraction intensities (see equation 3.2).

3.4 Composition Analyses and Surface Morphology

Scanning electron microscope (SEM) was used for surface structure studies. Energy dispersive X-ray analysis (EDX) and electron microprobe analysis were used for composition analyses. Polished samples were examined using a PHILIPS XL20 scanning electron microscope to reveal surface feature evolution during reactions. Chemical analysis was carried out using a Cameca CAMEBAX SX51 electron microprobe at Adelaide Microscopy, University of Adelaide. The electron microprobe was operated under an accelerating potential of 20 kV and a specimen current of ~20 nA. The spot size

was set at 1 μm but the effective resolution of the beam, due to beam spread in the sample, was of the order of 3 μm. A natural pentlandite was used as a standard for wavelength dispersive analysis.

Figure 3.3. Sealed glass tubes (bottom two) filled in with charges and covered with silica wool at both ends. Open tube filled in with finely ground powder charge (top).

Figure 3.4. Huber HTC 9634 X-ray diffractometer used in this work, with Co $K_{\alpha 1}$ radiation (λ = 1.78897 Å).

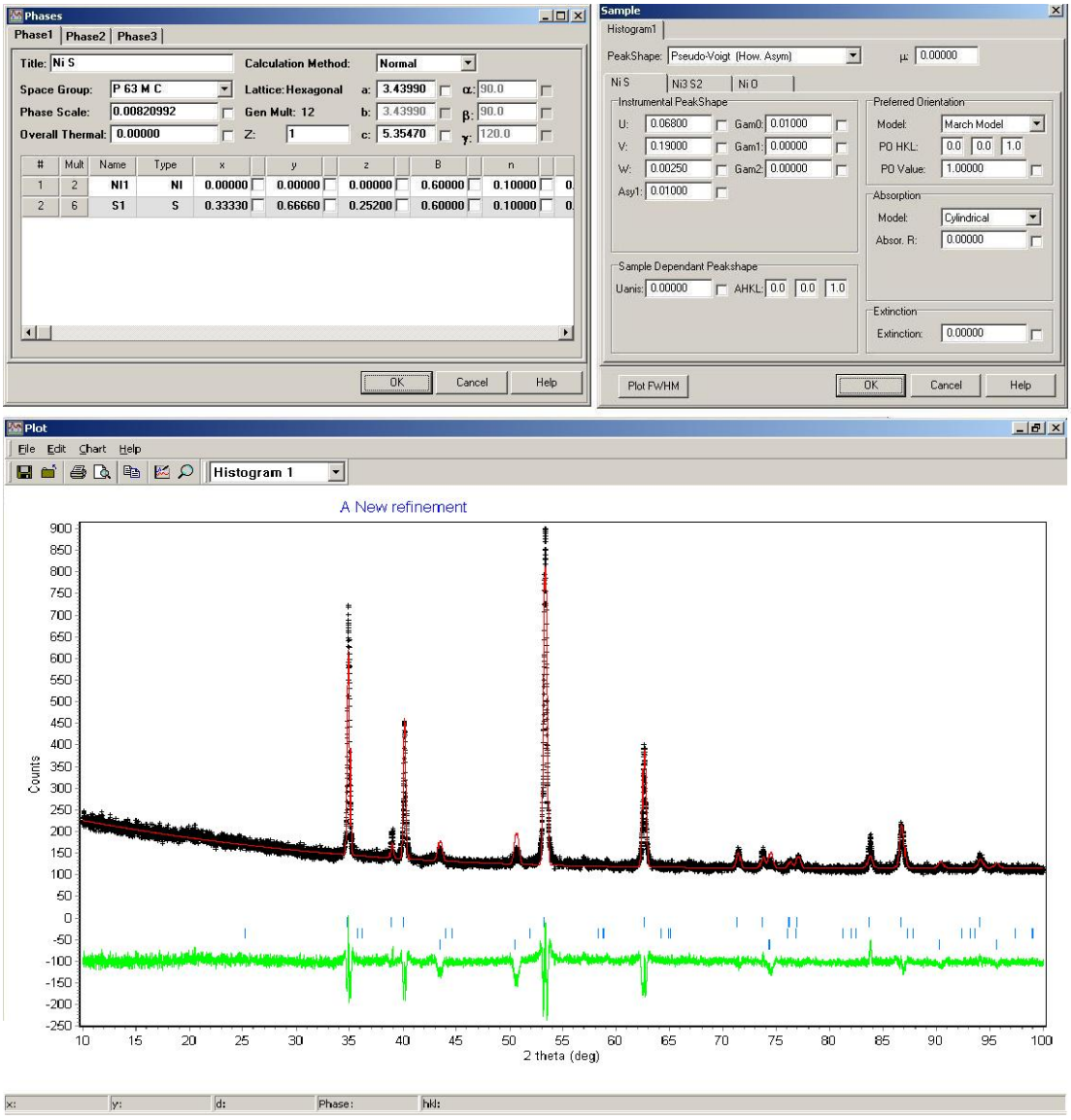

Figure 3.5. An example of *Rietveld* refinement using RIETICA. Three phases are observed in the XRD pattern, α-NiS, NiO, and Ni_3S_2 (short blue vertical lines above the green deviation curve (below) show the positions of diffraction peaks for each phase). The red curve is the calculated pattern, and the black dots ('+') are the observed diffraction intensities.

3.5 References

Etschmann B., Pring A., Putnis A., Grguric B.A., and Studer A., (2004), A kinetic study of the exsolution of pentlandite $(Ni,Fe)_9S_8$ from the monosulfide solid solution (Fe,Ni)S, American Mineralogist, 89, 39-50.

Hill, R.J., and Howard C.J. (1994), Peak shape variation in fixed-wavelength neutron powder diffraction and its effect on structural parameters obtained by Rietveld analysis. Journal of Applied Crystallography, 18, 173-180.

Hunter, B.A.(1997), Rietica 1.7.7. ANSTO, Sydney, Australia.

Kisi, E.H. (1994), Rietveld analysis of powder diffraction patterns. Material Forum, 18, 135-153.

Kullerud, G. (1971), Experimental techniques in dry sulfide research. In G.C. Ulmer, ed., Research Techniques for High Pressure and High Temperature, p. 288-315, Springer-Verlag, Berlin.

Rietveld, H.M. (1967), Line profiles of neutron powder-diffraction peaks for structure refinement. Acta Crystallographica, 22, 151-152.

Rietveld, H.M. (1969), A profile refinement method for nuclear and magnetic structures. Journal of Applied Crystallography, 2, 65-71.

Vaugan, D.J. and Craig, J.R. (1974), The crystal chemistry and magnetic properties of iron in the monosulfide solid solution of the Fe-Ni-S system. American Mineralogist, 59, 926-933.

Wallwork, K.S. (2002), *Ab initio* structure determination of minerals and inorganic materials by powder diffraction methods, Ph.D thesis, Flinders University of South Australia, Australia.

CHAPTER FOUR

Geochimica et Cosmochimica Acta, Vol. 69, No. 2, pp. 415–425, 2005

0016-7037/05 $30.00 + .00

doi:10.1016/j.gca.2004.06.031

A low-temperature kinetic study of the exsolution of pentlandite from the monosulfide solid solution using a refined Avrami method

HAIPENG WANG,[1] ALLAN PRING,[2,3,*] YUNG NGOTHAI,[1] and BRIAN O'NEILL[1]

[1]School of Chemical Engineering, University of Adelaide, Adelaide, SA 5005, Australia
[2]Department of Mineralogy, South Australian Museum, Adelaide, SA 5001, Australia
[3]School of Earth & Environmental Science, University of Adelaide, Adelaide, SA 5005, Australia

(*Received December* 1, 2003; *accepted in revised form June* 25, 2004)

Abstract—A refined Avrami method, that assumes that the activation energy is a function of reaction extent y, was used to analyze the kinetics of the exsolution of pentlandite from *mss*/pyrrhotite (bulk composition, $(Fe_{0.77}Ni_{0.19})S$) over the temperature range 473 to 573 K. The experimental results show the reaction rates vary from 1.6×10^{-5} to 5.0×10^{-7} s^{-1} at 473 K and from 9.4×10^{-5} to 4.1×10^{-7} s^{-1} at 573 K. Examination of exsolution textures indicated that the mechanism of exsolution did not change significantly over the temperature range investigated. The activation energy (E_a) decreases from 49.6 to 20.7 kJ mol^{-1} over the course of the reaction. The decrease in E_a with y is related to the change in the dominant factor of pentlandite exsolution, from nucleation dominant at the beginning to metal ion diffusion dominant at the end. The classic Avrami method provides average values of kinetic parameters for the overall solid-state reaction while the refined Avrami method provides more a detailed indication of the variation of kinetic parameters over the course of the reaction. Previously published kinetic data for the exsolution of pentlandite from *mss*/pyrrhotite are reevaluated using the refined Avrami method.

1. INTRODUCTION

The kinetic behavior of many mineral reactions has been successfully modelled using the Avrami /Arrhenius model, where the activation energy, E_a, is assumed constant during the course of reaction (Wiersma and Rimstidt, 1984; Putnis, 1992). Preliminary analysis of data for the exsolution of pentlandite and pyrrhotite from the monosulfide solid solution (*mss*) indicated that some modification to this classical treatment was necessary for the reactions in the Fe-Ni-S system (Wang et al., 2003; Etschmann et al., 2004). In this system, activation energies are comparatively small and changes in local crystal chemistry are significant. Vyazovkin (2001) noted that the notion that E_a varies with reaction extent, y, can be widely applied and the assumption of a constant E_a is only valid for a small segment of reaction extent (Δy). The Advanced Isoconversional Method (Vyazovkin, 1997; Vyazovkin, 2001) can be used to evaluate the dependence of E_a on reaction extent, y, using integration techniques.

Empirically it is found that the isothermal kinetics of a wide range of mineral reactions can be described by an equation of the general form

$$y = 1 - \exp\,[-(kt)^n] \tag{1}$$

where k is a rate constant, t is the reaction time, y is the reaction extent and n is a time exponent that depends on the reaction mechanism (Burke, 1965; Christian, 1965; Putnis, 1992).

Solid-state reaction kinetics is based on the activated state theory, where the reaction rate can be written as

$$\frac{dy}{dt} = k \cdot f(y) \tag{2}$$

As k, the rate constant in Eqn. 1 is defined in terms of both y and t, it is not a true rate constant in the same sense as it is in Eqn. 2, where k has the unit of s^{-1}.

It is well known that rate constants are exponentially dependent on the inverse of absolute temperature. The dependence of k on temperature has the general form of the Arrhenius equation:

$$k = A \exp\left(-\frac{E_a}{RT}\right) \tag{3}$$

where A is the preexponential constant. The disadvantage of this method is that the value of k depends on the empiric selection of the function $f(y)$ in Eqn. 2 and therefore E_a depends on the choice of rate equation. A number of different forms of rate equation may fit the data equally well, but result in different values of E_a (Vyazovkin and Wright, 1997). A second disadvantage is that it assumes E_a does not change over the course of an isothermal transformation. However, the activation energy needed to stimulate a reactant to an activated state is dependent on local structural features. The local structural environment of reactant atoms usually changes over the course of a reaction. Thus, it is reasonable to believe E_a is a function of y.

An alternative approach is to use the isoconversional methods of Friedman (1964), Ozawa (1965) and Vyazovkin and Lesnikovich (1990) where E_a is evaluated universally. Ozawa (1965) employed the integral approximation of Doyle (1961) to derive the equation:

$$\log \beta = \text{constant} - 0.4567\, E_a/RT_Y \quad (\text{when } E_a/RT_Y > 20) \tag{4}$$

where β is the heating rate; T_Y, the temperature reached when

* Author to whom correspondence should be addressed, at South Australian Museum, Department of Mineralogy, North Terrace, SA 5001, Australia. (Pring.Allan@saugov.sa.gov.au).

reaction extent is $y = Y$. Given the constancy of E_a, the plot of log β vs. the reciprocal absolute temperature at a given reaction extent, $y = Y$, must give a straight line. This is known as the Ozawa isoconversional method and the slope determines the activation energy. The dependence of activation energy on reaction extent, which is caused by the changing physical and mechanical properties of the reaction medium, was further developed by Vyazovkin (2000a).

In the current study on the exsolution of pentlandite from *mss*/pyrrhotite, the *mss*/pyrrhotite is the reaction media and it becomes progressively metal deficient with increasing reaction extent. Most solid-state reactions are multiple-step reactions. The activation energy dependence on reaction extent reflects the variation in relative contributions of each step to the overall reaction rate (Vyazovkin, 2000b). The main purpose of this study is to find a more appropriate formalization to describe the kinetic behavior of pentlandite exsolution from *mss*/pyrrhotite. This method incorporates the notion of E_a dependence on y (Vyazovkin and Dollimore, 1996; Vyazovkin and Wright, 1997; Vyazovkin, 2003). In this paper a refined Avrami model is derived and fitted to the isothermal data.

Pyrrhotite $(Fe,Ni)_{1-x}S$ and pentlandite $(Fe, Ni)_9S_8$ are important constituents of primary nickel sulfide ore deposits. Pentlandite is invariably associated with pyrrhotite. At high temperatures (above 883 K) $(Fe,Ni)_{1-x}S$ has the NiAs structure and is known as the monosulfide solid solution (*mss*). Above 883 K there is complete solid solution between Fe and Ni end members, but below this temperature *mss* breaks down via exsolution of pentlandite with the residual *mss* undergoing metal-vacancy ordering to form pyrrhotite (Naldrett et al., 1967; Misra and Fleet, 1973a; Francis et al., 1976; Vaughan and Craig, 1978; Durazzo and Taylor, 1982). During exsolution the Ni is concentrated into pentlandite, and in nature the host *mss*/pyrrhotite usually contains less than 1 atomic % Ni. In experimental studies, coexisting pyrrhotites can contain up to 25 atomic % Ni replacing Fe, the extent of this substitution depends both on the bulk composition and temperature (Craig, 1973; Misra and Fleet, 1973a,b; Vaughan and Craig, 1978; Etschmann et al., 2004). Experiments have shown that at 503 K the maximum Ni content of *mss* diminishes to 17 atomic % Ni. This value is still much greater than the range of Ni contents for pyrrhotites that coexist with pentlandite in magmatic sulfide deposits, and indicates that chemical readjustments in these sulfides occur at very low temperatures (Naldrett et al., 1967; Craig, 1973; Misra and Fleet, 1973a; Farrell and Fleet, 2002; Etschmann et al., 2004).

The composition and stoichiometry of the exsolved pentlandite is variable, and in nature, atomic Fe: Ni ratios vary from 1:3 to 3:1 but most natural compositions are close to 1:1 (Riley, 1977). The pure Ni and Fe pentlandite end members are not stable and Ni-rich pentlandites have been reported to show some cation deficiency $(Ni,Fe)_{9-x}S_8$ while Fe-rich pentlandites are said to be cation excess $(Fe,Ni)_{9+x}S_8$ (Rajamani and Prewitt, 1973; Vaughan and Craig, 1974, 1978). The nature of this exsolution process has been studied by a number of workers (Francis et al., 1976; Durazzo and Taylor, 1982; Kelly and Vaughan, 1983; Wang et al., 2003; Etschmann et al., 2004). Durazzo and Taylor (1982) and Kelly and Vaughan (1983) performed systematic studies investigating the exsolution textures produced in synthetic materials. They found that the texture was dependent on the annealing time, the temperature, and S fugacity. Early-formed textures depend on the initial degree of supersaturation and solid-state diffusion; the final textures result from further growth and coarsening of early forms and are particularly sensitive to metal diffusion, which is a function of temperature. Kelly and Vaughan (1983) also reported some preliminary kinetic studies on the pentlandite-pyrrhotite system.

Yund and Hall (1970) studied the kinetics of exsolution of pyrite from pyrrhotite. They measured changes in *mss*/pyrrhotite composition by X-ray diffraction and thus were able to estimate extent of pyrite exsolution. The stoichiometry of pure Fe *mss*/pyrrhotite can readily be determined from the cell parameters and the value of the d_{102} spacing of the NiAs subcell (Arnold, 1962; Toulmin and Barton, 1964; Fleet, 1968; Yund and Hall, 1970). Misra and Fleet (1973b) reported similar results for the effects of Ni/Fe substitution on the d_{102} spacing in *mss*/pyrrhotite, but the changes are an order of magnitude greater than those of the M: S (metal to sulfur) ratio. During the exsolution of pentlandite from *mss*/pyrrhotite, not only does the stoichiometry of *mss*/pyrrhotite change but also the Ni/Fe ratio, so Yund and Hall's (1970) method of measuring the extent of reaction from changes in the mss/pyrrhotite cannot be readily used in this case.

Etschmann et al. (2004) undertook detailed studies on the kinetics of exsolution using powder neutron diffraction phase analysis on anneal/quench samples and in situ cooling experiments. The compositions they investigated were restricted to M: S ratio of 1:1 and the kinetics was found to be very rapid. They concluded that these rapid reactions were driven by very rapid nucleation triggered by formation of S vacancies in the *mss* lattice. Heating *mss* with M: S ratio of 1:1 to 573 K produces S vacancies, which provide metal-enriched sites for the nucleation of pentlandite (Etschmann et al., 2004). Only in anneal/quench experiments at low temperatures, $\leq$ 473 K, was the exsolution process slow enough to allow the data to be fitted to a kinetic model and they used the classic Avrami model (Avrami, 1939; Avrami, 1940, 1941; Christian, 1965; Putnis, 1992). Unfortunately, the low temperature data of Estchmann (2004) were very limited and the uncertainties in the phase portions were relatively large. These errors were amplified during model fitting and resulted in large uncertainties in the calculated activation energy.

In this study, we have used similar methods of powder diffraction phase analysis to investigate a more *S*-rich composition $(Fe_{0.77}Ni_{0.19})S$, where metal to sulfur ratio is 49:51. In these experiments, exsolution is somewhat less rapid.

2. EXPERIMENTAL

2.1. Synthesis

The standard silica-tube techniques (Kullerud, 1971; Vaughan and Craig, 1978) were adopted to synthesize the monosulfide solid solution (*mss*). Accurately weighed stoichiometric amounts of Fe (1 mm diameter wire, 99.9+%, Aldrich), Ni (1 mm diameter wire 99.9+%, Aldrich) and S (granules 99.99+%, Aldrich) were sealed under vacuum in 10 mm diameter silica tubes. Bulk compositions of *mss* were selected to give a Ni: Fe of 20:80 and a metal to sulfur ratio M: S = 49:51. The charges were heated slowly to 573 K, then up to 773 and 1073 K, soaking for 12 h at each stage (Etschmann et al., 2004). The slow heating schedule and soaking process were employed to minimize tube failure due to high sulfur vapour pressure above 723 K. The tubes were

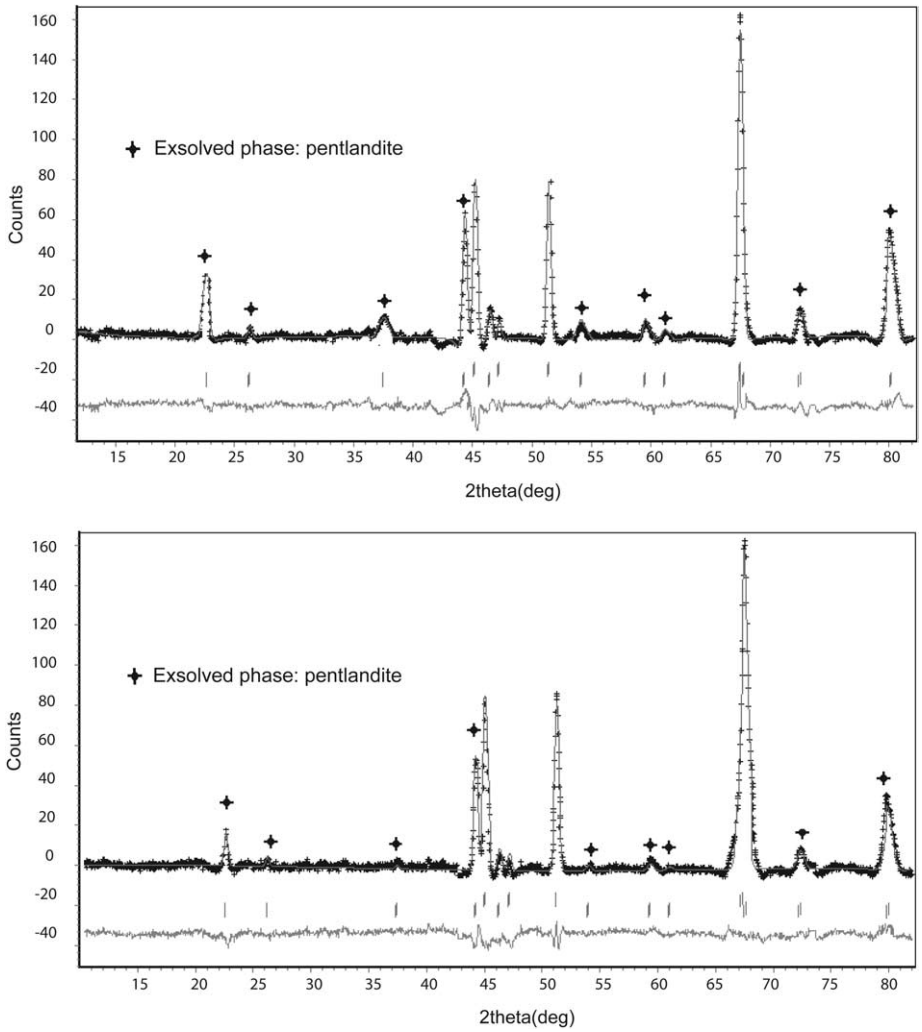

Fig. 1. X-ray diffraction profiles for $(Fe_{0.77}Ni_{0.19})S$ annealed at 473 K (top) and 573 K (bottom) for 500 h. Rietveld refinement of the phase portions gave pentlandite fractions of 33 wt% and 27wt% for 473 and 573 K respectively. Solid curves are the calculated pattern; the experimental data points are +. The difference between the experimental and calculated profiles is shown below. The goodness of fit (GOF) for the two profiles are 0.305 (473 K) and 0.147 (573 K).

quenched to room temperature in cold water. The charges were removed from the tubes and ground to fine powder under acetone ensuring the homogeneity of the *mss*. The samples were then resealed in new silica tubes and heated at 1373 K for 2 h, cooled to 1173 K, annealed for 7 d and then quenched in a large volume of cold water. This resulted in homogenous samples with a relatively uniform grain size of ~0.5 mm. A series of anneal/quench experiments were performed on the *mss* at temperature range from 473 to 573 K with annealing periods up to 500 h. Temperature in the muffle furnaces was controlled within error range ±5 K.

2.2. X-ray Diffraction

Room temperature X-ray powder diffraction patterns of the quenched products were obtained using a 100 mm diameter Guinier Hägg camera with Cr $K_{\alpha 1}$ radiation (λ = 2.2897Å). The finely powdered sample was mixed with a small amount pure Si which was used as an internal standard. The Guinier Hägg films were scanned in TPU/Pos mode using an Epson film scanner and the powder diffraction profiles over 2θ range 10 to 90° were extracted using the programs Scion Image and Universal-Si-Calibration, a macro function based on Igor Pro 4.0 (WaveMetrics Inc.). Weight fraction of exsolved pentlandite was determined by Rietveld refinement (Hunter, 1997). Since all the atoms in the pentlandite structure and *mss*/pyrrhotite subcell occupy special position and Fe and Ni are not readily distinguishable by X-ray diffraction, only profile parameters, cell parameters, overall temperature factor and phase scale factors were refined. The proportions of pentlandite and *mss*/pyrrhotite determined by Rietveld analyses of the X-ray powder diffraction data were compared with the phase analyses obtained on some of the same samples by powder neutron diffraction (Wang et al., 2003) and found to be within one standard deviation. Figure 1 shows the X-ray diffraction patterns for the samples annealed for 500 h at 473 K and 573 K. Note that the pentlandite reflections are more prominent at 473 K than at 573 K.

2.3. Chemical Analyses

Chemical analysis was carried out using a Cameca CAMEBAX SX51 electron microprobe at Adelaide Microscopy, University of Adelaide. The analyses were undertaken using an accelerating potential of 20 kV and a specimen current of ~20 nA. The spot size was set at 1 μm but the effective resolution of the beam, due to beam spread in the sample, was of the order of 3 μm. A natural pentlandite was used as a standard for wavelength dispersive analysis.

Table 1. Exsolution of pentlandite from *mss* $(Fe_{0.77}Ni_{0.19})S$. Summary of results from anneal quench specimens. Pentlandite in weight percentage; a_{penn} a_{pyrr} *and* c_{pyrr} are cell parameters of pentlandite and pyrrhotite. Estimated standard deviations are given in brackets.

Temp (K)	Time (hr)	*wt*% pent.	a_{pent}/Å	a_{pyrr}/Å	c_{pyrr}/Å
473	0.5	0(1)	10.057(3)	3.4461(8)	5.737(3)
	0.75	0(1)	10.059(3)	3.4476(8)	5.736(3)
	1	2(2)	10.060(3)	3.4480(8)	5.733(3)
	2	4(1)	10.064(3)	3.4520(8)	5.730(3)
	5	10(2)	10.058(4)	3.4511(8)	5.722(2)
	26	27(2)	10.063(2)	3.4522(4)	5.725(4)
	46	32(1)	10.070(2)	3.4523(4)	5.720(3)
	64	33(1)	10.067(2)	3.4525(6)	5.719(2)
	100	33(1)	10.070(2)	3.4518(6)	5.721(2)
	500	33(1)	10.068(3)	3.4522(8)	5.720(4)
498	0.5	5(2)	10.062(3)	3.4466(8)	5.725(2)
	1	10(2)	10.060(2)	3.4452(8)	5.726(1)
	8.5	14(3)	10.061(2)	3.4565(8)	5.722(2)
	12	18(2)	10.058(4)	3.4451(8)	5.722(2)
	17	21(2)	10.065(3)	3.5012(8)	5.721(2)
	22.5	25(2)	10.063(2)	3.5112(8)	5.719(2)
	26	25(2)	10.072(1)	3.4449(8)	5.718(2)
	30	27(2)	10.060(3)	3.4450(8)	5.717(3)
	46	30(2)	10.068(4)	3.4453(6)	5.716(2)
	64	29(1)	10.077(2)	3.4455(6)	5.715(2)
	84	31(1)	10.059(2)	3.4457(6)	5.713(1)
	100	31(1)	10.069(2)	3.4448(6)	5.713(1)
523	0.5	6(2)	10.077(1)	3.4464(4)	5.725(3)
	1	17(2)	10.072(4)	3.4501(4)	5.723(1)
	5	21(2)	10.065(2)	3.4502(7)	5.722(2)
	8.5	20(2)	10.072(3)	3.4504(6)	5.722(2)
	12	20(2)	10.069(1)	3.4510(5)	5.721(2)
	17	22(2)	10.067(3)	3.4521(4)	5.719(3)
	22.5	26(2)	10.070(2)	3.4531(5)	5.718(2)
	26	26(2)	10.055(2)	3.4509(7)	5.717(4)
	30	27(2)	10.067(2)	3.4509(6)	5.715(2)
	46	29(1)	10.064(2)	3.4488(6)	5.713(2)
	64	31(2)	10.068(2)	3.4547(8)	5.711(2)
	84	30(1)	10.071(2)	3.4498(3)	5.707(2)
	100	29(1)	10.073(2)	3.4765(6)	5.710(2)
548	0.5	5(2)	10.058(2)	3.4465(4)	5.718(4)
	1	20(2)	10.065(2)	3.4532(2)	5.714(2)
	8.5	22(2)	10.074(4)	3.4501(2)	5.713(2)
	12	24(2)	10.072(3)	3.4520(4)	5.713(2)
	17	26(1)	10.075(2)	3.4502(2)	5.711(2)
	22.5	27(1)	10.073(2)	3.4505(2)	5.711(2)
	26	28(1)	10.074(2)	3.4499(2)	5.710(2)
	30	26(2)	10.077(3)	3.4497(3)	5.708(2)
	46	27(2)	10.068(1)	3.4469(2)	5.707(2)
	64	28(1)	10.071(1)	3.4465(2)	5.708(1)
	100	28(1)	10.071(1)	3.4471(2)	5.708(2)
573	0.5	6(2)	10.061(2)	3.4496(4)	5.719(4)
	1	20(2)	10.063(2)	3.4488(2)	5.717(2)
	2	25(2)	10.068(3)	3.4493(3)	5.717(2)
	5	26(2)	10.071(1)	3.4502(2)	5.716(2)
	26	27(2)	10.073(2)	3.4495(2)	5.712(3)
	46	27(1)	10.074(2)	3.4477(2)	5.708(2)
	64	26(1)	10.073(2)	3.4502(4)	5.708(2)
	100	27(1)	10.065(2)	3.4501(2)	5.707(1)
	500	27(2)	10.070(2)	3.4501(4)	5.707(3)

3. RESULTS AND DISCUSSION

3.1. The Kinetic Model

The cell and phase data for the 5 sets of isothermal annealing experiments are summarized in Table 1. Note that the cell parameters for pentlandite did not change significantly over the course of the reaction indicating that its composition remains more or less constant on the time scale of these experiments. The *c* parameter of pyrrhotite, $c_{pyrr,}$ decreases over the exsolution, as *mss*/pyrrhotite becomes more Fe and vacancy rich. Electron microprobe analysis for the sample annealed at 573 K for 100 h gave the compositions $(Fe_{4.53}Ni_{4.45})S_8$ (S 32.67, Fe 32.30, Ni 33.31 wt%) and $Fe_{0.84}Ni_{0.11}S$ (S 36.84, Fe 53.75, Ni 7.65 wt%) for pentlandite and *mss*/pyrrhotite respectively. This

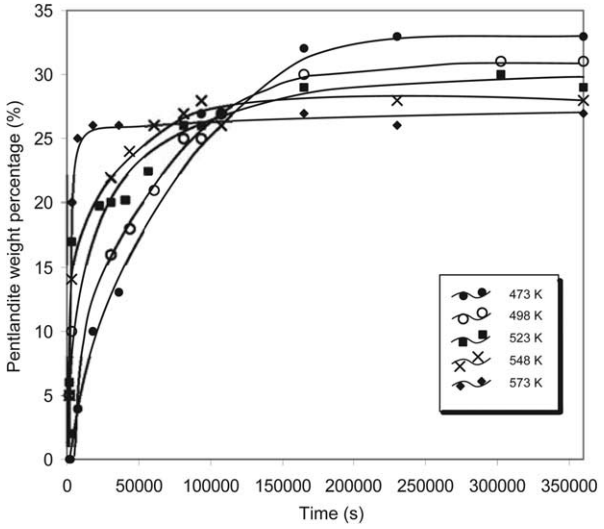

Fig. 2. Graph showing the extent of pentlandite exsolution from *mss*/pyrrhotite (in weight percent) for the five annealing temperatures used: 473 K (●), 498 K (○) 523 K (■), 548 K (×), 573 K (♦). The data were derived by Rietveld refinement of the powder X-ray diffraction profiles. The lines of best fit were calculated by least-square refinement (exponential function in divided sections) using Igor Pro 4.0.

sample had relatively coarse pentlandite lamella and this enabled accurate pentlandite analysis. The electron microprobe analyses also showed that the *mss*/pyrrhotite in this sample was homogeneous; there was no evidence of Fe-Ni compositional gradients between pentlandite lamella. Since the cell parameters of pentlandite do not vary significantly between the five data sets, it can be taken that the pentlandite compositions are the same for all 5 annealing temperatures. The *mss*/pyrrhotite compositions will vary as the final amount of exsolved pentlandite changes with annealing temperature.

Figure 2 shows the amount of pentlandite exsolution plotted against time for 5 temperatures between 473 and 573 K. The exsolution rate in this system is relatively rapid. At the highest temperature, (573 K) the exsolution reaction reaches equilibrium within 5 h (18,000 s), after that period the pentlandite weight fraction remained at around 27%, with little increase even after prolonged annealing. At 473 K the reaction is less rapid and the pentlandite fraction increases continuously to 33 wt% over 24 h.

It is reasonable to believe the same mechanism for exsolution applies over the temperature range, 473 to 573 K, as the samples show very similar textures (Fig. 3).

The weight fraction of pentlandite in Table 1 is converted to reaction extent, *y,* using the equation

$$y = \frac{w_t - w_0}{w_e - w_0} \times 100\% = \frac{w_t}{w_e} \times 100\% (w_0 = 0) \qquad (5)$$

where w_O, w_e, w_t are the weight fractions of pentlandite exsolved at: the beginning of reaction ($t = 0$), at the end of reaction ($t = \infty$) and at an arbitrary time, t, respectively (Yund and Hall, 1970).

A crucial point in kinetic analysis of the data are the definition of w_e. In isothermal exsolutions, the compositions of the host phase *mss*/pyrrhotite will vary with temperature, compositional fields being more extensive with higher temperatures and thus less exsolution will occur. Due to the lack of thermodynamic data for pentlandite-pyrrhotite reactions across the *mss* compositional field, the end of reaction w_e, cannot be determined by *Gibbs* free energy calculations. It is possible to determine w_e by assuming a constant composition of pentlandite and a fixed final composition for *mss*/pyrrhotite, which are independent of temperature and then calculate the mole fractions by mass balance. This approach was employed by Etschmann et al. (2004), who calculated w_e to be 38.78 wt% pentlandite for a pentlandite composition of $(Fe_{4.5},Ni_{4.5})S_8$ and a Ni-free *mss*/pyrrhotite. This mode of a fixed extent of reaction independent of temperature is unrealistic, as at higher temperatures the reactions will never reach completion and this can result in apparently negative activation energies.

The alternative is to define equilibrium for the process empirically from the experiments and make no assumptions about the compositions of the pentlandite and *mss*/pyrrhotite.

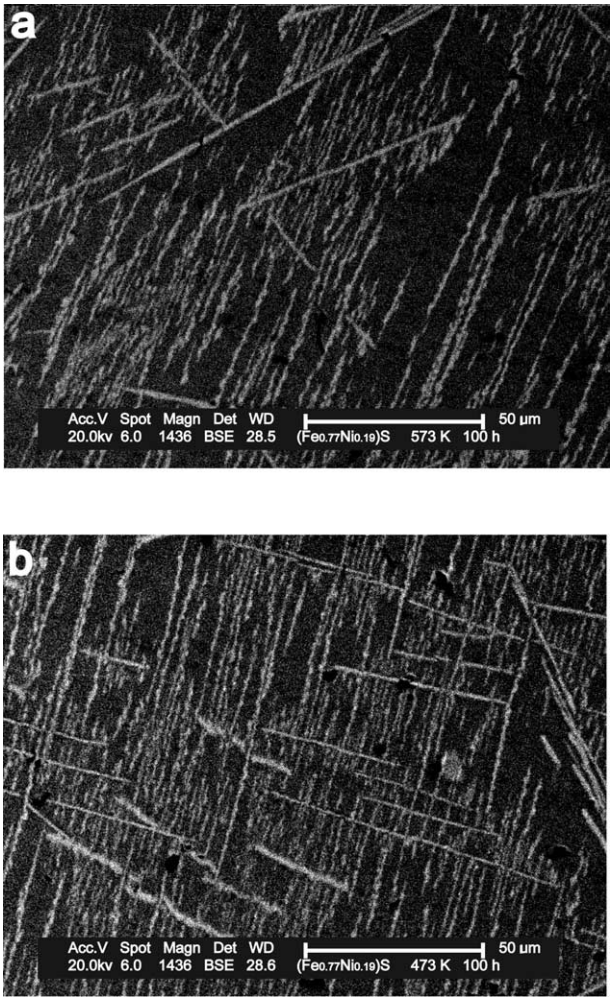

Fig. 3. Back Scattered Electron (BSE) images showing the pentlandite/pyrrhotite exsolution textures for $(Fe_{0.77}Ni_{0.19})S$ annealed at (a) 573 K and (b) 473 K for 100 h. Pentlandite lamella (light) in *mss*/pyrrhotite host (dark). The similarity of the textures at both temperatures indicates that similar exsolution mechanism applies over the temperature range 473 to 573 K.

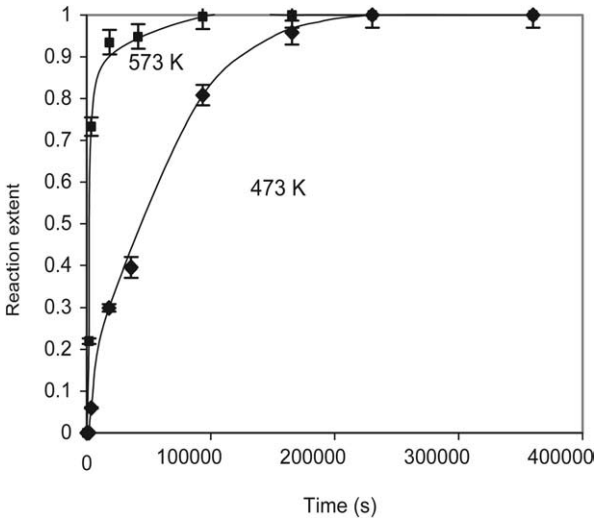

Fig. 4. Plot of reaction extent of pentlandite exsolution (y) against time (t) for annealing experiments at 473 and 573 K. The curves are derived from the data in Table 1 and Figure 2. The pentlandite weight fractions are converted to reaction extent using Eqn. 5. Data measured at 473 and 573 K are represented by symbols ♦ and ■ with error bar.

The classic Avrami model describes the exponential relationship between y (reaction extent) and t (time), but this relation is, theoretically, not valid for infinitively long reaction times (Yund and Hall, 1970). For heterogeneous solid reactions, w_e should be selected at the phase fractions when the portion of pentlandite exsolution has leveled out. The phase fractions from the annealing experiments at 473 and 573 K change very little after 24 h. In these experiments w_e was defined as the average amount of pentlandite exsolved during the three longest annealing periods at each temperature (Table 1). Converting pentlandite weight fraction to reaction extent, y, vs. time, using the above method gives the plots in Figure 4.

3.2. Kinetic Analysis Using the Refined Avrami Method

Many traditional kinetic models assume the overall activation energy of solid-state reaction does not vary during the course of reaction. This assumption ignores the fact that activation energy depends on the structural environment around the atoms, and that this may change significantly during the reaction. Vyazovkin and Lesnikovich (1990) showed that revealing the dependence of the activation energy (E_a) on reaction extent (y), helps not only to understand the complexity of a reaction process, but also identify its kinetics scheme. During the course of exsolution, Ni and Fe atoms diffuse out of the *mss*/pyrrhotite into pentlandite and the *mss*/pyrrhotite becomes progressively more metal deficient and richer in Fe as the reaction proceeds. The local chemical environment of Ni and Fe atoms in *mss*/pyrrhotite changes in the second coordination sphere as the Ni fraction falls from 0.20 to 0.11 during exsolution. More importantly, the concentration of metal vacancies in *mss*/pyrrhotite increases from 3 to 5% of cation sites and thus, E_a for metal diffusion would be expected to decrease. This should lead to a decrease in the overall activation energy as y increases.

On the premise that E_a is a function of reaction extent, y, we can adjust the Arrhenius equation as follows:

$$k(T, y) = A\exp\left[-\frac{E_a(y)}{RT}\right] \tag{6}$$

Assuming the plot against t in Figure 5 conforms to the classic Avrami equation, we can rewrite the Avrami Eqn. 1 as

$$\ln\ln\left(1/(1-y)\right) = n\ln k + n\ln t \tag{7}$$

If Eqn. 7 applies, then a plot of lnln[1/(1 − yr)] vs. ln$t$ should be linear. Clearly, from the plot in Figure 5, it is not, even when experimental uncertainties are considered. Also, the reaction curves in Figure 2 do not comply with the classic Avrami model. The experimental curves show simply decelerating reaction rates during the reactions while the classic Avrami model (Eqn. 1) has a sigmoidal form (n ≠ 1). Reaction curves described by the classic Avrami Eqn. 1 undergo a distinct induction period with a low reaction rate at the beginning, then accelerate to a maximum, and finally approach zero as the reaction reaches completion.

Therefore, we need to consider a modification of the classic Avrami method.

The basic kinetic equation is

$$\frac{dy}{dt} = k(T, y)\cdot f(y) \tag{8}$$

T is temperature; $k(T,y)$, rate constant; $f(y)$, a kinetic model. Rewriting Eqn. 8 and substituting Eqn. 6 for $k(T,y)$ gives,

$$\ln\frac{dy}{dt} = \ln A + \ln f(y) - \frac{E_a(y)}{RT} \tag{9}$$

For a given reaction extent $y = y_0$, ln $f(y)$ and $E_a(y_O)$ are constant. Therefore,

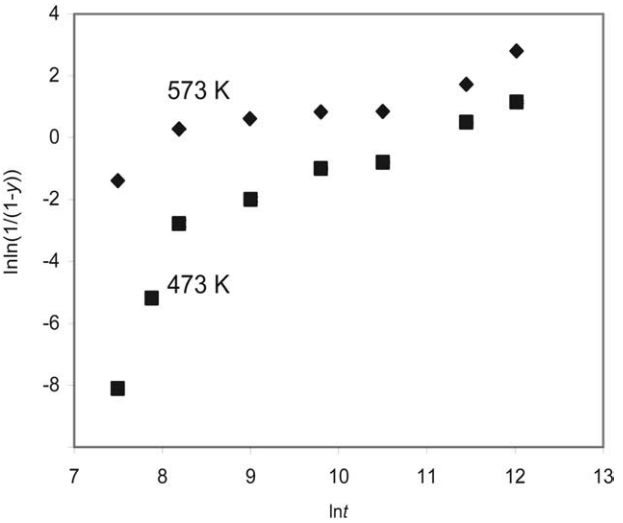

Fig. 5. The plot of lnln[1/(1 − y)] against ln$t$ for the pentlandite exsolution at 473 and 573 K. Reaction extent (y), time (t). It appears that the variation of lnln[1/(1 − y)] with ln$t$ does not follow a linear relation as the classic Avrami method requires.

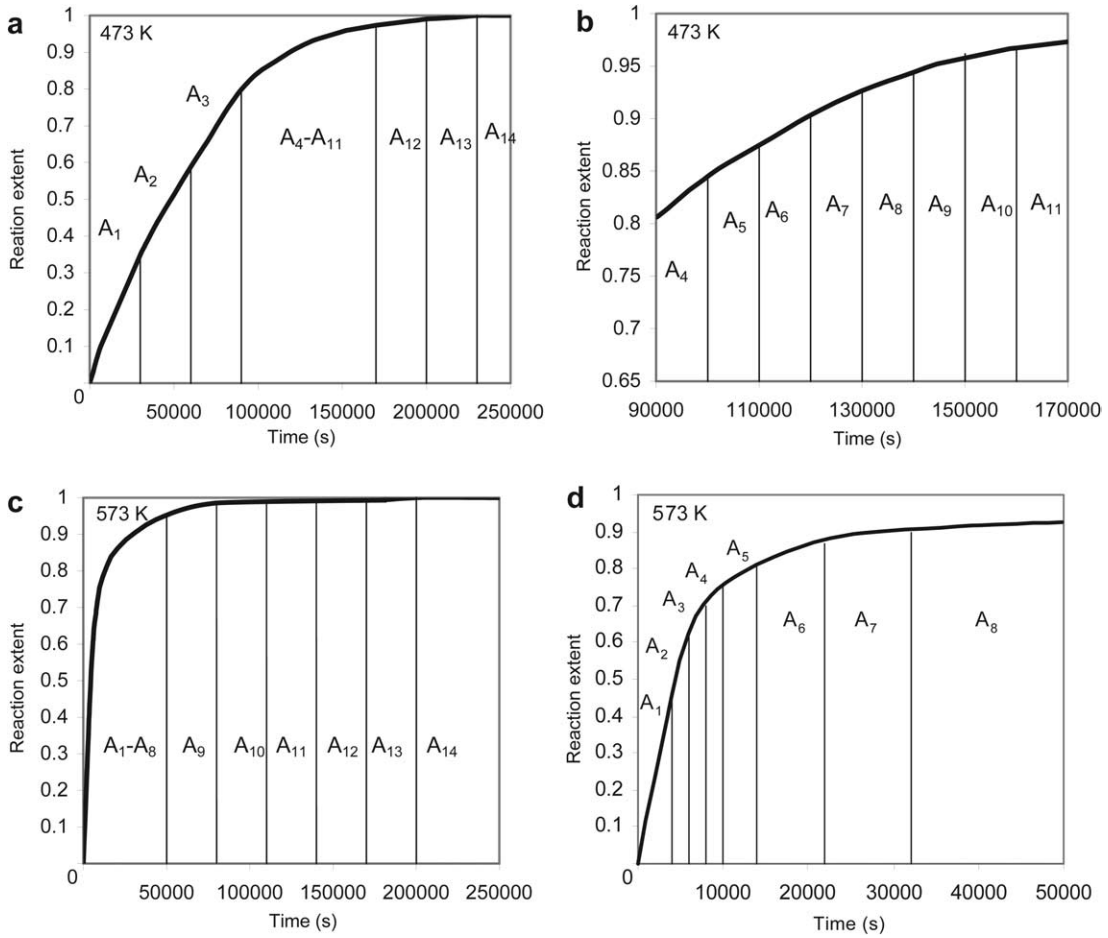

Fig. 6. The curves describing the exsolution of pentlandite at 473 and 573 K (Fig. 4) are subdivided into small regions where the slope is approximately constant. Regions $A_4 \sim A_{11}$ at 473 K and A_1-A_8 at 573 K are finely subdivided due to the relative sharpness of these parts of the curves. (a) exsolution lines at 473 K. (b) enlargement of region A_4-A_{11} in (a). (c) exsolution lines at 573 K. (d) Enlargement of region A_1-A_8 in (c). The curves are derived by least-square method (exponential function in divided sections) using Igor Pro 4.0 to fit exsolution data at 473 and 573 K in Table 1.

$$E_a(y_0) = -R\frac{\ln \dfrac{dy}{dt}(y_0, T_1) - \ln \dfrac{dy}{dt}(y_0, T_2)}{\left(\dfrac{1}{T_1} - \dfrac{1}{T_2}\right)} \qquad (10)$$

where $dy/dt(y_0, T_1)$ and $dy/dt(y_o, T_2)$ are reaction rates to a given value of y_0 at two different temperatures (473 and 573 K respectively). Assuming that the reaction mechanism does not change significantly over the temperature range, the plots in Figure 4 functionally relate the reaction extent y and the annealing time, t, at 473 K and 573 K. The time to a given reaction extent y_0 can therefore be extrapolated from these plots.

Applying Eqn. 10 to calculate activation energy relies on the determination of dy/dt. With careful inspection of the exsolution graph in Figure 4 we find that $\tilde{y}y(t)$ can be divided into a series of regions. This is achieved by dividing the raw data into small time segments, such that the $y = y(t)$ curve can be approximated as a straight line and the slope of each segment is the reaction rate dy/dt. Each region has a nearly constant slope (dy/dt) and this is shown in Figure 6. The calculated reaction rates are plotted against y for the reactions at 473 K and 573 K and are shown in Figure 7. The reaction rates vary from 1.6×10^{-5} to 5.0×10^{-7} s^{-1} at 473 K and 9.4×10^{-5} to 4.1×10^{-7} s^{-1} at 573 K. These reaction rates are slower than those reported by Etschmann et at. (2004) for pentlandite exsolution with M:S of 1:1. The activation energies, determined using Eqn. 10 are summarized in Table 2 and the dependence on y are plotted in Figure 8.

At the beginning of reaction, E_a is around 49.4 kJ.mol^{-1}, but decreases gradually to around 20.7 kJ.mol^{-1} as y approaches 1.

This situation is different from that found by Etschmann et al. (2004) where the bulk composition of their *mss*/pyrrhotite was $(Fe_{0.8}Ni_{0.2})S$, equal amounts of metal and sulfur and thus very few metal vacancies. Heating this material creates S vacancies, and thus local sites of metal enrichment for nucleation of pentlandite, a metal rich mineral. This more metal rich system, $Fe_{0.8}Ni_{0.2}S$ shows a variation of E_a from 2.0 to 21.0 kJ.mol^{-1} (Fig. 9). The low value of E_a (2.0 kJ.mol^{-1}) at the beginning of reaction is consistent with a much lower

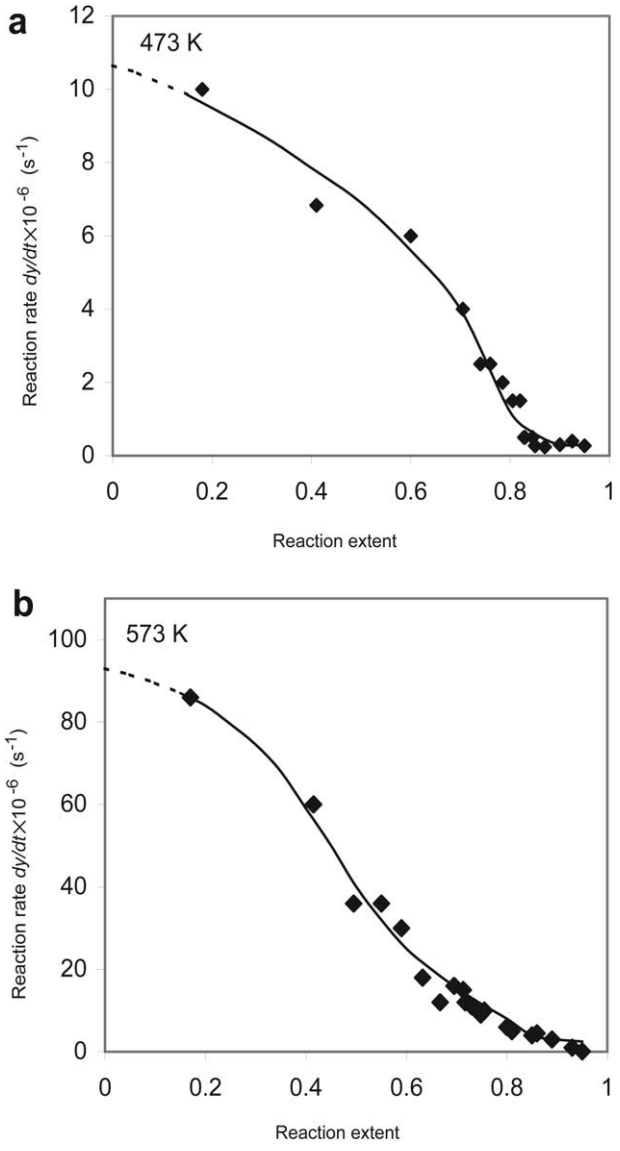

Fig. 7. Plot of reaction rate against reaction extent (y) at 473 and 573 K. Reaction rate (dy/dt) is calculated from the slope of $\bar{y}t$ at each time region $A_1 \sim A_{14}$ in Figure 6. The solid curves are produced by least-square method (Hill function) using Igor Pro 4.0 to fit the calculated dy/dt values in time segments $A_1 \sim A_{14}$.

nucleation energy barrier and consistent with a nucleation model based on S vacancies forming local sites of metal enrichment. The activation energy gradually approaches to an asymptotic value 21.0 kJ.mol^{-1} at the end of reaction. This value is comparable with the value of E_a (20.7 kJ.mol^{-1}) in our current study as the reaction approaches completion. In the metal poor composition investigated here, heating of the sample also will create S vacancies, but these are compensated by the existing metal vacancies and the local areas of metal enrichment that trigger pentlandite nucleation are much more difficult to form.

For $(Fe_{0.77}Ni_{0.19})S$, it appears that E_a is relatively constant at the beginning of exsolution as nucleation of pentlandite is the decisive step. Once $y > 0.5$ it is reasonable to assume that

Table 2. Annealing time and overall activation energy at various fractions of the reaction at T_1 = 473 and T_2, 573 K.

y_o/%	$t(y_o, T_1)$/s	$t(y_o, T_2)$/s	E_a (y_o)/kJ · mol^{-1}
0	0	0	—
0.10	6588	980	48.86
0.15	13482	1471	49.12
0.20	15333	1960	49.32
0.25	19321	2451	49.47
0.30	23130	2941	49.61
0.35	30120	3436	49.35
0.40	35010	3827	48.34
0.45	43221	4101	48.44
0.50	48569	4832	46.48
0.55	56370	5392	44.33
0.60	63124	5882	41.95
0.65	69547	6842	37.74
0.70	78828	8102	32.81
0.75	84466	9580	28.43
0.80	90123	12890	23.67
0.85	100123	19522	21.54
0.90	119985	31000	21.03
0.95	146912	69124	20.66

lamellae coarsening is dominant. As the reaction proceeds, the concentration of metal vacancies in *mss*/pyrrhotite increases and the diffusion path for the metal ions becomes easier. The observation that the reaction rate (dy/dt) slows towards the end of reaction does not conflict with the conclusion of decreasing E_a. The decreasing reaction rate as the reaction approaches equilibrium or at metastable equilibrium is linked to the extended compositional field of *mss* at these annealing temperatures. Both our experiments and those of Etschmann et al. (2004) converge to common residual *mss* compositions and a common value of E_a. The decreasing reaction rate does not appear to be due to increasing path length for Ni and Fe diffusion in mss/pyrrhotite. Under such circumstances, it would be reasonable to expect Ni or Fe composition gradients in

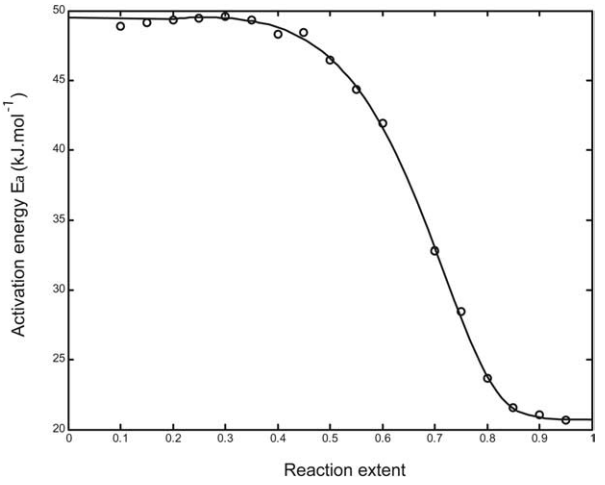

Fig. 8. Graph showing the dependence of E_a (activation energy) on y for the pentlandite exsolution from *mss*/pyrrhotite (initial bulk composition $(Fe_{0.77}Ni_{0.19})S$). The calculated values of activation energy using the refined Avrami method are represented by symbol ○. The solid curves are produced by least-square method (sigmoid function) using Igor Pro 4.0 to fit the calculated value of E_a.

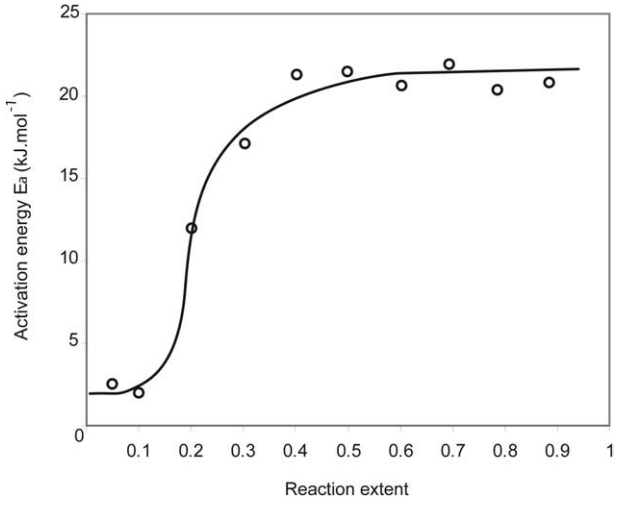

Fig. 9. Graph showing dependence of E_a (activation energy) on y for the pentlandite exsolution from *mss*/pyrrhotite (initial bulk composition $(Fe_{0.8}Ni_{0.2})S$). Raw data are from Etschmann et al. (2004). The calculated values of activation energy using the refined Avrami method are represented by symbol ○. The solid curves are produced by least-square method (sigmoid function) using Igor Pro 4.0 to fit the calculated value of E_a.

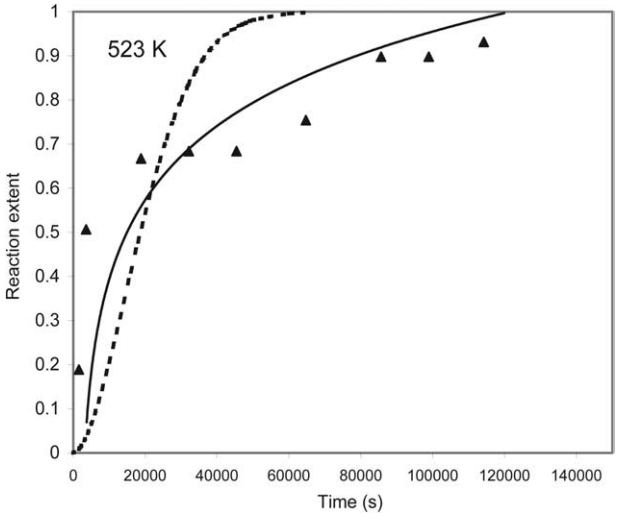

Fig. 10. Predicted kinetic curves for the exsolution of pentlandite from *mss*/pyrrhotite at 523 K. Continuous line is the prediction using the refined Avrami method and the dash line is the prediction using the classic Avrami method, and triangles are experimental data.

mss/pyrrhotite samples annealed for long periods. A series of line scans during electron microprobe analyses failed to find any evidence of such gradients, the composition of *mss*/pyrrhotite was homogenous.

The dependence of E_a on y can be used to predict kinetic behavior at any arbitrary intermediate temperature assuming the reaction mechanism has not changed.

We denote this method, the refined Avrami method, and it employs the concept that E_a changes with reaction extent y. The original Avrami Eqn. 1 can be rewritten as,

$$t(y_0, T) = \exp\left[\frac{E_a(y_0)}{R}\left(\frac{1}{T} - \frac{1}{T_1}\right) + \ln\, t(y_0, T_1)\right] \quad (11)$$

If, $T_1 = 473$ K then

$$t(y_0, T) = \exp\left[\frac{E_a(y_0)}{R}\left(\frac{1}{T} - 0.002113\right) + \ln\, t(y_0, 473\ \text{K})\right] \quad (12)$$

Calculated from Eqn. 12 with data $E_a = E_a(y)$ in Table 2, the predicted variation of y with t at $T = 498$, 523 and 548 K are given in Table 3.

The difference between the kinetic behavior predicted using the classic Avrami method and the refined Avrami method is shown in Figure 10, where the predicted curves of both methods are compared with experimental data obtained at 523 K. Clearly, the refined Avrami method produces a better fit to the

Table 3. Predicted kinetic data for the exsolution of pentlandite fro m *mss* $(Fe_{0.77}Ni_{0.19})S$ at temperatures 498, 523, and 548 K.

y_o/%	$E_a(y_o)$/kJ · mol^{-1}	$t(y_0, 498\ \text{K})$/s	$t(y_o, 523\ \text{K})$/s	$t(y_o, 548\ \text{K})$/s
0	—	0	0	0
0.10	48.86	3532	2010	1204
0.15	49.12	7204	4087	2442
0.20	49.32	8172	4626	2758
0.25	49.47	10278	5808	3457
0.30	49.61	12283	6929	4119
0.35	49.35	16048	9081	5412
0.40	48.34	18895	10817	6516
0.45	48.44	23297	13322	8016
0.50	46.48	26843	15700	9644
0.55	44.33	32021	19199	12062
0.60	41.95	36963	22780	14673
0.65	37.74	42971	27801	18715
0.70	32.81	51867	35521	25181
0.75	28.43	58771	42335	31422
0.80	23.67	66633	50708	39563
0.85	21.54	76066	59327	47332
0.90	21.03	91751	71982	57737
0.95	20.66	112873	88933	71610

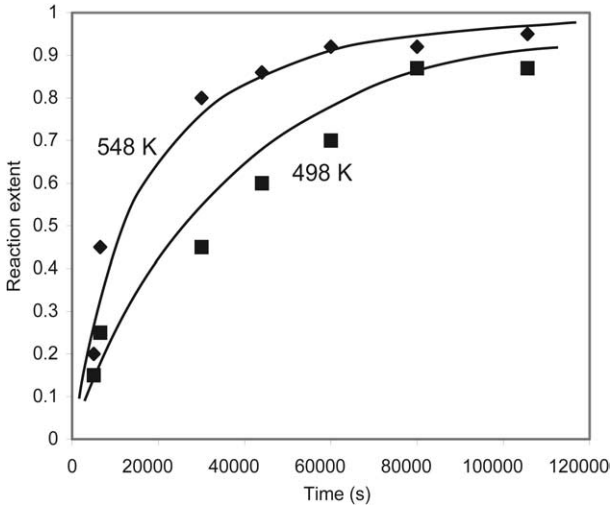

Fig. 11. Plot showing the predicted kinetics exsolution of pentlandite from *mss*/pyrrhotite exsolution at 498 and 548 K using the refined Avrami method together with the experimental values. The solid lines are the theoretical predictions using the refined Avrami method. Squares and diamonds are experimental results at 498 and 548 K, respectively.

isothermal data than the classic Avrami method. Isothermal data were also collected at two other temperatures, 498 and 548 K, and these are illustrated in Figure 11. Again the correspondence between experimental data and prediction is excellent using the refined Avrami method.

Overall, the exsolution process is a multi-step reaction dependent on many other factors in addition to nucleation and metal diffusion. These experiments, however, do illustrate that the widely used assumption of constant activation energy during reaction is very approximate. It is worth emphasizing that most mineral reactions are heterogenous, involving the nucleation and growth of new phases, separated by new surfaces or interfaces. Such reactions involve at least two or often more consecutive steps, each with its own activation energy. In sequential reactions the overall reaction rate is determined by the slowest step and hence an experimentally determined activation energy or rate constant would most probably refer to this 'rate-determining' step (Yund and McCallister, 1970). In the pentlandite-pyrrhotite system, the nucleation and ion diffusion are more than just sequential steps. At the beginning of reaction, pentlandite nucleation is followed by crystal growth (driven by Fe/Ni diffusion) and as the reaction proceeds nucleation becomes less important and crystal growth will dominate. In most cases, the overall activation energy is some intermediate value if more than one step is compatible with the slowest step. Therefore, the contributions of each step to the reaction mechanism are nearly impossible to determine. To gain an understanding of these solid-state reactions it is important to extract the activation energy independent of any reaction model.

Apart from isothermal methods, nonisothermal experiments are also widely used to study reaction kinetics. Vyazovkin (1997) shows how isoconversional methods can be used to predict the kinetic behavior of a reaction outside of the range of experimental temperatures. Model free methods can be adopted to avoid any arbitrary decision in choosing an over simplified model.

3.3. The Effects of S Fugacity on the Kinetics of Exsolution

The experimental results for the exsolution of pentlandite from a *mss*/pyrrhotite, of composition $(Fe_{0.77}Ni_{0.19})S$, show reaction rates vary from 1.6×10^{-5} to 5.0×10^{-7} s^{-1} at 473 K and from 9.4×10^{-5} to 4.1×10^{-7} s^{-1} at 573 K. These rate constants can be compared with those of Etschmann et al. (2004) who found rates of 8×10^{-6} s^{-1} for exsolution from a *mss* of a more metal rich composition $(Fe_{0.8}Ni_{0.2})S$. Etschmann et al. (2004) also recalculated the data from a set of isothermal experiments at 673 K on *mss* compositions $(Fe_{0.89}Ni_{0.11})_{1-x}S$ reported by Kelly and Vaughan (1983). They examined 4 different M:S ratios, with x in the range $0.0 \leq x \leq 0.05$ and the rate constants calculated from their data vary from 3×10^{-5} to 1×10^{-6} s^{-1} between $0.0 \leq x \leq 0.035$, with the slowest rate for the most S rich composition, $x = 0.035$. For $x = 0.05$ no exsolution was observed on the time scale of their annealing runs (1000 h). Our results, taken with those of Etschmann et al. (2004) and Kelly and Vaughan (1983), show that an increase in S fugacity (f_s) decreases the rate of exsolution. Etschmann et al. (2004) concluded that the decrease in rate with increasing f_s is associated with a change in the nucleation mechanism. For *mss*/pyrrhotite with M:S ratios near to 1:1, heating to 573 K creates S vacancies in the *mss* $(Fe,Ni)S_{1-x}$, even in a closed evacuated system. This triggers nucleation of pentlandite, a metal rich mineral and facilitates nucleation. Examination of the exsolution textures confirms different nucleation mechanisms for different sulfur to metal ratios (see Durazzo and Taylor, 1982; Etschmann et al., 2004). On the other hand, increasing S content results in a greater concentration of cation vacancies that will facilitate metal diffusion. Etschmann et al. (2004), using the classic Avrami method, calculated an approximate E_a for the exsolution of 5.0 $kJ.mol^{-1}$. However using the refined Avrami method, E_a varies from 2.0 to 21.0 $kJ.mol^{-1}$. The increase in E_a with y is related to the nucleation dominant stage at the beginning of reaction, and crystal growth controlled stage at the end. The in situ cooling and high temperature annealing experiments of Etschmann et al. (2004) showed that, after the initial exsolution, some of the pentlandite is resorbed indicating a high degree of supersaturation in the solid solution with M:S ratio of 1:1. The differences in E_a for pentlandite exsolution from $(Fe_{0.8}Ni_{0.2})S$ and $(Fe_{0.77}Ni_{0.19})S$ reflect the change of nucleation mechanism, from S vacancies to grain boundaries and S vacancies with the richer S compositions.

Overall our data and the work by Etschmann et al. (2004), and Yund and Hall (1970) indicate that low exsolution activation energies prevail in the pyrrhotite/pentlandite/pyrite system, although further experimental data are required to draw such general conclusions.

4. CONCLUSION

The pentlandite-*mss*/pyrrhotite exsolution reaction has multiple steps: nucleation, new phase growth and atomic diffusion, lamellae coarsening. These make its kinetic analysis difficult, as the mechanisms cannot be elucidated in detail. In mineral

reactions of this type the true functional form of the reaction model is almost never known, and the Arrhenius parameters determined by the classic Avrami method are skewed to compensate for errors in the model. The refined Avrami method employs the important concept that activation energy depends on reaction extent y. Kinetic study of pentlandite exsolution from *mss*/pyrrhotite was performed for the low temperature range from 473 to 573 K. For *mss*/pyrrhotite with bulk composition $(Fe_{0.77}Ni_{0.19})S$, activation energy of pentlandite exsolution, E_a varies from 49.6 kJ.mol^{-1} at the beginning of reaction (nucleation is dominant) to 20.7 kJ.mol^{-1} at the end (crystal growth is dominant).

In general, the activation energy varies during the course of solid reaction with the extent of reaction. The surrounding environment of reactant atoms affects the atom's activity and more or less account for changes of activation energy E_a. We are currently applying this refined Avrami method to further study of the pentlandite-*mss*/pyrrhotite and pyrite-pyrrhotite systems, where constancy of E_a fails to reveal details of the exsolution kinetics.

Acknowledgments—The authors wish to thank Barbara Etschmann and Andrew Putnis for the assistance with data collection and valued advice. We thank Prof. D.J. Vaughan and the three anonymous referees for their valuable comments and suggestions. This work is financially supported by Australian Research Council and Australian Institute for Nuclear Science and Engineering.

Associate editor: David Vaughan

REFERENCES

Arnold R. G. (1962) Equilibrium relations between pyrrhotite and pyrite from 325 to 743°C. *Econ. Geol.* **75,** 72–90.

Avrami M. (1939) Kinetics of phase change I. *J. Chem. Phys.* **7,** 1103–1112.

Avrami M. (1940) Kinetics of phase change II. *J. Chem. Phys.* **8,** 212–224.

Avrami M. (1941) Granulation, phase change and microstructure. *J. Chem. Phys.* **9,** 177–184.

Burke J. (1965) *The Kinetics of Phase Transformations in Metals*. Pergamon Press.

Christian J. W. (1965) *The Theory of Transformations in Metals and Alloys*. Pergamon Press.

Craig J. R. (1973) Pyrite-pentlandite assemblages and other low temperature relations in the Fe-Ni-S system. *Am. J. Sci.* **273A,** 496–510.

Doyle C. D. (1961) Kinetic analysis of thermogravimetric data. *J. Appl. Polym. Sci.* **5,** 285–292.

Durazzo A. and Taylor L. A. (1982) Exsolution in the *mss*/pyrrhotite-pentlandite system: Textural and genetic implications for Ni-sulfide ores. *Min. Dep.* **17,** 313–332.

Etschmann B., Pring A., Putnis A., Grguric B. A., and Studer A. (2004) A kinetic study of the exsolution of pentlandite $(Ni,Fe)_9S_8$ from the monosulfide solid solution (Fe,Ni)S. *Am. Mineral.* **89,** 39–50.

Farrell S. P. and Fleet M. E. (2002) Phase separation in $(Fe, Co)_{1-x}$ monosulfide solid-solution below 450°C, with consequences for coexisting pyrrhotite and pentlandite in magmatic sulfide deposits. *Can. Mineral.* **40,** 33–46.

Fleet M. S. (1968) On the lattice parameters and superstructures of pyrrhotites. *Am. Mineral.* **53,** 1846–1855.

Francis C. A., Fleet M. E., Misra K., and Craig J. R. (1976) Orientation of exsolved pentlandite in natural and synthetic nickeliferous pyrrhotite. *Am. Mineral.* **61,** 913–920.

Friedman H. (1964) Kinetics of thermal degradation of char-forming plastics from thermogravimetry: Application to a phenolic plastic. *J. Polym. Sci. C.* **6,** 183–195.

Hunter B. A. (1997) Rietica for Windows, ANSTO Press, Sydney. pp. 1–22.

Kelly D. P. and Vaughan D. J. (1983) Pyrrhotine-pentlandite ore textures: A mechanistic approach. *Min. Mag.* **47,** 453–463.

Kullerud G. (1971) Experimental techniques in dry sulfide research. In *Research Techniques for High Pressure and High Temperature* pp. 288–315 (ed. G. C. Ulmer). Springer-Verlag.

Misra K. C. and Fleet M. E. (1973a) The chemical composition of synthetic and natural pentlandite assemblages. *Econ. Geol.* **68,** 518–539.

Misra K. C. and Fleet M. E. (1973b) Unit cell parameters of monosulfide, pentlandite and taenaite solid solutions within the Fe-Ni-S system. *Mater. Res. Bull.* **8,** 669–678.

Naldrett A. C., Craig J. R., and Kullerud G. (1967) The central portion of the Fe-Ni-S system and its bearing on pentlandite exsolution in iron-nickel sulfide ores. *Econ. Geol.* **62,** 826–847.

Ozawa T. (1965) A new method of analyzing thermogravimetric data. *Bull. Chem. Soc. Jpn.* **38,** 1881–1886.

Putnis A. (1992) *Introduction to Mineral Science.* Cambridge University Press.

Rajamani V. and Prewitt C. T. (1973) Crystal chemistry of natural pentlandites. *Can. Mineral.* **12,** 178–187.

Riley J. F. (1977) The pentlandite group $(Fe,Ni,Co)_9S_8$: New data and an appraisal of structure-composition relationships. *Min. Mag.* **41,** 345–349.

Toulmin P. □. and Barton P. B. (1964) A thermodynamic study of pyrite and pyrrhotite. *Geochim. Cosmochim. Acta* **28,** 641–671.

Vaughan D. J. and Craig J. R. (1974) The crystal chemistry and magnetic properties of iron in the monosulfide solid solution of the Fe-Ni-S system. *Am. Mineral.* **59,** 926–933.

Vaughan D. J. and Craig J. R. (1978) *Mineral Chemistry of Metal Sulfides*. Cambridge University Press.

Vyazovkin S. (1997) Evaluation of activation energy of thermally stimulated solid-state reactions under arbitrary variation of temperature. *J. Comput. Chem.* **18,** 393–402.

Vyazovkin S. (2000a) On the phenomenon of variable activation energy for condensed phase reactions. *New J. Chem.* **24,** 913–917.

Vyazovkin S. (2000b) Kinetic concepts of thermally stimulated reactions in solids: A view from a historical perspective. *Int. Rev. Phys. Chem.* **19,** 45–60.

Vyazovkin S. (2001) Modification of the integral isoconversional method to account for variation in the activation energy. *J. Comput. Chem.* **22,** 178–183.

Vyazovkin S. (2003) Reply to "what is meant by the term 'variable activation energy' when applied in the kinetics analyses of solid state decompositions (crystolysis reactions)?" *Thermochim. Acta* **392,** 269–271.

Vyazovkin S. and Lesnikovich A. (1990) Error in determining activation energy caused by the wrong choice of process model. *Thermochim. Acta* **165,** 273–80.

Vyazovkin S. and Dollimore D. (1996) Linear and nonlinear procedures in isoconversional computations of the activation energy of nonisothermal reactions in solids. *J. Chem. Inf. Comput. Sci.* **36,** 42–45.

Vyazovkin S. and Wright C. A. (1997) Kinetics in solids. *Annu. Rev. Phys. Chem.* **48,** 125–149.

Wang H., Ngothai Y., O'Neill B. and Pring A. (2003) The effects of S fugacity on the exsolution of pentlandite $(Fe, Ni)_9S_8$ from the monosulfide solid solution(Fe,Ni)S. Presented at CHEMECA 2003, 31st Annual Australian Chemical Engineering Conference, Adelaide, Australia.

Wiersma C. L. and Rimstidt J. D. (1984) Rates of reaction of pyrite and marcasite with ferric iron at pH 2. *Geochim. Cosmochim. Acta* **48,** 85–92.

Yund R. A. and Hall H. T. (1970) Kinetics and mechanism of pyrite exsolution from pyrrhotite. *J. Petrol.* **11,** 381–404.

Yund R. A. and McCallister R. H. (1970) Kinetics and mechanisms of exsolution. *Chem. Geol.* **6,** 5–30.

CHAPTER FIVE

NOTE: Statement of coauthorship appears in the print copy of the thesis held in the University of Adelaide Library.

Available online at www.sciencedirect.com
SCIENCE DIRECT®
Thermochimica Acta 427 (2005) 13–25
thermochimica acta
www.elsevier.com/locate/tca

Phase evolution and kinetics of the oxidation of monosulfide solid solution under isothermal conditions

Haipeng Wang[a,*], Allan Pring[b,c], Yaning Xie[d], Yung Ngothai[a], Brian O'neill[a]

[a] *School of Chemical Engineering, University of Adelaide, SA 5005, Australia*
[b] *Department of Mineralogy, South Australian Museum, SA 5001, Australia*
[c] *School of Earth and Environmental Science, University of Adelaide, SA 5005, Australia*
[d] *Beijing Synchrotron Radiation Laboratory, Institute of High Energy Physics, Beijing 100039, PR China*

Received 18 June 2004; received in revised form 31 July 2004; accepted 6 August 2004
Available online 15 September 2004

Abstract

In this work, the effects of stoichiometry on phase evolution during the oxidation of *mss* (monosulfide solid solution) were investigated. A series of *mss* samples, ranging from $Fe_{7.9}S_8$ to $Fe_{2.37}Ni_{5.53}S_8$ were synthesized from pure components. Samples with grain size 53–90 μm were oxidized at 830 and 850 K in air in a muffle furnace. The *Rietveld* quantitative phase analysis method was used to identify and quantify the phase information from powder X-ray diffraction (XRD) profiles.

Hematite was observed and accounted for most of the oxidized iron. Nickel in *mss* was not oxidized to NiO under current isothermal conditions; instead, it was finally transformed to $Ni_{17}S_{18}$. Hematite, $Fe_2(SO_4)_3$ and residual *mss* were identified in the final phases after 24 h oxidation of the *mss* composition $Fe_{7.9}S_8$; hematite and $Ni_{17}S_{18}$ for compositions $Fe_{6.15}Ni_{1.54}S_8$ and $Fe_{2.37}Ni_{5.53}S_8$; hematite, $Ni_{17}S_{18}$ and pentlandite for $Fe_{6.4}Ni_{1.6}S_8$.

Given a constant iron to nickel atomic ratio of 4:1, the sample with lower metal concentration, $Fe_{6.15}Ni_{1.54}S_8$, showed a faster oxidation rate than its metal richer counterpart, $Fe_{6.4}Ni_{1.6}S_8$. The mean oxidation rates for these two samples are 1.85×10^{-4} and $1.22 \times 10^{-4}\,s^{-1}$ respectively for 1.5 h heating at 830 K. Vyazovkin's theory of changing activation energy (E_a) with reaction extent (y) was employed in the current kinetic study. The activation energy was determined using a model-free method. The oxidation of $Fe_{6.4}Ni_{1.6}S_8$ exhibited a higher E_a than $Fe_{6.15}Ni_{1.54}S_8$ over the course of reaction. The activation energy increases with y from 67.1 to 103.3 kJ mol^{-1} for *mss* composition $Fe_{6.15}Ni_{1.54}S_8$; 76.1 to 195.0 kJ mol^{-1} for $Fe_{6.4}Ni_{1.6}S_8$.

Bulk compositions $Fe_{7.9}S_8$, $Fe_{2.37}Ni_{5.53}S_8$ were selected to give a constant metal to sulfur atomic ratio of 7.9:8. Oxidation of $Fe_{2.37}Ni_{5.53}S_8$ achieved equilibrium within 1 h, compared to 5 h for $Fe_{7.9}S_8$.

Keywords: Kinetics; Model free; Monosulfide solid solution; Oxidation; Phase evolution

1. Introduction

The monosulfide solid solution $(Fe, Ni)_{1-x}S$, is an important precursor of primary iron–nickel sulfides in ore deposits. At high temperatures (>883 K) $(Fe, Ni)_{1-x}S$ has the NiAs structure and is known as the monosulfide solid solution (*mss*). Above 883 K, there is complete solid solution between Fe- and Ni-end-members; below this temperature it decomposes to form pyrrhotite and pentlandite [1]. The composition and stoichiometry of the monosulfide solid solution are variable but in nature it rarely exceeds Ni to Fe atomic ratio of 1:4. The variation in *mss* composition is due to the diversity of primary ore bodies as well as alterations due to supergene environment and weathering over geological time [2]. In this work, samples were prepared to give different iron to nickel atomic ratios (Fe:Ni) and different metal to sulfur ratios (M:S). The variable stoichiometry of *mss* leads

* Corresponding author. Tel.: +61 8 82077659; fax: +61 8 82077222.
E-mail address: haipeng.wang@adelaide.edu.au (H. Wang).

0040-6031/$ – see front matter © 2004 Elsevier B.V. All rights reserved.
doi:10.1016/j.tca.2004.08.007

to different oxidation mechanisms as well as phase evolution procedures during the oxidation.

Violarite and pentlandite (often accompanied by pyrrhotite/*mss*) are important nickel ores used as feedstock in flash smelting processes to produce nickel matte [3]. Monosulfide solid solution is a common intermediate phase observed during the oxidation of violarite and pentlandite. Therefore, the investigation of *mss* oxidation is of benefit in understanding the thermal behavior of these economically important metal sulfides. In this work, oxidation temperature of 830 and 850 K were chosen, as they are above the onset decomposition temperature of these economic metal sulfides (violarite and pentlandite) to *mss*, 723 K [3,4].

Oxidation behaviors of economic metal sulfide ores under heating schedules have been well studied [3,5–7]. The oxidation of *mss* starts at a very low temperature under atmospheric conditions. The dominant oxidation products from *mss* are ferrous sulfate and hematite in the temperature range 413–483 K; ferrous sulfate starts decomposing to *mss* and hematite when the temperature reaches 733 K [5]. It was postulated by Sliullin and Gitis that *mss* is first converted to sulfate during oxidizing roasting before being converted to oxides [8]. Banerjee proposed that the oxidation of *mss* starts at relatively low temperatures where iron is preferentially oxidized to metal sulfate accompanied by the release of SO_2 [5]. At elevated temperatures, the iron (III) sulfate will be transformed to a porous Fe_2O_3 layer.

Oxidation studies on metal sulfides are generally carried out under three sets of conditions: (i) under hydrothermal conditions, (ii) under heating conditions, where the temperature increases at a steady rate, and (iii) under vigorously oxidizing conditions, where metal sulfides are ignited [2,9–13]. The thermodynamics and kinetics of metal sulfide oxidation were extensively investigated in each of these methods. However, these methods do not provide enough evidence to reveal the reaction mechanism and kinetic behavior under isothermal conditions. Metal sulfides oxidize in a stepwise reaction sequence with increasing temperature; different reactions in this sequence are governed by different reaction mechanisms. The reaction mechanisms can also be different for the same reaction, if undertaken at different temperatures. Kinetic studies under isothermal conditions, on the other hand, investigate the kinetic behavior during the oxidation at a constant temperature. The reaction mechanism can be better understood using isothermal kinetic data and phase evolution evidence acquired from isothermal experiment. This work focused on the oxidation behaviors of *mss* under isothermal conditions.

The oxidation rate of *mss* is also dependent on particle size and oxygen partial pressure. Smaller particle size and increased oxygen partial pressure accelerate the process of oxidation. However, when the temperature exceeds 825 K the particle size effect becomes less significant and the oxidation rate is virtually independent of the particle size [7]. The applicability of this result to the current study remains uncertain but carrying out the oxidation experiment at elevated temperatures certainly will reduce the affect of particle size on the oxidation rate. To simplify the kinetic analysis, the current oxidation study was performed in an air atmosphere at 830 and 850 K. The particle size was confined to the range 53–90 μm. The experimental kinetic results only apply to this specified particle range. The effect of particle size on the oxidation kinetics is not concerned in this paper.

Earlier works on oxidation and thermal decomposition of metal sulfides concentrated on natural samples from various ore deposits, which contained different types of impurities [5,8]. The present study is confined to synthetic samples, which minimize the complexity of analysis caused by trace impurities in natural sulfides. Generalized mechanisms derived from experiments on synthetic samples may also apply to natural samples.

2. Experimental

2.1. Synthesis

The standard silica-tube techniques [1,14] were adopted to synthesize the monosulfide solid solution (*mss*). Accurately weighed stoichiometric amounts of Fe (1 mm diameter wire, 99.9+%, Aldrich), Ni (1 mm diameter wire 99.9+%, Aldrich) and S (granules 99.99+%, Aldrich) were sealed under vacuum in 10 mm diameter silica tubes. Bulk compositions of *mss* $Fe_{7.9}S_8$, $Fe_{2.37}Ni_{5.53}S_8$, $Fe_{6.15}Ni_{1.54}S_8$, $Fe_{6.4}Ni_{1.6}S_8$ were selected to provide different iron and nickel contents as well as different metal to sulfur ratios. The charges were heated slowly to 573 K, then up to 773 K and finally to1073 K, soaking for 12 h at each stage [15,16]. The slow heating schedule and soaking process were employed to minimize tube failure due to the high sulfur vapour pressure above 723 K. The tubes were quenched to room temperature in cold water. The charges were removed from the tubes and ground to fine powder under acetone, ensuring the homogeneity of the *mss*. The charges were then resealed in silica tubes and heated at 1373 K for 2 h, cooled to 1173 K, annealed for 7 days, and then quenched in a large volume of cold water. This resulted in homogenous samples with a relatively uniform 0.5 mm grain size.

2.2. Oxidation

Mss samples were ground to fine power using an agate mortar and then sieved to ensure particle size ranging from 53 to 90 μm. Each charge of 0.1 g *mss* powder was placed in an open platinum crucible. Oxidation experiments were performed in a muffle furnace (Kilnwest Ltd.) at 830 and 850 K, 1 atm. The samples were placed in the preheated furnace and a series of oxidation periods ranging from 0.5 to 24 h were adopted. The platinum crucibles containing the oxidized samples were carefully removed from the furnace with a pair of tweezers and then quenched by only dipping the

bottom of the crucible into water, avoiding water contamination. The temperatures were controlled within an error range ±5 K.

2.3. X-ray diffraction

Room temperature X-ray diffraction patterns of the quenched products were obtained using a *Guinier Hägg* camera with Cr $K\alpha_1$ radiation (λ = 2.2897 Å). Samples were ground with acetone in an agate mortar and pestle to produce an optimum grain size below 10 μm. The finely powdered sample was mixed with a small amount of pure Si, which acted as an internal standard. The *Guinier Hägg* films were scanned in *TPU/Pos* mode using an Epson film scanner and the powder diffraction profile over 2θ range 10–90° was extracted using the program *Scion Image* and the *Universal-Si-Calibration*, a macro function based on *Igor Pro* Version 4.0 [17].

The *Rietveld* method [18,19] was used to analyse the X-ray powder diffraction profiles. This method reveals the detailed structure and composition of a polycrystalline sample [20]. The *Pseudo-Voigt* function was adopted to model the peak shapes of X-ray diffraction patterns. Refined parameters were: peak shape variables (*U*, *V*, *W*), background (*Shifted Cheby* I function), scale factor (*S*), cell parameters (*a*, *b*, *c*, α, β, γ), and thermal displacement (B). The refinement of these parameters integrates each intensity into a properly shaped reflection, which contributes to the overall diffraction pattern. The result is a calculated X-ray diffraction profile, which best-fits the experimental intensities of X-ray diffraction peak. GOF (goodness of fit) was used to assess the success or otherwise of the refinement procedure.

Quantitative phase analysis was performed on oxidized samples using the formalism described by Hill and Howard [21]. The general scattering cross-section for *Bragg* scattering (scale factor *S*) is proportional to *N*/*V*, where *N* is the number of unit cells contributing to the scattering and *V* the unit cell volume [22]. The weight fraction of a phase can be described as:

$$w_i = \frac{(\mathrm{SZMV})_i}{\sum (\mathrm{SZMV})_i} \tag{1}$$

where w_i is the weight fraction of phase *i*, *S* the scale factor, *Z* the number of formula units per unit cell, *M* the molecular weight of the formula unit, and *V* the volume of unit cell.

Any variation of the stoichiometry of *mss* over the course of oxidation will be reflected in changes in the cell parameters. Thus, the cell parameters are refined for each X-ray powder profile. Initial input cell parameters and atom positions for the *Rietveld* refinement were taken from Alsen for $(Fe, Ni)_{1-x}S$, Collin et al. for $Ni_{17}S_{18}$, Pearson and Buerger for $(Fe_{4.5}Ni_{4.5})S_9$, Pauling and Hendricks for Fe_2O_3, and Christidis and Rentzeperis for $Fe_2(SO_4)_3$ [23–27].

2.4. SEM examination

Samples of three different bulk compositions of *mss* series, $Fe_{7.9}S_8$, $Fe_{2.37}Ni_{5.53}S_8$, $Fe_{6.15}Ni_{1.54}S_8$ were examined using a PHILIPS XL20 scanning electron microscope to reveal surface feature evolution during oxidation. Non-oxidized *mss* specimens were polished to produce smooth surfaces, and then placed in a preheated muffle furnace oxidized for up to 24 h at 830 K (dry air atmosphere).

3. Kinetic theory

Solid-state reaction kinetics is based on the *Activated State* theory, where the reaction rate can be written as:

$$\frac{\mathrm{d}y}{\mathrm{d}t} = kf(y) \tag{2}$$

where *y* is the reaction extent, *k* the rate constant, and *f*(*y*) the function of kinetic model.

Under current experimental conditions, the results show that the Fe in *mss* was oxidized to hematite, whilst Ni was eventually transformed to $Ni_{17}S_{18}$, a phase which has the pyrrhotite structure. Either hematite or $Ni_{17}S_{18}$ (wt.%) can be used to determine the extent of reaction. As most of the *mss* compositions examined were Fe-rich, the reaction extent was calculated on the basis of hematite fraction to minimize systematic errors amplified by mathematical calculation. The weight percentage of hematite was converted into reaction extent (*y*) using the following equation:

$$y = \frac{w_t - w_0}{w_e - w_0} \times 100\% = \frac{w_t}{w_e} \times 100\% \quad (w_0 = 0) \tag{3}$$

where *y* is the reaction extent; w_0, w_e, w_t are the weight fractions of hematite, at the beginning of reaction (t = 0), at the end of reaction($t = \infty$) and at an arbitrary time *t*, respectively [16,28]. Assuming complete oxidation of Fe to hematite, the calculated equilibrium weight fraction of hematite was derived by mass balance. The kinetic behavior of *mss* oxidation can be investigated by inspecting the relationship between reaction extent (*y*) and reaction time (*t*).

It is well known that rate constants are exponentially dependent on the inverse of absolute temperature. The dependence of *k* on temperature has the general form of the *Arrhenius* equation:

$$k = A \exp\left(\frac{E_\mathrm{a}}{RT}\right) \tag{4}$$

The disadvantage of this method is that the calculated value of *k* depends on the empirical selection of the function *f*(*y*), the kinetic model in Eq. (2) and therefore E_a depends on the choice of rate equation. Unfortunately, a number of different forms of the rate equation may fit the data equally well, but result in different values of E_a [29].

A second disadvantage is that it assumes that E_a does not change during the course of an isothermal transformation.

Vyazovkin explained the dependence of activation energy on reaction extent, caused by changing physical and mechanical properties of reaction medium [30].

Vyazovkin discussed isoconversional methods that employ the notion of the dependence of the activation energy on the reaction extent to predict the kinetic behavior of a reaction outside of the range of experimental temperatures [31]. Model-free methods can be adopted to avoid the problems associated with choosing an over simplified kinetic model. Vyazovkin and Dollimore introduced a unified approach to kinetic processing of non-isothermal data [32].

In this work, isothermal data were used to calculate E_a. It is postulated that E_a is a function of y. Hence, the basic kinetic equation can be rewritten as:

$$\frac{dy}{dt} = k(T, y)f(y) \tag{5}$$

where T is the absolute temperature, $k(T, y)$ the rate constant and $f(y)$ of a kinetic model. Rewriting Eq. (5) and substituting Eq. (4) for $k(T, y)$ give,

$$\ln\frac{dy}{dt} = \ln A + \ln f(y) - \frac{E_a(y)}{RT}$$

For a given segment of the reaction $y = y_0$, $\ln f(y_0)$ and $E_a(y_0)$ are constant. Therefore, the model-free determination of E_a gives:

$$E_a(y_0) = -R\frac{\ln dy/dt(y_0, T_1) - \ln dy/dt(y_0, T_2)}{(1/T_1 - 1/T_2)} \tag{6}$$

where $dy/dt(y_0, T_1)$ and $dy/dt(y_0, T_2)$ are reaction rates to a given value of y_0 at two different temperatures T_1 and T_2, respectively.

4. Results and discussion

4.1. Oxidation mechanism

Although the oxidation mechanism of metal sulfides has been addressed by a number of researchers, general conclusions have not been established [5–7]. A popular hypothesis, the "Shrinking-Unreacted Core" model is widely accepted [33,34]. According to this theory, solid particles in an oxygen gas stream are oxidized through gaseous diffusion of O_2 to the reaction interfaces and controlled by the rates of both chemical reaction and mass transport [4]. The *mss* oxidation is initiated at the grain surfaces and then moves towards the unreacted shrinking core. Chamberlain states that, for the oxidation of *mss*, the particles pass through an induction stage, during which sulfur is disassociated from the surface and gaseous sulfur oxides are released [4]. The kinetic data from the current study show that the oxidation of *mss* is so rapid that the induction stage could not be identified due to the difficulty of collecting data on a very short time frame. The experimental data indicate that the *mss* oxidation is a simple decelerating process. It starts at a relative high reaction rate and levels out at the end, due to the thickening of the inhibiting oxide layer. The ever-thickening oxide layer results in a porous surface [35–39]. The porosity of the oxide layer is caused by sulfur evolution during the induction stage of oxidation [2]. Fig. 1 shows the porous surfaces of samples: $Fe_{7.9}S_8$, $Fe_{6.15}Ni_{1.54}S_8$, $Fe_{2.37}Ni_{5.53}S_8$, after being oxidized at 830 K for 1, 1 and 1.5 h, respectively. The EDX composition analysis shows a slightly lower sulfur and higher oxygen content around the pits than that of the smooth surfaces (in Fig. 1). However, no statistically valuable data were obtained due to the small size and high concentration of the pits. Most of the EDX data were more like average compositions of the void and smooth surface. For the composition $Fe_{7.9}S$, EDX shows that after prolonged oxidation virtually no sulfur was detected on the granular surface. Similarly, a distinct decrease in sulfur content occurred for the oxidation of other *mss* compositions. These results indicate the continuous release of sulfur during the oxidation of *mss*.

X-ray diffraction profiles of the oxidized *mss* samples demonstrate that the Fe is preferentially oxidized to hematite; Ni, instead, is finally transformed to $Ni_{17}S_{18}$. This conforms to the results of previous researchers [40–46]. Dunn [47] and Chamberlain and Dunn [48] proposed that during the oxidation of metal sulfides, Fe migrates towards the outer rim where it is preferentially oxidized leaving a Ni-rich *mss* core. This preferential oxidation occurs once the partial pressure of the evolved sulfur gas decreases sufficiently to allow the diffusion of oxygen through the porous layer.

For the Ni free sample $Fe_{7.9}S_8$, the oxidation of Fe (within the first hour of reaction) leaves a much more distinctly porous surface than that of the sample $Fe_{6.15}Ni_{1.54}S_8$ (Fig. 1a–d). These micrographs of Fe-rich and pure Fe *mss* samples show the evolving surface features, from porous to grainy, during oxidation. For the Ni-rich sample $Fe_{2.37}Ni_{5.53}S_8$, a surface with sporadic pits does not appear until the oxidation reaches equilibrium (Fig. 1e and f).

4.2. Oxidation reactions

Oxidation products of *mss* were determined from the powder X-ray diffraction profiles. The intermediate and final products of the oxidation are dependent on the stoichiometry of *mss*. The desulfuration and release of SO_2 are responsible for the induction stage of the oxidation [4]. The major reactions at this stage are:

$$(Fe, Ni)_{1-x}S \rightarrow (Fe, Ni)_{1-x}S_{1-y} + \tfrac{1}{2}yS_2 \tag{7}$$

$$\tfrac{1}{2}yS_2 + yO_2 \rightarrow ySO_2 \tag{8}$$

Following the induction stage, the principal reaction is the preferential oxidation of iron in *mss* to hematite. The onset temperature of this reaction remains unsolved, although a wide range of temperatures have been reported for this reaction [4–8]. In the current study,

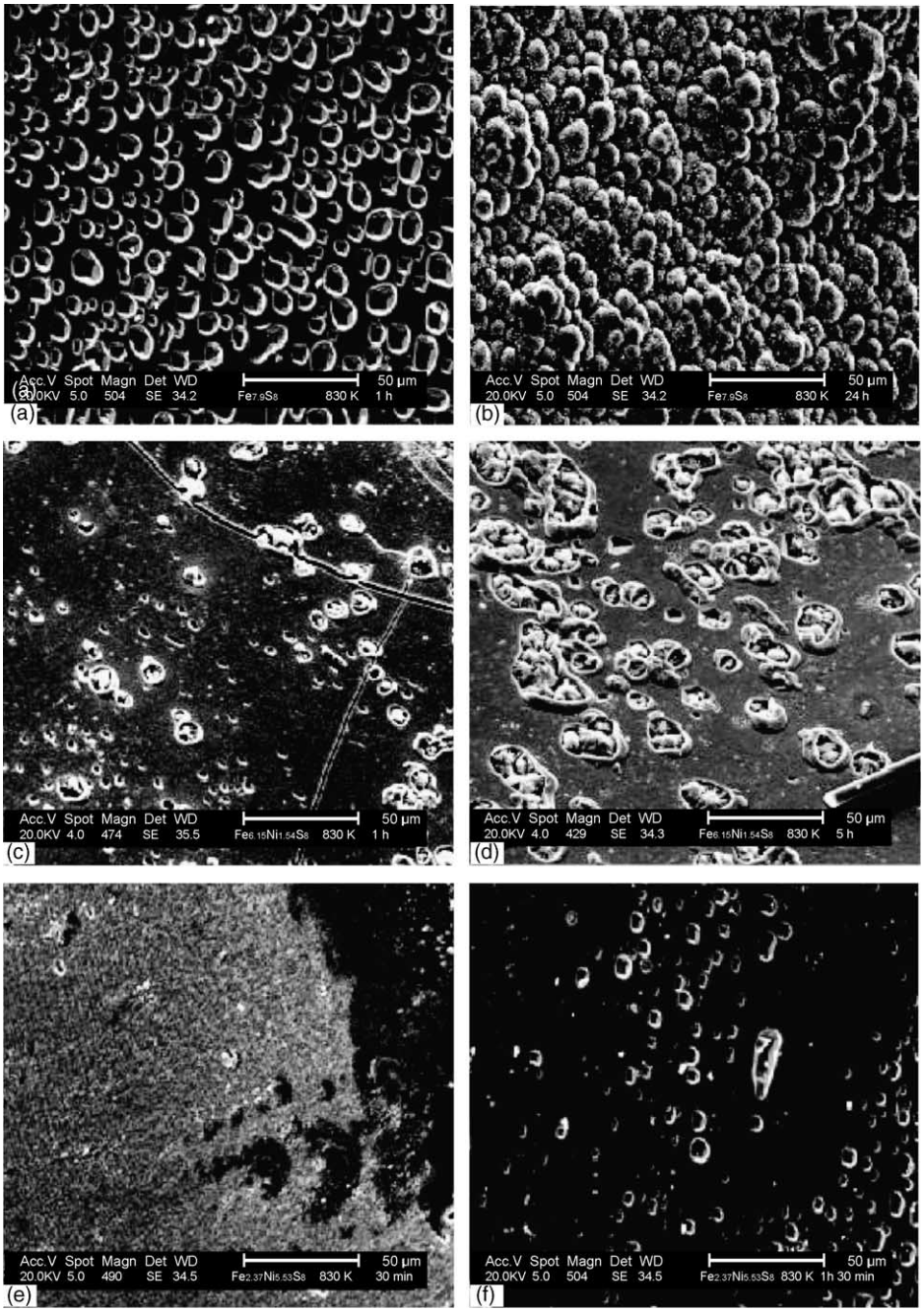

Fig. 1. SEM micrographs of the surface feature for oxidized *mss* samples. The oxidation was performed at 830 K, 1 atm. Micrographs (a) and (b) were taken after 1 and 24 h oxidation for $Fe_{7.9}S_8$; (c) and (d): 1 and 5 h oxidation for $Fe_{6.15}Ni_{1.54}S_8$; (e) and (f): 0.5 and 1.5 h oxidation for $Fe_{2.37}Ni_{5.53}S_8$.

hematite was observed as the major oxidation product of *mss* at 830 and 850 K. Some minor or intermediate phases were also identified in the X-ray powder diffraction profiles.

For the pure Fe *mss* ($Fe_{7.9}S_8$), hematite, mikasaite ($Fe_2(SO_4)_3$) and residual *mss* were identified in the charge after 24 h oxidation at 830 K in air (Table 1). For Fe–Ni *mss* compositions, hematite and $Ni_{17}S_{18}$ were observed as the final oxidation products for experiments carried out under the same conditions. Magnetite was not observed, which contradicts the results of Asaki et al. [6]. Magnetite, if present, is below the detection limits of *Rietveld* profile fitting methods (around 1 wt.% of product). Apart from these main oxidation products, up to 5.7 wt.% of an intermediate phase, pentlandite, was observed for the sample $Fe_{6.4}Ni_{1.6}S_8$ (Tables 2 and 3). Pentlandite was not an equilibrium product in this oxidation. Exsolved pentlandite was eventually oxidized to produce hematite and $Ni_{17}S_{18}$. Pentlandite will exsolve from *mss* when *mss* is heated above 450 K [15]. It was reported that the activation energy of pentlandite exsolution

Table 1
Phase evolution during the oxidation of nickel-free *mss* ($Fe_{7.9}S_8$) at 830 K

Time (h)	wt.% mik.	a_{mik} (Å)	c_{mik} (Å)	wt.% *mss*	a_{mss} (Å)	c_{mss} (Å)	V_{mss} (Å^3)	wt.% hem.	a_{hem} (Å)	c_{hem} (Å)
0.0				99.9(2)	3.4506(2)	5.8156(6)	59.968(7)			
1.0	1.1(2)	8.236(1)	22.178(3)	72.3(8)	3.4479(3)	5.7314(9)	59.01(1)	26.6(6)	5.026(2)	13.764(5)
5.0	5.7(2)	8.235(1)	22.177(3)	15.3(6)	3.4488(7)	5.5443(2)	57.09(3)	79.0(8)	5.0234(6)	13.781(2)
24.0	5.4(2)	9.237(1)	22.176(3)	14.5(6)	3.4486(7)	5.5422(2)	57.08(3)	80.1(8)	5.0238(5)	13.775(2)

Summary of cell parameters and unit cell volume for each phase: wt.% mik., wt.% *mss*, wt.% hem. are weight fractions for mikasaite, *mss* and hematite. a_{mik}, c_{mik} are cell parameters for mikasaite; a_{mss}, c_{mss} and V_{mss} for *mss*; a_{hem}, c_{hem} for hematite. Estimated standard deviations are given in brackets.

Table 2
Phase evolution during the oxidation of iron–nickel *mss* at 830 K

Initial bulk composition	Time (h)	wt.% pent.	a_{pent} (Å)	V_{pent} (Å^3)	wt.% *mss*	a_{mss} (Å)	c_{mss} (Å)	V_{mss} (Å^3)	wt.% hem.	a_{hem} (Å)	c_{hem} (Å)
$Fe_{6.4}Ni_{1.6}S_8$	0.0				100.0(4)	3.4501(6)	5.810(1)	59.89(2)			
	0.5	1.5(7)	10.105(3)	1032.0(6)	80.3(8)	3.4521(1)	5.7546(5)	59.390(6)	18.2(7)	5.025(1)	13.767(4)
	1.0	5.7(7)	10.110(3)	1033.2(5)	53.9(7)	3.4505(6)	5.496(1)	56.67(2)	40.4(8)	5.041(2)	13.783(5)
	1.5	1.8(7)	10.118(5)	1035.8(6)	45.8(8)	3.4496(5)	5.416(1)	55.81(2)	52.4(7)	5.024(1)	13.787(3)
	5.0				23.1(7)	10.258(2)	15.991(6)	1457.4(8)	76.9(8)	5.0304(5)	13.756(2)
	24.0				23.2(7)	10.259(3)	16.008(7)	1459.1(9)	76.8(8)	5.031(1)	13.759(3)
$Fe_{6.15}Ni_{1.54}S_8$	0.0				99.9(3)	3.4477(6)	5.772(1)	59.42(2)			
	0.5				64.5(6)	3.4488(5)	5.542(1)	57.09(2)	35.5(8)	5.018(1)	13.778(4)
	1.0				36.1(8)	3.4481(5)	5.402(1)	55.63(2)	63.9(8)	5.0218(9)	13.768(3)
	1.5				24.1(8)	10.251(3)	16.018(7)	1457.7(9)	75.9(6)	5.031(1)	13.759(3)
	5.0				23.6(8)	10.251(3)	16.020(6)	1457.9(8)	76.4(7)	5.030(1)	13.754(3)
$Fe_{2.37}Ni_{5.53}S_8$	0.0				99.9(2)	3.4489(6)	5.530(1)	56.96(2)			
	0.5				77.7(7)	3.4418(8)	5.384(1)	55.23(2)	22.3(7)	5.013(2)	13.735(7)
	1.0				73.3(6)	10.368(1)	15.959(4)	1485.6(4)	26.7(4)	5.035(1)	13.772(6)
	1.5				74.2(8)	10.367(1)	15.960(3)	1485.4(4)	25.8(4)	5.035(2)	13.786(6)

Summary of cell parameters and unit cell volume for each phase: wt.% pent., wt.% *mss*, wt.% hem. are weight fractions for pentlandite, *mss* and hematite. a_{pent}, V_{pent} are cell parameters for pentlandite; a_{mss}, c_{mss} and V_{mss} for *mss*; a_{hem}, c_{hem} for hematite. Estimated standard deviations are given in brackets.

from *mss* is very low (around 5 kJ mol^{-1}) at the beginning of the exsolution for *mss* composition $Fe_{6.4}Ni_{1.6}S_8$ [15]. This may explain the observation of pentlandite during the oxidation of $Fe_{6.4}Ni_{1.6}S_8$. The proposed oxidation reactions for these *mss* samples are:For $Fe_{7.9}S_8$,

$$\begin{cases} Fe_{7.9}S_8 + 13.925O_2 \rightarrow 3.95Fe_2O_3 + 8SO_2 \\ Fe_{7.9}S_8 + 19.85O_2 + 3.85SO_2 \rightarrow 3.95Fe_2(SO_4)_3 \end{cases} \quad (9)$$

For $Fe_{2.37}Ni_{5.53}S_8$,

$$Fe_{2.37}Ni_{5.53}S_8 + 3.9222O_2 \rightarrow 1.185Fe_2O_3 + 0.3253Ni_{17}S_{18} + 2.1447SO_2 \quad (10)$$

For $Fe_{6.15}Ni_{1.54}S_8$,

$$Fe_{6.15}Ni_{1.54}S_8 + 10.982O_2 \rightarrow 3.075Fe_2O_3 + 0.0906Ni_{17}S_{18} + 6.37SO_2 \quad (11)$$

Table 3
Phase evolution during the oxidation of iron–nickel *mss* at 850 K

Initial bulk composition	Time (h)	wt.% pent.	a_{pent} (Å)	V_{pent} (Å^3)	wt.% *mss*	a_{mss} (Å)	c_{mss} (Å)	V_{mss} (Å^3)	wt.% hem.	a_{hem} (Å)	c_{hem} (Å)
$Fe_{6.4}Ni_{1.6}S_8$	0.0				100.0(3)	3.4499(5)	5.809(2)	59.87(2)			
	0.5	0.9(7)	10.105(3)	1031.8(5)	70.6(6)	3.4501(4)	5.662(1)	58.37(2)	28.5(7)	5.024(1)	13.777(4)
	1.0	5.1(7)	10.108(3)	1032.8(5)	41.8(6)	3.4509(5)	5.401(1)	55.70(2)	53.1(7)	5.026(2)	13.779(3)
	2.0				27.7(6)	3.4506(5)	5.346(1)	55.13(2)	72.3(7)	5.024(1)	13.783(3)
	3.0				23.2(6)	10.256(2)	16.011(6)	1458.5(8)	76.8(7)	5.029(2)	13.765(3)
	5.0				23.0(6)	10.259(2)	16.008(7)	1459.1(8)	77.0(7)	5.030(1)	13.768(3)
$Fe_{6.15}Ni_{1.54}S_8$	0.0				100.0(3)	3.4478(5)	5.770(2)	59.40(2)			
	0.5				49.4(7)	3.4485(5)	5.448(1)	56.11(2)	50.6(8)	5.020(1)	13.774(3)
	0.75				32.5(7)	3.4481(5)	5.398(2)	55.58(2)	67.5(8)	5.024(1)	13.770(3)
	1.0				24.9(7)	10.254(3)	16.022(5)	1458.9(8)	75.1(7)	5.032(1)	13.761(3)
	1.5				23.3(6)	10.255(3)	16.021(6)	1459.1(8)	76.7(7)	5.032(1)	13.757(3)
	2.0				23.4(6)	10.254(3)	16.023(6)	1459.0(8)	76.6(7)	5.030(1)	13.758(3)

Summary of cell parameters and unit cell volume for each phase: wt.% pent., wt.% *mss*, wt.% hem. are weight fractions for pentlandite, *mss* and hematite. a_{pent}, V_{pent} are cell parameters for pentlandite; a_{mss}, c_{mss} and V_{mss} for *mss*; a_{hem}, c_{hem} for hematite. Estimated standard deviations are given in brackets.

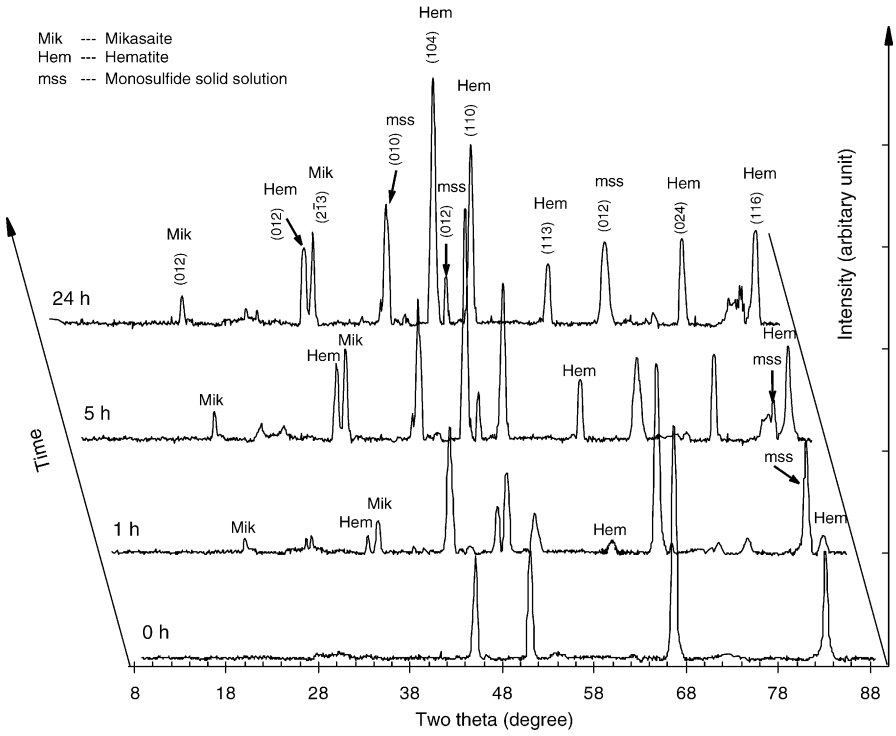

Fig. 2. Stack of X-ray powder diffraction patterns showing the progress of phase evolution during the oxidation of $Fe_{7.9}S_8$. The oxidation was taken under isothermal condition (830 K, 1 atm.). The time range for oxidation varied from 0 to 24 h.

For $Fe_{6.4}Ni_{1.6}S_8$,

$$\begin{cases} Fe_{6.4}Ni_{1.6}S_8 + 11.1059O_2 \\ \quad \rightarrow 3.2Fe_2O_3 + 0.09412Ni_{17}S_{18} + 6.306SO_2 \\ Fe_{6.4}Ni_{1.6}S_8 + 5.156O_2 \\ \quad \rightarrow 2.844(Fe_{4.5}Ni_{4.5})S_8 + 5.156SO_2 \\ (Fe_{4.5}Ni_{4.5})S_8 + 3.235O_2 \\ \quad \rightarrow 2.25Fe_2O_3 + 0.2647Ni_{17}S_{18} + 3.235SO_2 \end{cases} \quad (12)$$

4.3. Phase evolution

The pure iron *mss* $Fe_{7.9}S_8$ samples were oxidized at 830 K in air for periods up to 24 h. Fig. 2 shows the phases evolution over the oxidation. Diffraction patterns were collection at 0, 1, 5 and 24 h. The major oxidation product was hematite. A minor phase, mikasaite ($Fe_2(SO_4)_3$), was also detected. Distinct mikasaite peaks (0 1 2) and (2 1 3) were observed after 1 h. The diffraction intensity of mikasaite (iron (III) sulfate) increased to a maximum after 5 h and remained unchanged till the end of the oxidation experiment. The *Rietveld* resolved phase fraction of iron (III) sulfate increased up to 5.7 wt.% then remained constant after prolonged oxidation of pure Fe *mss* at 830 K. Following this stage, the oxidation is retarded and the oxide layer growth follows a parabolic rate law, where mass transfer through the gaseous boundary layer at sample surface and diffusion of oxygen through the oxide layer control the progress of oxidation. Banerjee detected iron (II) and (III) sulfates during the oxidation experiment of pyrrhotite. The iron (II) sulfate is more likely a precursor of iron (III) sulfate. In the current study iron (II) sulfate is not detected by XRD. This may due to the fast conversion rate of iron (II) to iron (III) at elevated temperatures, and the lack of data collected in very short time frames at the beginning of the reactions [5].

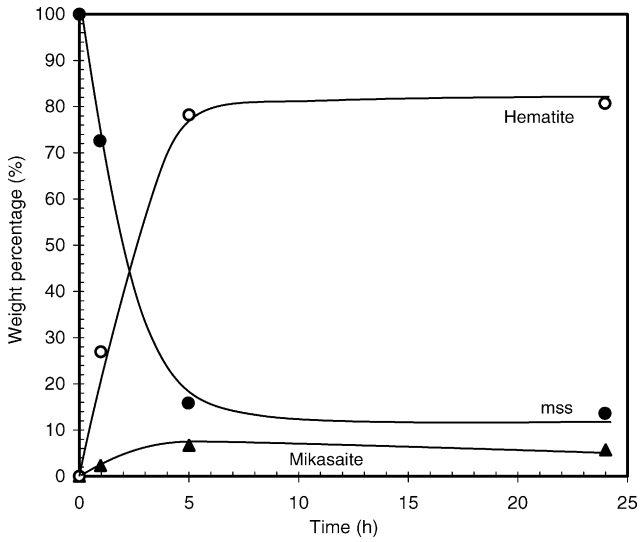

Fig. 3. Plot showing the progress of iron oxidation to hematite, producing mikasaite and decreasing weight fraction of *mss* during the oxidation of $Fe_{7.9}S_8$ at 830 K, 1 atm. The circle symbol represents the weight fraction of hematite; solid circle, for *mss*; solid triangle, for mikasaite. The curves are produced using least-square method to best-fit experimental data.

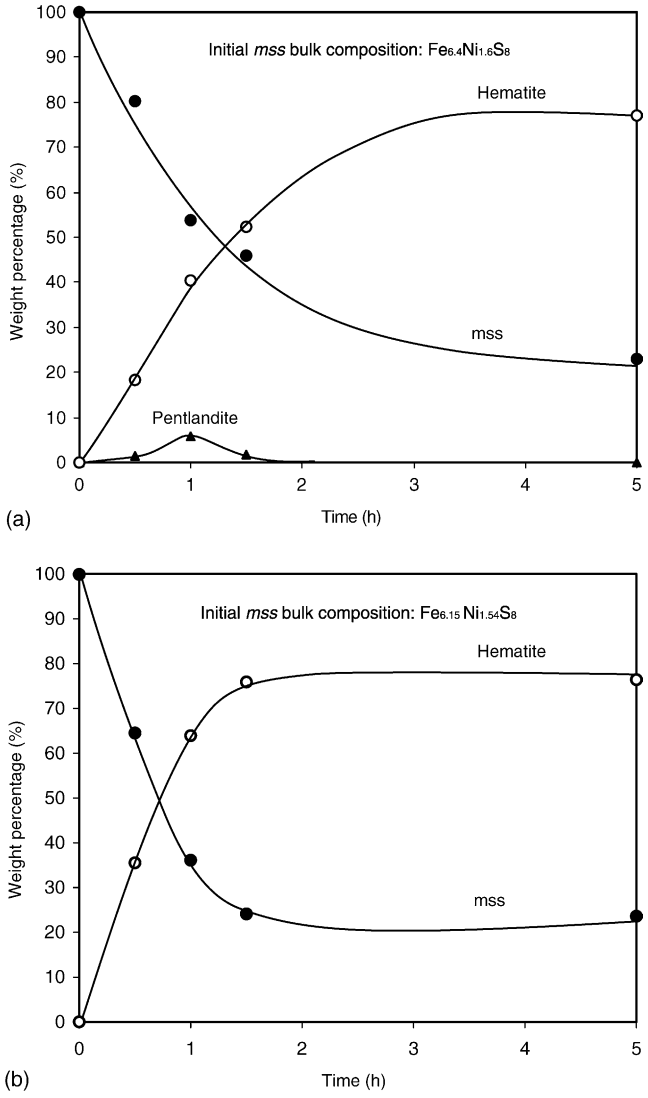

Fig. 4. Plot showing the evolving phase fractions during the oxidation of *mss* samples $Fe_{6.4}Ni_{1.6}S_8$ (a) and $Fe_{6.15}Ni_{1.54}S_8$ (b) at 830 K, 1 atm. Symbols (◯), (●) and (▲) are the representative for the weight percentage of hematite, *mss*, and pentlandite, respectively.

The weight fractions of each phase versus oxidation time are shown in Fig. 3. It is clear that the reaction rate was very rapid at the beginning and levelled out after 5 h annealing. It is worth noting that the residual *mss* was not oxidized even after prolonged oxidation. It was also observed that the former finely powdered samples formed hard conglomerates during oxidation. This inhibited the diffusion of oxygen and left an unreacted *mss* core.

The phase evolutions for the nickel containing (iron rich) *mss* samples, $Fe_{6.4}Ni_{1.6}S_8$ and $Fe_{6.15}Ni_{1.54}S_8$ are shown in Fig. 4a and b. The compositions of both samples were chosen to give an Fe:Ni atomic ratio of 4:1 but with different metal to sulfur ratios, 0.96:1 and 1:1, respectively. Hematite and $Ni_{17}S_{18}$ are the major final products (also see Eqs. (11) and (12)). An intermediate phase, pentlandite, was observed for the composition richer in metal $Fe_{6.4}Ni_{1.6}S_8$. The phase fraction of pentlandite reached a maximum after oxidation for 1 h. The following continuous decrease of pentlandite can be explained by the oxidation of pentlandite. Different onset decomposition temperatures of pentlandite have been reported by several researchers [2,4]. The maximum onset decomposition temperature of pentlandite was reported at 883 K, where Fe to Ni ratio was 1:1 [49]. This temperature decreased rapidly as the Fe to Ni atomic ratio deviated from the ideal value of 1:1. In the current oxidation study, the intermediate phase, pentlandite (exsolved from *mss*), is believed to have a changing Fe:Ni ratio. This may explain the lower oxidation temperature for pentlandite in this work. The composition of pentlandite can be determined from its cell edge [15]. Using the cell parameter data in Table 2, the calculated pentlandite compositions are $Fe_{4.5}Ni_{4.5}S_8$, $Fe_{4.9}Ni_{4.1}S_8$, and $Fe_{5.6}Ni_{3.4}S_8$ after *mss* $Fe_{6.4}Ni_{1.6}S_8$ was oxidized at 830 K for 0.5, 1.0 and 1.5 h, respectively.

The exsolution of pentlandite from the host phase and its subsequent oxidation are competitive steps, which result in a maximum weight fraction of pentlandite at some time during oxidation. Increasing metal content retards the oxidation of the metal sulfide but facilitates the pentlandite exsolution from the *mss* host [15,48,50]. In the current study, pentlandite was only observed in the metal richer sample ($Fe_{6.4}Ni_{1.6}S_8$), which is related to the rapid exsolution of pentlandite from *mss* at the beginning of reaction. For the more sulfur rich sample ($Fe_{6.15}Ni_{1.54}S_8$), the accelerated oxidation rate overwhelmed the decelerated exsolution rate of pentlandite and no pentlandite was detected.

The oxidation of the Ni-rich sample, $Fe_{2.37}Ni_{5.53}S_8$ (830 K, 1 atm.) reached equilibrium within 1 h and yielded 26.7 wt.% hematite and 74.2 wt.% $Ni_{17}S_{18}$.

4.4. Structural modification

It is shown in Tables 1–3 that the cell parameters for hematite and mikasaite did not change significantly, when ex-

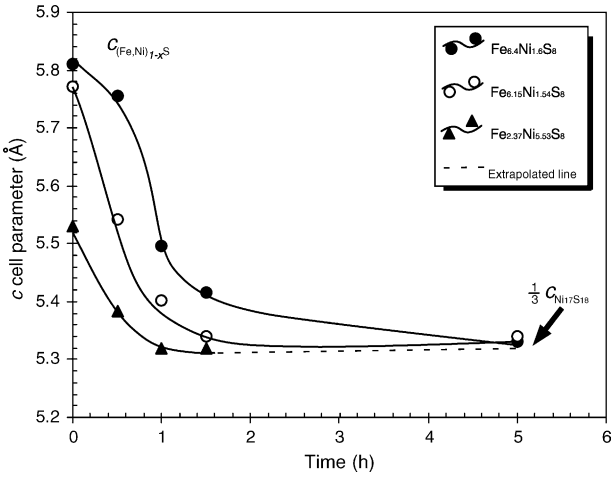

Fig. 5. Plot of c parameter versus retaining time over the oxidation at 830 K for three iron–nickel *mss* compositions ($Fe_{6.4}Ni_{1.6}S_8$, $Fe_{6.15}Ni_{1.54}S_8$ and $Fe_{2.37}Ni_{5.53}S_8$).

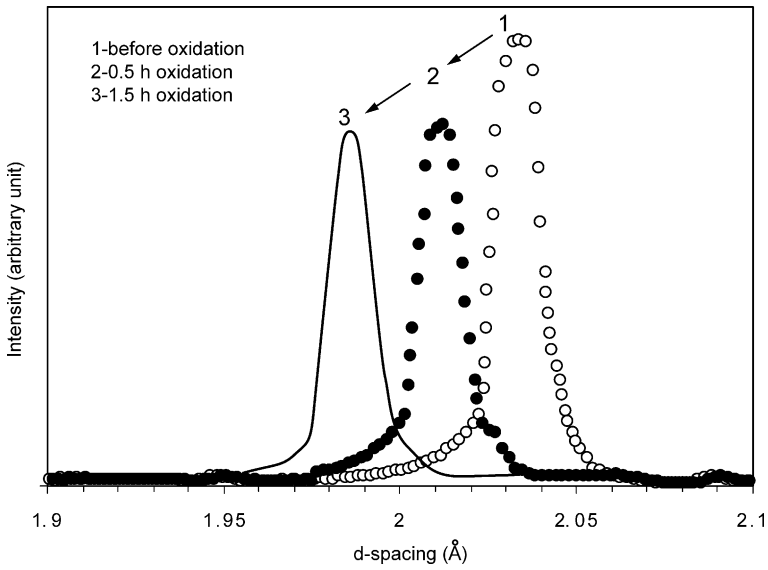

Fig. 6. Plot showing the shift of (0 1 2) peak in the X-ray profile of *mss* ($Fe_{2.37}Ni_{5.53}S_8$) during the oxidation at 830 K. The symbol (◯), (●) and solid curve represent the X-ray intensity for samples prior to oxidation, after 0.5 and 1.5 h oxidation.

perimental uncertainties are considered, during the oxidation indicating their compositions remains more or less constant on the time scale of these experiments. For *mss*, on the other hand, some distinct variation in the cell parameters was observed over the course of oxidation. This was caused by the variation of stoichiometry of *mss*. In general, sulfur-rich *mss* produces more cation vacancies, which results in a smaller unit cell volume. Replacing Fe with Ni also reduces unit cell volume of *mss*, especially the *c* parameter due to the smaller atomic diameter of Ni [51]. Fig. 5 shows the variation of the *c*

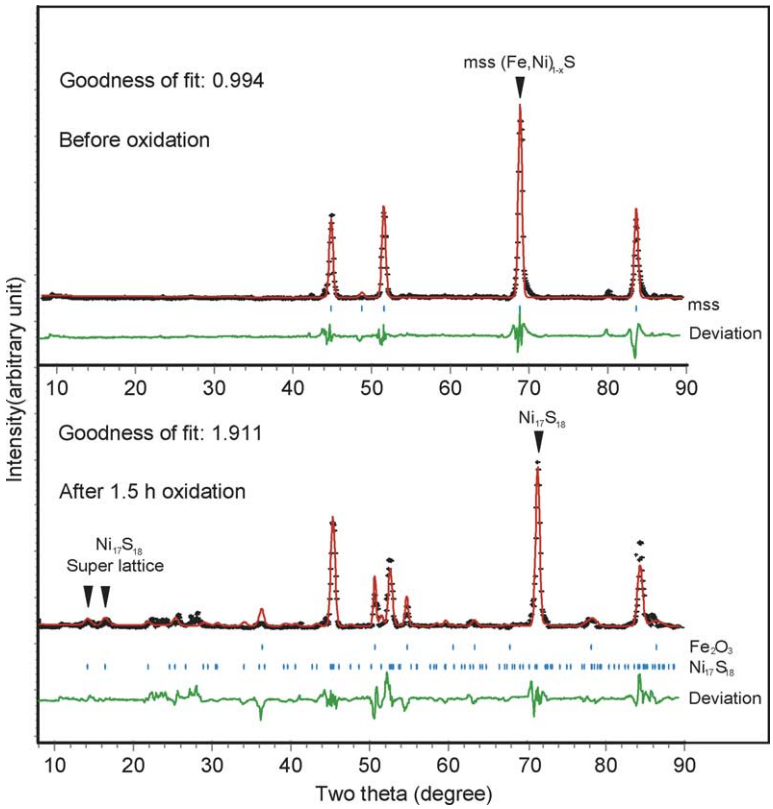

Fig. 7. The X-ray diffraction patterns taken before and after oxidation at 830 K for *mss* sample $Fe_{2.37}Ni_{5.53}S_8$. The appearance of two distinct diffraction peaks at small $2\theta = 14.1^\circ$ and 16.1° (*d*-spacing = 8.9396 and 7.8024 Å) indicated the formation of super-lattice for *mss*.

parameter for three iron–nickel *mss* samples ($Fe_{2.37}Ni_{5.53}S_8$, $Fe_{6.15}Ni_{1.54}S_8$, $Fe_{6.4}Ni_{1.6}S_8$) during the oxidation at 830 K. The *c* parameters for these samples start from 5.530, 5.772 and 5.810 Å respectively at the beginning of oxidation. The smallest *c* parameter of *mss* corresponds to the most nickel-rich sample, and the largest for the most Fe and also metal rich sample. As the oxidation progressed, the *c* parameter for all the three samples converged to a value around 5.330 Å. This is related to the formation of $Ni_{17}S_{18}$. The preferential oxidation of Fe in *mss* to hematite left a progressively nickel-enriched *mss* and eventually an almost pure nickel compound, $Ni_{17}S_{18}$ (pyrrhotite-type structure), at the end of oxidation. The ever nickel-enriching *mss* results in a decreasing *c* parameter during the oxidation. This is characterized by the (0 1 2) peak shifting to a smaller *d*-spacing in the X-ray diffraction pattern of *mss*. Fig. 6 shows that the (0 1 2) peak moved from *d*-spacing 2.0336 to 1.9858 Å after 1.5 h oxidation at 830 K for the *mss* composition $Fe_{2.37}Ni_{5.53}S_8$.

X-ray patterns were collected for these samples after the oxidation reaction reached equilibrium. The occurrence of two distinct diffraction peaks at *d*-spacing = 7.8024 and 8.9396 Å (correspond to the planes (0 1 0) and (0 1 1) of nickel sulfide $Ni_{17}S_{18}$) after the oxidation of sample $Fe_{2.37}Ni_{5.53}S_8$ for 1.5 h, indicates the formation of a super-lattice of $Ni_{17}S_{18}$ (Fig. 7). These peaks conformed to the X-ray diffraction profile of the $Ni_{17}S_{18}$ with space group *P*3 2, which was reported by Collin et al. [24]. It appears that the *mss* evolved from an iron–nickel *mss* with space group P6/mmc at the beginning of oxidation to a pure nickel sulfide ($Ni_{17}S_{18}$) with space group *P*3 2 at the end. The super-lattice of $Ni_{17}S_{18}$ has a tripled *c* parameter compared to the hexagonal iron–nickel *mss* (Fig. 8). The cell projections along [0 1 0] for (Fe, Ni)S and $N_{17}S_{18}$ show that the structural modification of *mss* from space group P6/mmc to *P*3 2 is a topotactic transition in which the anionic array is unchanged during the transition but cation is replaced and reorganization occurs, as $(Fe, Ni)_{1-x}S \rightarrow N_{17}S_{18}$.

4.5. Oxidation kinetics

The oxidation of *mss* has multi steps, involving various reactions. These make its kinetic analysis difficult, as the mechanisms cannot be elucidated in detail for every step. For mineral reactions of this type, the true functional form of the reaction model is almost never known, thus the Vyazovkin's notion of model-free determination of E_a should be applied to the kinetic study of *mss* oxidation in order to avoid any over simplified assumption of the kinetic models. The calculated E_a is empirical activation energy for the overall oxidation process, and is not confined to a specific step. The E_a varies with the reaction extent (*y*).

The effect of stoichiometry on the kinetic behavior of *mss* oxidation was investigated. Reaction extent was determined using Eq. (3). We assumed that all Fe in *mss* was oxidized to hematite and the Ni transformed to $Ni_{17}S_{18}$ at the end of oxidation. This hypothesis was verified by comparing the calculated and measured hematite weight fraction after oxidation

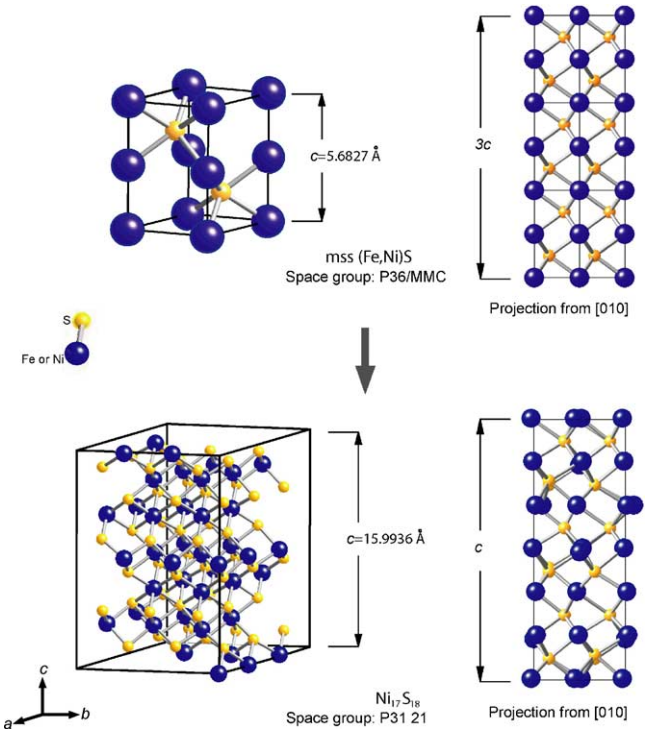

Fig. 8. Comparison of the crystal structure between iron–nickel *mss* (Fe, Ni)S and the nickel sulfide $Ni_{17}S_{18}$. The (Fe, Ni)S unit cell is enlarged for the purpose of good illustration.

achieved equilibrium (Table 4). The theoretical equilibrium hematite weight fractions are in good agreement with our experimental results, except for the *mss* composition $Fe_{7.9}S_8$. This may be caused by the effect of sintering of the finely grinded *mss* ($Fe_{7.9}S_8$) powder during the oxidation.

The samples were placed in a reheated furnace. If the samples were ignited at the elevated temperature, the surface temperature of these samples will differ from that of the furnace, and the calculated activation energies would have no general thermodynamic meaning. The possible ignited *mss* composition under current experimental conditions is $Fe_{7.9}S$, which conglomerated as the results of sintering. The E_a was only calculated for the compositions $Fe_{6.15}Ni_{1.54}S_8$ and $Fe_{6.4}Ni_{1.6}S_8$.

Table 4
Comparison of the theoretical and experimental hematite weight fraction after the oxidation of *mss* achieved equilibrium

Oxidation condition	Bulk mss composition	Theoretical equilibrium hematite (wt.%)	Experimental equilibrium hematite (wt.%)
830 K, 1 atm.	$Fe_{7.9}S_8$	100.00	80.00
	$Fe_{2.37}Ni_{5.53}S_8$	26.97	25.25
	$Fe_{6.15}Ni_{1.54}S_8$	77.50	76.15
	$Fe_{6.4}Ni_{1.6}S_8$	77.50	76.85
850 K, 1 atm.	$Fe_{6.15}Ni_{1.54}S_8$	77.50	76.90
	$Fe_{6.4}Ni_{1.6}S_8$	77.50	76.65

The completion of iron oxidation to hematite was assumed to derive the theoretical equilibrium hematite.

In this study, the equilibrium was defined as the oxidation products vary very little even over a prolonged period of reaction. The equilibrium phase fraction was determined by averaging the value of phase fractions over the two longest oxidation periods.

Reaction extent (y) is a function of reaction time (t). The plots of y versus t for the oxidation reactions of samples $Fe_{6.15}Ni_{1.54}S_8$ (M:S = 0.96) and $Fe_{6.4}Ni_{1.6}S_8$ (M:S = 1.00) are shown in Fig. 9a. Since the S-rich sample oxidized more rapidly and achieved equilibrium within 1.5 h, we can speculate that the increasing sulfur content in *mss* accelerates the oxidation process. For the sulfur-rich sample, more sulfur atoms were vapourized and reacted with oxygen. The sulfur oxidation to SO_2 is an exothermic chemical reaction. Chamberlain and Dunn proposed that abundant evolved sulfur, reacting with oxygen at the surface of the particle, increases the surface temperature of the particle and speeds the oxidation of iron to hematite [48]. Fig. 9b shows the time function of the reaction rate (dy/dt) for both samples (the S-rich and non-S-rich). These time functions were derived from the curves of $y \sim y(t)$ in Fig. 9a by differentiating y with respect to t. In order to show the induction stage (discussed in Section 4.1) for *mss* oxidation, the third order polynomial data fitting was used to give $y \sim y(t)$. The derivative $dy/dt \sim t$ curves in Fig. 9b show that the reaction rate increases to a maximum and then decreases to zero when the reaction approaches completion. It is worth noting that the induction stage was shown with the aid of a theoretical model. However, the experimental data in Fig. 9a only show a decelerating reaction rate due to the difficulty of data collection in a very short time frame, where the

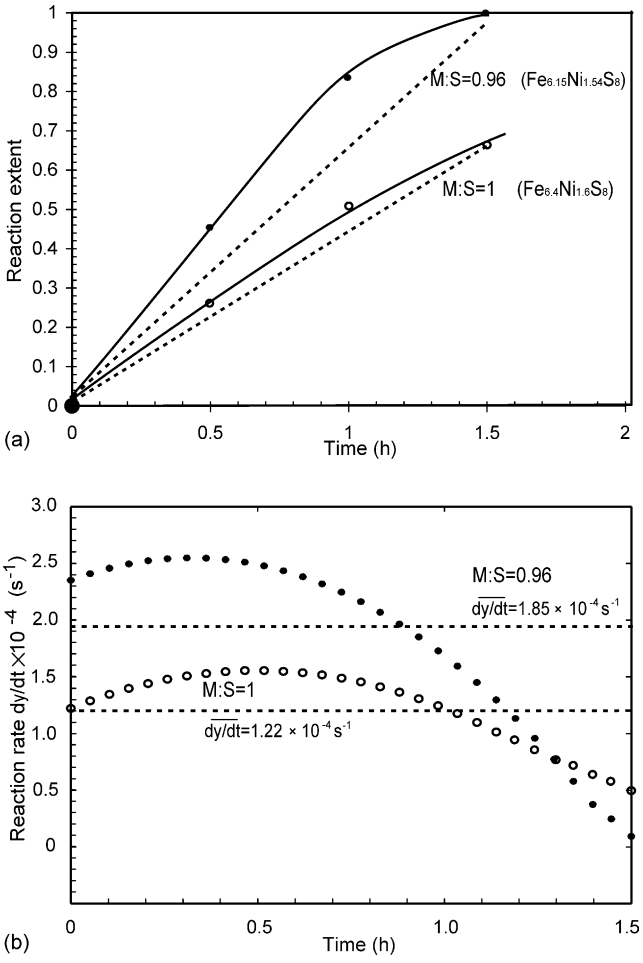

Fig. 9. (a) Progress of reaction extent with retaining time during the oxidation at 830 K for samples $Fe_{6.4}Ni_{1.6}S_8$ (M:S = 1), $Fe_{6.15}Ni_{1.54}S_8$ (M:S = 0.96). The circle symbol represents experimental data of reaction extent for the sample $Fe_{6.4}Ni_{1.6}S_8$; symbol star, for the sample $Fe_{6.15}Ni_{1.54}S_8$. The average reaction rate is derived from the slope of dashed line. (b) Dependence of reaction rate (dy/dt) on reaction time (t). The circle symbol represents calculated reaction rate for $Fe_{6.4}Ni_{1.6}S_8$; symbol of star, for $Fe_{6.15}Ni_{1.54}S_8$. The dashed line is the calculated average reaction rate over 1.5 h oxidation.

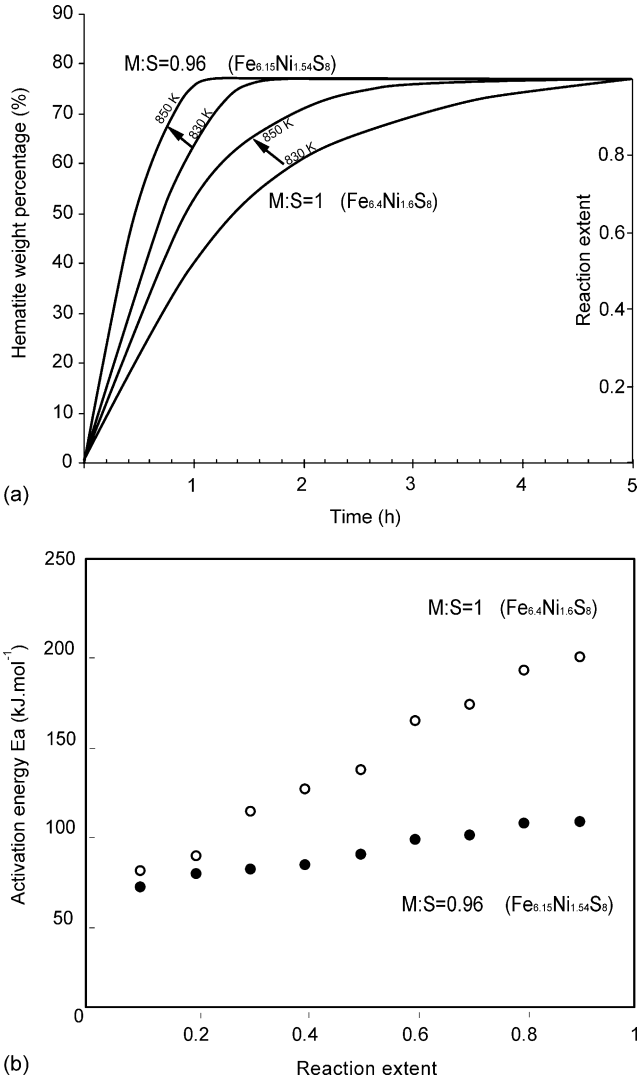

Fig. 10. (a) Graph showing the variation of hematite wt.% and reaction extent with oxidation time. The time function of hematite wt.% (or y) evolves with temperature (T). (b) Dependence of E_a on y for the oxidation of *mss* compositions $Fe_{6.4}Ni_{1.6}S_8$ and $Fe_{6.15}Ni_{1.54}S_8$ in the temperature range 830–850 K. The calculated values of activation energy are represented by symbols (◯) and (●) for compositions $Fe_{6.4}Ni_{1.6}S_8$ and $Fe_{6.15}Ni_{1.54}S_8$, respectively.

induction stage occurs. It is clearly shown in Fig. 9b that the S-rich sample oxidized at a more rapid rate at the beginning and the oxidation rate approached zero after 1.5 h, whereas the non-S-rich sample was still under oxidation at a reaction rate of $5 \times 10^{-4}\,s^{-1}$. The average reaction rates within 1.5 h for the samples $Fe_{6.15}Ni_{1.54}S_8$ and $Fe_{6.4}Ni_{1.6}S_8$ are 1.85×10^{-4} and $1.22 \times 10^{-4}\,s^{-1}$, respectively. The activation energies for the oxidation of both compositions are calculated using Eq. (6) assuming the reaction mechanism does not change significantly in the temperature range 830–850 K. Fig. 10a shows the time dependence of hematite wt.% (or reaction extent) evolves with temperature. This time function of $y \sim y(t)$ is used to determine the E_a dependence of y (Fig. 10b). It is shown that the oxidation of $Fe_{6.4}Ni_{1.6}S_8$ has a higher E_a than $Fe_{6.15}Ni_{1.54}S_8$ over the course of reaction. The activation energy increases with y from 67.1 to 103.3 kJ mol^{-1} for *mss* composition $Fe_{6.15}Ni_{1.54}S_8$; 76.1 to 195.0 kJ mol^{-1} for $Fe_{6.4}Ni_{1.6}S_8$. The thickening of oxide layer, which inhibits the diffusion of O_2 into the unreacted *mss* particles, causes the increasing E_a with y.

The effect of nickel content on the oxidation rate of *mss* was investigated by performing oxidation experiments on two *mss* compositions $Fe_{7.9}S_8$ and $Fe_{2.37}Ni_{5.53}S_8$. The oxidation achieved equilibrium in 1 h for the nickel-rich composition and 5 h for the pure Fe *mss* sample. It appears that adding nickel to *mss* increases the oxidation rate, which reflects the fact that *mss* composition $Fe_{7.9}S_8$ requires over three times as much oxygen from the atmosphere to complete the oxidation as composition $Fe_{2.37}Ni_{5.53}S_8$ does. Oxygen diffusion into the particle is the controlling factor during oxidation of metal sulfides [11]. This reduction in the reaction rate for nickel-free *mss* is related to the high oxygen-consumption rate caused by high iron concentration, which inhibited the diffusion of oxygen into the particle. For the nickel-rich sample, on the other hand, oxygen on the surface of the particle is relatively abundant due to a lower iron concentration in *mss*.

5. Conclusions

The oxidation products of *mss* vary in our samples depending on their stoichiometry. Apart from the common oxidation products hematite and $Ni_{17}S_{18}$, mikasaite ($Fe_2(SO_4)_3$) was observed during the oxidation of $Fe_{7.9}S_8$, and pentlandite for $Fe_{6.15}Ni_{1.54}S_8$. Iron in the *mss* was preferentially oxidized to hematite, leaving a nickel enriched *mss* core. Nickel in the *mss* samples was less active than iron and eventually existed in the form of $Ni_{17}S_{18}$, a pyrrhotite-like phase. For iron–nickel *mss*, X-ray diffraction evidence shows that the *mss* gradually underwent a topotactic structural transformation from hexagonal (P6/mmc) to trigonal ($P3\,2$) during the oxidation. The transformation was related to the enrichment of nickel in *mss*.

This study also demonstrated that increasing sulfur content in the *mss* accelerates the oxidation rate of *mss*. Also, the oxidation of *mss* samples showed a decrease in reaction rate as Ni:Fe atomic ratio decreased.

Acknowledgments

This research was supported by Australian Research Council and Australian Institute for Nuclear Science and Engineering. HW would like to thank the Australian Education, Science and Training Department for the APA award, which has allowed this work to be carried out.

References

[1] D.J. Vaughan, J.R. Craig, Mineral Chemistry of Metal Sulfides, Cambridge University Press, Cambridge, 1978.
[2] J.G. Dunn, L.C. Mackey, J. Therm. Anal. 39 (1993) 1255.
[3] J.G. Dunn, V.L. Howes, Thermochim. Acta 282/283 (1996) 305.
[4] A.C. Chamberlain, The effect of stoichiometry on the thermal behavior of synthetic iron–nickel sulfides, Ph.D. Dissertation, Curtin University of Technology, 1996.
[5] A.C. Banerjee, Indian J. Chem. 14A (1976) 845.
[6] Z. Asaki, K. Matsumoto, T. Tanabe, Y. Kondo, Metall. Trans. B 14B (1983) 109.
[7] Z. Asaki, S. Mori, M. Ikeda, Y. Kondo, Metall. Trans. B 16B (1985) 627.
[8] N.S. Saliullin, E.B. Gitis, J. Appl. Chem. U.S.S.R. 41 (1968) 1596.
[9] M.J. Nichol, P.D. Scott, J. S. Afr. Inst. Min. Metall. (1979) 298.
[10] R.T. Lowson, Chem. Rev. 5 (1982) 461.
[11] J.G. Dunn, A.C. Chamberlain, J. Therm. Anal. 37 (1991) 1329.
[12] R.V. Nicholson, Short Course Handbook on Environmental Geochemistry of Sulfide Mine-Wastes, Mineralogical Association of Canada, Nepean, Ont., 1994.
[13] M.P. Janzen, R.V. Hicholson, J.M. Scharer, Geochim. Cosmochim. Acta 64 (2000) 1511.
[14] G. Kullerud, Experimental techniques in dry sulfide research, in: G.C. Ulmer (Ed.), Research Techniques for High Pressure and High Temperature, Springer-Verlag, Berlin, 1971.
[15] B. Etschmann, A. Pring, A. Putnis, B.A. Grguric, A. Studer, Am. Miner. 89 (2004) 39.
[16] H. Wang, A. Pring, Y. Ngothai, B. O'Neill, Geochim. Cosmochim. Acta, in press.
[17] WaveMetrics Inc., Igor Pro Version 4.0, WaveMetrics Inc., USA, 2000.
[18] H.M. Rietveld, Acta Crystallogr. 22 (1967) 151.
[19] H.M. Rietveld, J. Appl. Crystallogr. 2 (1969) 65.
[20] E.H. Kisi, Mater. Forum. 18 (1994) 135–153.
[21] R.J. Hill, C.J. Howard, J. Appl. Crystallogr. 18 (1985) 173.
[22] R.J. Hill, C.J. Howard, LHPM: A Computer Program for Rietveld Analysis of X-ray and Neutron Powder Diffraction Patterns, Australian Nuclear Science and Technology Organization, 1998.
[23] N. Alsen, Geologiska Foereningens i Stockholm Foerhandlingar. 47 (1925) 19.
[24] G. Collin, C. Chavant, R. Comes, Acta Crystallogr. B 39 (1983) 289.
[25] A.D. Pearson, M.J. Buerger, Am. Miner. 41 (1956) 804.
[26] L. Pauling, S.B. Hendricks, Am. Chem. Soc. 47 (1925) 781.
[27] P.C. Christidis, P.J. Rentzeperis, Zeitschrift fuer Kristallographie. 144 (1976) 341.
[28] R.A. Yund, H.T. Hall, J. Petrol. 11 (1970) 381.
[29] S. Vyazovkin, C.A. Wright, Annu. Rev. Phys. Chem. 48 (1997) 125.
[30] S. Vyazovkin, New J. Chem. 24 (2000) 913.
[31] S. Vyazovkin, J. Comput. Chem. 18 (1997) 393.
[32] S. Vyazovkin, D. Dollimore, J. Chem. Inf. Comput. Sci. 36 (1996) 42.
[33] R. Mohan, M.D. Mckinley, G.W. Douglas, Proceedings of the Fifth Underground Coal Conversion Symposium, Alexandria, VA, 1979.
[34] Z. Zhang, L. Wang, Y.K. Liu, X. Feng, J. Xi'an Jiaotong Univ. 37 (2003) 11.

[35] J.G. Dunn, L.C. Mackey, J. Therm. Anal. 37 (1991) 2143.
[36] J.G. Dunn, G.C. De, B.H. O'Connor, Thermochim. Acta 145 (1989) 115.
[37] J.G. Dunn, G.C. De, B.H. O'Connor, Thermochim. Acta 155 (1989) 135.
[38] F.R.A. Jorgensen, F.J. Moyle, J. Therm. Anal. 25 (1982) 473.
[39] F.R.A. Jorgensen, F.J. Moyle, J. Therm. Anal. 29 (1984) 13.
[40] F. Habashi, Chalcopyrite: its Chemistry and Metallurgy, McGraw Hill International Book Co., New York, 1987.
[41] F.T. Bumazhnov, A.S. Lenchev, Dokl. Aolg. Akad. Nauk. 25 (1972) 953.
[42] H. Tsukada, Z. Asaki, T. Tanabe, Y. Kondo, Metall. Trans. B 12B (1981) 603.
[43] T. Rosenqvist, J. Iron Steel Inst. 176 (1954) 37.
[44] M. Nagamor, M. Kameda, Trans. Jpn. Inst. Met. 19 (1968) 187.
[45] E.T. Turkdogan, Trans. TMS-AIME 242 (1968) 1665.
[46] A.V. Vanyukov, Y.B. Boitkovskii, Zh. Prikl. Khim. 51 (1978) 1124.
[47] J.G. Dunn, Thermochim. Acta 300 (1997) 127.
[48] A.C. Chamberlain, J.G. Dunn, Thermochim. Acta 340/341 (1999) 367.
[49] G. Kullerud, Can. Miner. 7 (1962) 353.
[50] H. Wang, Y. Ngothai, B. O'Neill, A. Pring, The Effects of S Fugacity on the Exsolution of Pentlandite (Fe, Ni)$_9$S$_8$ from the Monosulfide Solid Solution (Fe, Ni)S, in: Proceedings of the 31st Annual Australian Chemical Engineering Conference, Adelaide, Australia, 2003.
[51] K.C. Misra, M.E. Fleet, Econ. Geol. 68 (1973) 518.

CHAPTER SIX

Wang Haipeng, Pring Allan, Ngothai Yung and O'Neill Brian (2006)
The kinetics of the $\alpha \rightarrow \beta$ transition in synethetic nickel monosulfide.
American Mineralogist, v. 91 pp. 171-181, 2006

CHAPTER SEVEN

Wang Haipeng, Pring Allan, Ngothai Yung and O'Neill Brian (2006)
The mechanism and kinetics of α-NiS oxidation in the temperature range 670-700 ^{o}C
American Mineralogist, v. 91 pp. 537-543, 2006

CHAPTER EIGHT

Chapter 8: Summary and Conclusions

8.1 Introduction

The principal achievement of this work is the development of a new kinetic model, the *Refined Avrami* method, to solve the often-encountered difficulty of predicting the kinetic behavior caused by changes in the activation energy (E_a) over the course of a reaction. By formalizing time functions of E_a, the kinetic data fitting is significantly improved. This method is used in solid-state reactions involving nonstoichiometric phases (e.g. $(Fe,Ni)_{1-x}S$, $Ni_{1-x}S$) for which variations in E_a with time appear to be more significant than for reactions that involve only stoichiometric compounds. The *Refined Avrami* method also allows us to identify different reaction stages by analyzing the E_a variations during the reactions. An example of using this method to differentiate two dominant reaction mechanisms is illustrated in Figure 8.1. Pentlandite exsolves from two different *mss* compositions, $(Fe_{0.77}Ni_{0.19})S$ and $(Fe_{0.8}S_{0.2})S$. These exsolution processes are initially controlled by nucleation mechanisms but switch to crystal growth mechanisms as the reactions near completion. The difference in bulk composition of the two *mss* hosts determines their specific activation energy profiles in the nucleation stage, as higher metal content facilitates nucleation. The compositions of the two *mss* hosts converge towards the end of the reaction, due to the depletion of metal content in the host. As a consequence the E_a in the crystal growth stage varies for the two *mss* hosts.

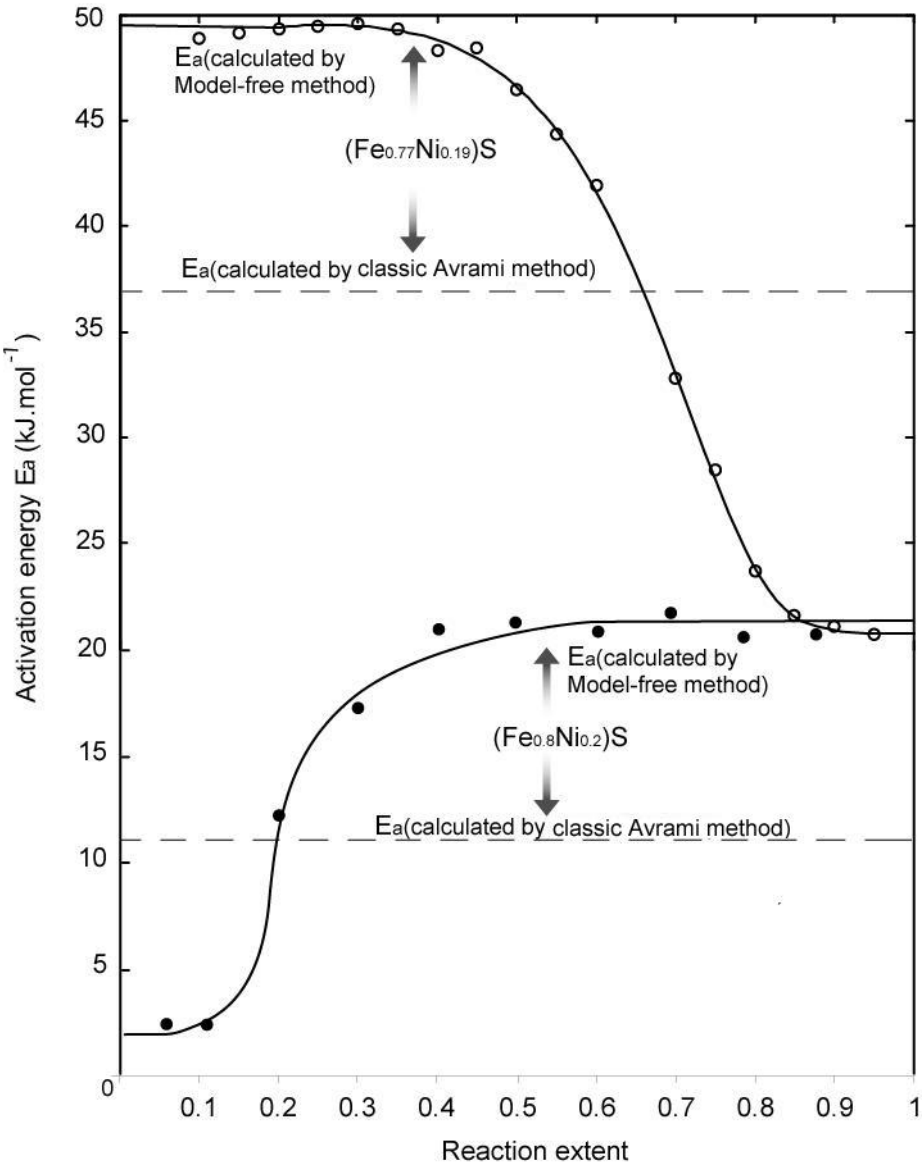

Figure 8.1. Curves showing the dependence of E_a (activation energy) on reaction extent (y) for the pentlandite exsolution from *mss*/pyrrhotite compositions: $(Fe_{0.77}Ni_{0.19})S$ and $(Fe_{0.8}Ni_{0.2})S$. The calculated values of activation energy using the *Refined Avrami* method are represented by symbol "○" for $(Fe_{0.77}Ni_{0.19})S$; "●" for $(Fe_{0.8}Ni_{0.2})S$. The solid curves are produced by *least-square* method (sigmoid function). Dashed lines represent E_a calculated using classic *Avrami* method.

8.2 Exsolution of $(Fe,Ni)_9S_8$ from $(Fe,Ni)_{1-x}S$

The first successful implementation of the *Refined Avrami* method was achieved in the study of the kinetics of pentlandite exsolution (from *mss* host). The *mss*/pyrrhotite host experienced progressive depletion in metal content during the exsolution. The nonstoichiometric nature of this *mss*/pyrrhotite distinctly impacts on the exsolution steps, such as nucleation, new phase growth and atomic diffusion, lamellae coarsening. The changing chemical environment caused by metal depletion of *mss* makes the kinetic analysis very complex and the dominant mechanisms cannot be elucidated in detail. In mineral reactions of this type, the true functional form of the reaction model is almost never known, and the *Arrhenius* parameters determined by the classic *Avrami* method are skewed to compensate for errors in the model. The *Refined Avrami* method employs the important concept that activation energy depends on reaction extent (y). Kinetic study of pentlandite exsolution from *mss*/pyrrhotite was performed for the low temperature range from 200 to 300 ^{o}C. For *mss*/pyrrhotite with bulk composition $(Fe_{0.77}Ni_{0.19})S$, activation energy of pentlandite exsolution, E_a varies from 49.6 kJ.mol^{-1} at the beginning of reaction (nucleation is dominant) to 20.7 kJ.mol^{-1} at the end (crystal growth is dominant).

In general, the activation energy varies during the course of solid reaction with the extent of reaction. The surrounding environment of reactant atoms affects an atom's activity and consequently may more or less account for changes of activation energy E_a.

8.3 Oxidation of $(Fe,Ni)_{1-x}S$

A second demonstration of the usefulness of the *Refined Avrami* method is illustrated by the study of the oxidation of *mss*, $(Fe,Ni)_{1-x}S$. The oxidation process involves nonstoichiometric variation in *mss* composition. The activation energies of the oxidation for $Fe_{6.4}Ni_{1.6}S_8$ and $Fe_{6.15}Ni_{1.54}S_8$ steadily increase over the course of oxidation. The

oxidation products of *mss* depends on the composition and stoichiometry. Apart from the common oxidation products hematite and $Ni_{17}S_{18}$, mikasaite ($Fe_2(SO_4)_3$) was observed during the oxidation of $Fe_{7.9}S_8$, whilst pentlandite was formed in the case of $Fe_{6.15}Ni_{1.54}S_8$. Iron in the *mss* was preferentially oxidized to hematite, leaving a nickel enriched *mss* core. Nickel in the *mss* samples is less active than iron and eventually forms $Ni_{17}S_{18}$, a pyrrhotite-like phase. For iron-nickel *mss*, X-ray diffraction evidence demonstrates that the *mss* gradually underwent a topotactic structural transformation from hexagonal (P6/mmc) to trigonal (P3 2) during the oxidation. This transformation is related to the enrichment of nickel in *mss*.

This study also demonstrated that increasing sulfur content in the *mss* accelerates the oxidation rate of *mss*. The oxidation of the sulfur content in *mss* is an exothermic process and is important in flash smelting. Abundant evolved sulfur, reacting with oxygen at the surface of the particles, increases the surface temperature and speeds the oxidation of iron to hematite. As well during the oxidation of *mss* samples, a decrease in reaction rate was observed as the Ni: Fe atomic ratio decreased. Oxygen diffusion into the particles is the controlling factor during the oxidation of metal sulfides. The reduction in the reaction rate for nickel-free mss is related to the high oxygen-consumption rate on the particle surface caused by high iron concentration, which inhibited the diffusion of oxygen into the particle. For the nickel-rich sample, on the other hand, oxygen on the particle surface is relatively abundant due to a lower iron concentration in *mss*.

8.4 α → β transition in $Ni_{1-x}S$

The transition behavior of α- to β- nickel monosulfide is complex. When β-nickel monosulfide exsolves from the stoichiometric composition (α-NiS), little variation in E_a

was observed over the course of the reaction, as the composition of α-nickel monosulfide host varies very little during the transition. By contrast, when β-nickel monosulfide exsolves from a nickel deficient composition (α-$Ni_{1-x}S$) the E_a changes significantly over the course of reaction, decreasing from around 70 $kJ.mol^{-1}$ (in the initial stage) to near 20 $kJ.mol^{-1}$ (toward the completion of the reaction).

8.5 Oxidation of NiS

There is no obvious variation in E_a during the oxidation of equimolar NiS and very little compositional variations of phases were observed. The *Refined Avrami* and the classic *Avrami methods* produce similar kinetic results for these reactions. In an open-air environment, the oxidation mechanism of α-NiS is constant at 670 and 680^oC, dominated by the direct oxidation of α-NiS → NiO. However, the dominant oxidation mechanism changes to a two-step chain reaction: $\alpha\text{-NiS} \xrightarrow{k1} Ni_3S_2 \xrightarrow{k2} NiO$ at 700^oC. Clearly, different kinetic models ought to be applied to these two distinct reaction mechanisms. Activation energy for the oxidation, α-NiS → NiO, in the temperature range 670 to 680^oC was calculated to be 868.2 $kJ.mol^{-1}$ using *Avrami/Arrhenius* method. The rate constant k_1 and k_2 are approximated to be 3.4×10^{-4} s^{-1} and 4.7×10^{-4} s^{-1} for the first part and second part of the chain reaction respectively. The study of the variation in reaction rate with oxidation time illustrates the optimum oxidation time zone for each temperature, where NiO was produced at the fastest rate.

8.6 Kinetic Implications

In these four sets of kinetic experiments, the changes in activation energy during the course of reaction are obvious for the reactions involving nonstoichiometric compounds, whereas for the oxidation of NiS, with little variation in the stoichiometry of NiS during

the reaction, the activation energy remains constant. It is plausible to relate the change in activation energy to the compositional variations of the nonstoichiometric compounds during the reactions. According to the "Transition State Theory", the activation energy needed to form an activated complex (an intermediate species between reactant and product) depends on the chemical environment surrounding the reactant atoms. For example: in reactions involving nonstoichiometric *mss* $(Fe,Ni)_{1-x}S$ or nickel monosulfide $Ni_{1-x}S$, the gradual changes in their compositions during the reactions lead to changes in the metal vacancy ratio in their crystal structures. Therefore, the chemical environment surrounding the reactant atoms varies during the reaction. The value of overall activation energy may be partially attributed to the formation/annihilation of metal vacancies.

8.7 Suggestions for Further Work

1. The *Refined Avrami* method, which employs the notion of changing E_a with *y* is a more generalized kinetic formalization, whereas the classic *Avrami* method is for the special case where the constancy of E_a is assumed. The kinetic results produced by the *Refined Avrami* method conform to that produced by the classic *Avrami* method when the assumption of constant E_a does not introduce significant deviation in the linearity of the $\ln\ln(1/(1-y))\sim\ln t$ curve (*y*, the reaction extent; *t*, the reaction time). However, this assumption is not always sufficient. The compositional variation of nonstoichiometric compounds (e.g. $(Fe,Ni)_{1-x}S$ and $Ni_{1-x}S$) during reactions is likely to result in distinct changes in E_a. The *Refined Avrami* method is designed to reveal the trend of E_a variations and differentiate different reaction mechanisms at different stages during a reaction. This method

can be applied to other nonstoichiometric systems such as: Fe-Co-S, Fe-Cu-S, and Fe-S-Se.

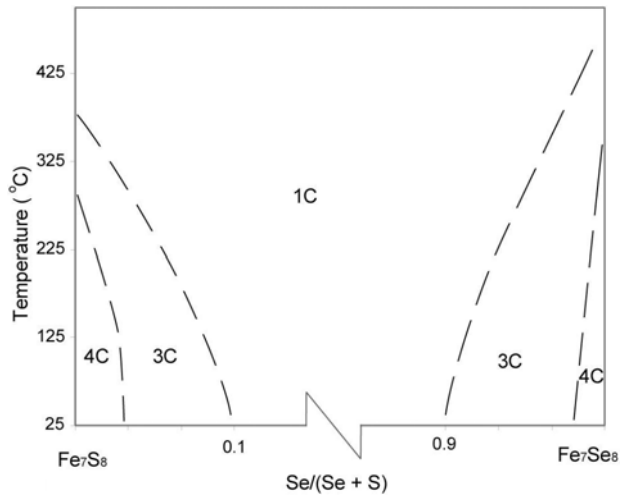

Figure 8.2. Phase relations along the FeS-FeSe joint (after Ericsson et al., 1997).

2. The *Refined Avrami* method can be used to study the kinetics of phase transitions in the FeS-FeSe joint (see Figure 8.2). The substitution of S with Se will certainly vary the chemical environmental within the crystal structure. This may cause distinct variation in activation energy during the phase transitions. The near end member compositions (FeS and FeSe) have 4C superstructures. At room temperature, the increase in substitutional anions in the FeS-FeSe solid solution results in a crystal structure evolution from 4C to 3C and finally 1C structure of NiAs-type subcell when $0.12 < Se: (S + Se) < 0.88$ (Ericsson et al., 1997). The vacancy ordering is the direct cause for the formation of superstructures of NiAs-type and the ferrimagnetic property of pyrrhotites. The vacancy ordering is affected by S-Se substitution and the kinetics of vacancy ordering depends on temperature and the stoichiometry of Fe-S-Se solid solution.

3. The kinetic method developed in this work can also be used for industrial applications such as nickel extraction from nickeliferous sulfides. Pyrrhotite group minerals often contain reasonable amount of nickel impurities as cation substitutions in their crystal structures. The nickel extraction from its host pyrrhotite phases is of economic interest. An important step of the nickel extraction is pyrrhotite leaching, which removes both nickel and iron from the solid pyrrhotite minerals by dissolving them into acidic solutions (e.g. sulfuric acid, nitric acid) (Queneau, 1973; Van-Weert et al., 1974; Yan and Xianluang, 1988; Prater and Shang and Van-Weert, 1993; Droppert and Shang, 1995). A metal deficient layer forms on the surface of metal sulfide after leaching in acidic solutions. The formation of nonstoichiometric layer (NL) proceeds via the removal of metal (e.g. Fe + Ni) from the sulfide structure leave the metal depleted zone. A kinetic study of the formation of NL layer on the leaching rate of the nickeliferous sulfides could be of significant economic interest.

4. The α- and β- transitions of pyrrhotite group minerals are well recognized, however, the accurate phase curves of the α- and β- transitions of pyrrhotite have not been established. Pyrrhotite group minerals experience rearrangements of their magnetic moments upon heating. Figure 8.3 shows that the moments flip from // *c* axis of pyrrhotite to $\perp c$ during α- transition and experience moment disordering during β- transition (Li and Franzen, 1996). Neutron diffraction technique and Mössbauer spectroscopy are recommended to characterize magnetic property variations during the kinetic studies.

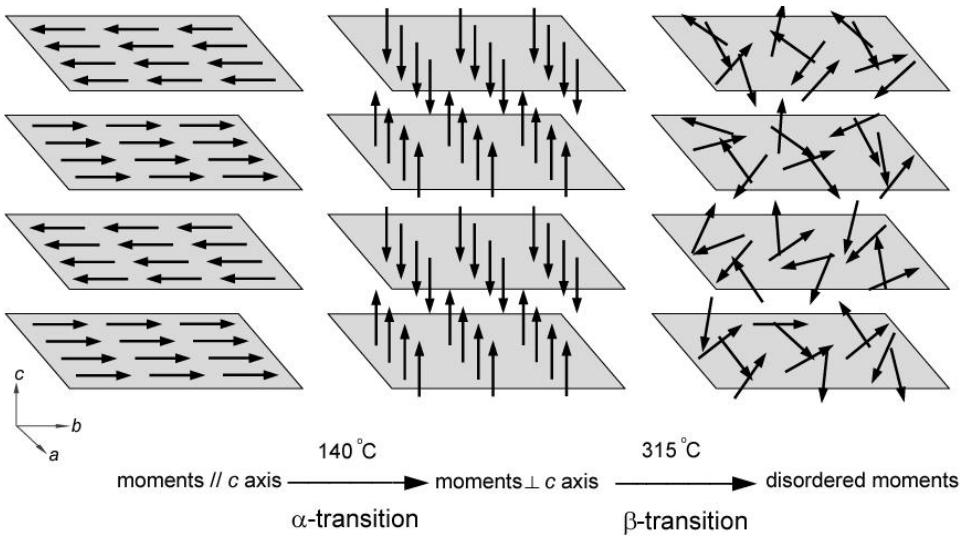

Figure 8.3. The transitions of magnetic moments configuration in FeS during a heating process (α-transition at 140°C, β-transition at 315°C).

5. In this work, anneal-quench technique was used to investigate kinetic behaviors of several solid-state reactions in metal sulfide system. However, numerous phase transitions in metal sulfide systems are very rapid. This trend becomes more significant in high temperature ranges. It is important for further work being carried out *in-situ* in order to study faster solid-state reactions at elevated temperatures.

8.8 References

Droppert, D. and Shang, Y. (1995), The leaching behavior of nickeliferous pyrrhotite concentrate in hot nitric acid. Hydrometallurgy. 39,169-182.

Ericsson, T., Amcoff, Ö. and Nordblad, P. (1997), Superstructure formation and magnetism of synthetic selenian pyrrhotite of $Fe_7(S_{1-y}Se_y)_8$, $y \leq 1$ composition, European Journal of Mineralogy 9, 1131-1146.

Li, F., Franzen, H. F. (1996), Phase transitions in near stoichiometric iron sulfide, Journal of Alloys and Compounds, 238,73-80.

Prater, J.D. and Queneau, P.B., Hudson T.J. (1973), Nitric acid route to processing copper concentrates. AIME Transactions 254, 117-122.

Shang, Y., Van-Weert, G. (1993), Iron control in nitrate hydrometallurgy by autoclaving hydrolysis of iron(III) nitrate. Hydrometallurgy, 33, 273-290.

Van-Weert, G., Mah, K. and Piret, N. (1974), Hydrometallurgy Section, Metallurgical Society of CIM, Edmonton, pp63-69.

Yan, S.and Xianluang, L. (1988), In: Proc. 1st International Conference of Hydrometallurgy (ICHM'88). Academic Press, Beijing, pp135-139.

Coauthored journal publication: thermal expansion of troilite and pyrrhotite

APPENDIX A

Tenailleau C., Etschmann B., Wang H., Pring A., Grguric B.A. and Studer A. (2005)
Thermal expansion of troilite and pyrrhotite determined by in situ cooling (873 to 373 K) neutron powder diffraction measurements
Mineralogical Magazine, v. 69, no. 2 pp. 205-216

Conference paper: Effect of S fugacity on *mss* → pentlandite

CHEMECA 2003, 31st Annual Australian Chemical Engineering Conference

2003, Adelaide, Australia

APPENDIX B

Wang H., Ngothai Y., O'Neill B., Etschmann, B. and Pring A. (2003)
The effects of S fugacity on the exsolution of pentlandite $(Ni,Fe)_9S_8$ from the monosulfide solid solution (Fe,Ni)S*
Chemeca 2003, 31st Annual Australian Chemical Engineering Conference, 2003, Adelaide, Australia.

Conference paper: X-ray study of α- to β- $Ni_{1-x}S$/NiS

CHEMECA 2005, 33st Annual Australian Chemical Engineering Conference

2005, Brisbane, Australia

APPENDIX C

Wang H., Pring A., Ngothai Y. and O'Neill B. (2005)
X-ray diffraction study of the transition kinetics of α- to β-nickel monosulfide
Chemeca 2005, 33rd Annual Australian Chemical Engineering Conference, 2005, Brisbane, Australia.

Conference paper: Phase relations of pyrrhotite group minerals

CHEMECA 2005, 33st Annual Australian Chemical Engineering Conference

2005, Brisbane, Australia

APPENDIX D

Ngothai Y., Wang H., Pring A. and O'Neill B. (2005)
A review on the controversial phase relations of pyrrhotite group minerals in low temperature ranges
Chemeca 2005, 33rd Annual Australian Chemical Engineering Conference, 2005, Brisbane, Australia.

Conference paper: Phase evolution of *mss* during oxidation

CHEMECA 2005, 33st Annual Australian Chemical Engineering Conference

2005, Brisbane, Australia

APPENDIX E

Wang H., Pring A., Ngothai Y., Xie Y. and O'Neill B. (2005)
Phase evolution during the oxidation of monosulfide solid solution under isothermal conditions
Chemeca 2005, 33rd Annual Australian Chemical Engineering Conference, 2005, Brisbane, Australia.

Conference paper: Model-free kinetics of *mss* → pentlandite

7Th World Congress of Chemical Engineering

2005, Glasgow, U.K.

APPENDIX F

Wang Haipeng, Pring Allan, Ngothai Yung and O'Neill Brian (2005)
Model-free kinetics of the pentlandite exsolution from monosulfide solid solution
7th World Congress of Chemical Engineering, 2005, Glasgow, U.K.

Conference paper: A mineralogical note

7Th World Congress of Chemical Engineering

2005, Glasgow, U.K.

APPENDIX G

Wang Haipeng, Ngothai Yung, O'Neill Brian and Pring Allan, (2005)
A mineralogical kinetics note: negative activation energy or misinterpretation of *Avrami method?*
7th World Congress of Chemical Engineering, 2005, Glasgow, U.K.